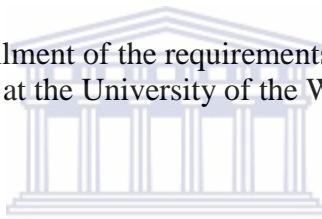


# New bands in $^{192}\text{Tl}$ using gamma spectroscopy techniques

Jayson Lee Easton

Thesis presented in fulfilment of the requirements for the degree of  
Magister Scientiae at the University of the Western Cape



Supervisor:

Dr E. A. Lawrie  
Department of Physics  
iThemba LABS

Co-supervisor

Prof. R Lindsay  
Department of Physics  
University of the Western Cape

**December 2011**

# **New bands in $^{192}\text{Tl}$ using gamma spectroscopy techniques**

Jayson Lee Easton

## **Keywords**

**Gamma spectroscopy**

**Thallium 192**

**High spin states**

**Chiral bands**

**Gamma-gamma coincidence**

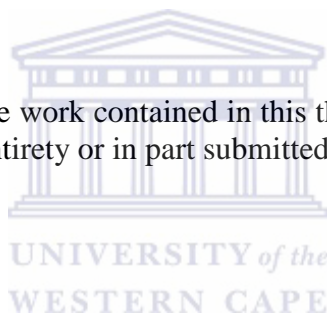
**AFRPDITE Array**

**Level scheme**



## DECLARATION

I, the undersigned, declare that the work contained in this thesis is my own original work and that I have not previously in its entirety or in part submitted it to any university for a degree.



Signature:.....

Date:.....

# New bands in $^{192}\text{Tl}$ using gamma spectroscopy techniques

Jayson Lee Easton

Thesis presented in fulfilment of the requirements for the degree of Master of Science at the  
University of the Western Cape



Supervisor:

U Dr E. A. Lawrie *of the*  
WESTERN CAPE  
Department of physics  
iThemba Labs

Co- supervisor:

Professor Robert Lindsay  
Department of physics  
University of the Western Cape

December 2011

## Contents

I.	Abstract	1
1.	CHAPTER 1 Introduction	2
1.1	Motivation of the present work	2
1.2	Chirality	3
2.	CHAPTER 2 Experimental methods	5
2.1	Producing the nuclei of interest	5
2.1.1	Nuclear Reaction	5
2.1.2	Beam	7
2.1.3	Target	9
2.2	Gamma-rays in matter	10
2.2.1	Photoelectric effect	10
2.2.2	Pair production	11
2.2.3	Compton scattering	13
2.2.4	Attenuation of gamma rays in matter	14
2.3	Detection of gamma rays	14
2.3.1	Detectors	14
2.3.2	Compton suppression	21
2.3.3	Detector Placement	22
2.3.4	AFRODITE array	25
2.3.5	Absorbers	26
2.4	Electronics basic ideas	27
2.4.1	Energy measurements	27
2.4.2	Timing circuits	29
2.4.3	Pole Zero	32
2.4.4	Threshold	33
2.4.5	Trigger and Gamma-Gamma coincidence	33
3.	Chapter 3 Preliminary data analysis	35
3.1	Data Acquisition	35
3.2	$E_\gamma - E_\gamma$ Matrix	36

3.3	Data analysis	36
3.3.1	Programs	36
3.4	Energy and time-gain matching, Doppler correction and gain drifts	37
3.4.1	Energy gain matching and calibrations	37
3.4.2	Time gain matching and calibration	41
3.4.3	Gain drift and Energies	42
3.4.4	Gamma coincidence analysis	49
4.	Chapter 4 Data analysis, results and discussion	50
4.1	Contaminants	50
4.1.2	External sources of contaminants	50
4.1.3	Internal sources of contaminants	53
4.2	Results	54
4.2.1	Building the level scheme	54
4.2.1.1	Confirmation of the known level scheme Band 1	54
4.2.1.2	Extension of band 1	57
4.2.1.3	Band2	64
4.2.1.4	Other decays of band 2	71
4.2.1.5	Band3	74
4.2.1.6	Other difficult cases	76
4.2.1.7	Almost doublet	77
4.2.1.8	The final level scheme	80
4.3	Discussion and conclusion	82
4.3.1	Deformed Shell model	82
4.3.2	Band1	87
4.3.3	Band4	91
4.3.4	Band3 and band2	94
5.	Conclusion	95
6.	Reference	97

## I. Abstract

High spin excited states in  $^{192}\text{Tl}$  were studied using gamma-ray spectroscopy. The study included taking an active part in performing the experiment, understanding the experimental procedure, electronics and data acquisition in this experiment. The high spin states in  $^{192}\text{Tl}$  were produced using a  $^{37}\text{Cl}$  beam and  $^{160}\text{Gd}$  target. The nine clovers of the AFRODITE array were placed at  $90^\circ$  and  $135^\circ$ . The target was thin, allowing the residual thallium nuclei to recoil in vacuum. Two weeks of data was acquired and analysed in this work. In addition more data was acquired in order to perform DSAM lifetime measurements, but this is beyond the scope of this work. The preliminary data analysis of the thin target data involved energy and time-gain matching calibrations as well as Doppler shift and gain drift corrections. Then the data were sorted into matrices and spectra for the actual analysis. The known level scheme of  $^{192}\text{Tl}$  was extended by more than 50 new transitions placed in three new bands. A chiral partner to the yrast band in  $^{192}\text{Tl}$  was searched for but not found. But there is still a possibility such a band to be discovered, when the additional three weekends of data (including the DSAM lifetime measurements) undergo such an analysis.

# 1 CHAPTER 1 Introduction

## 1.1 Motivation of the present work

Gamma spectroscopy research helps us to understand the structure of the nuclei and to explain their observed behaviour. It was suggested recently that some nuclei may exhibit chiral symmetry [Fra97]. This symmetry occurs in the angular momentum space and it was often studied within the framework of the particle rotor model. Such nuclei which could possibly possess chiral symmetry are thought to belong to the 80, 100-130 and 190 mass regions. These nuclei are deformed, and most importantly their shape is triaxial. It was suggested at iThemba LABS that chiral symmetry exist in the thallium isotopes in the 190 mass regions as well.

The main objective of the present research was to test the chirality scenario in  $^{192}\text{Tl}$ . It is expected that a chiral nucleus should exhibit a pair of bands, called chiral partner bands, which should be near degenerate. Using standard gamma spectroscopy one can observe such partner bands and determine how close in excitation energy are the corresponding levels with the same spin and parity. As a finer test of chirality one can use the DSAM to measure the lifetimes of the levels of the chiral doublet band, and establish whether the reduced transition probabilities  $B(M1)$  and  $B(E2)$  are degenerate. An added bonus in this experiment was the good amount of data obtained on  $^{192}\text{Tl}$ . This presented an opportunity to expand the known level scheme of  $^{192}\text{Tl}$ , acquire information on the properties of the newly observed excited states and search for a chiral partner to the yrast band in  $^{192}\text{Tl}$ . This experiment encompasses two sets of data, one obtained when using a thick target and the other when using a thin target. This work focusses on studying  $^{192}\text{Tl}$  using the thin target.

To study the high spin states of interest a fusion evaporation reaction was employed i.e. the reaction  $^{160}\text{Gd} (^{37}\text{Cl}, 5n) ^{192}\text{Tl}$  at a beam energy of 167MeV. The  $^{160}\text{Gd}$  target was approximately  $1.2\text{mg}/\text{cm}^2$  thick.

The gamma rays were detected in the AFRODITE array, which consisted of nine Compton-suppressed high purity germanium clover detectors. The thin target data corresponded to total time of approximately 122 hours of data collection. In order to successfully accomplish the gamma-coincidence study, which was the most important task in the present work, one has to understand well the data acquisition programs used to sort the data and also the experimental procedure employed when doing experiments at iThemba LABS. Thus a big part of this work



includes becoming familiar with the experimental systems and procedures. These included acquiring some knowledge on the electronics used in this experiment, on the data acquisition systems, software and sorting codes. As well as performing preliminary data analysis such as gain matching and other corrections on the data. Finally the actual gamma coincidence analysis leading to considerable extension of the known level scheme was performed.

The results obtained in this work are presented in the following chapters. Chapter 2 includes a brief introduction to chiral symmetry. Chapter 3 describes the experimental methods used to produce  $^{192}\text{Tl}$  and the detection mechanisms of emitted gamma rays. In chapter 4 the data and also analysis the results obtained are presented. These are followed by a discussion and conclusion.

## 1.2 Chirality

Chirality exists in structures which are three dimensional. If an object's mirror image cannot be brought to coincide with itself then the structure is chiral [Fra97]. At the macroscopic level chirality exists in the spatial domain and it is a structural feature of the system. In the nuclear realm chiral features are hard or impossible to infer if considering the spatial matter distribution. However nuclear chirality may exist in the angular momentum space. Odd-odd nuclei have two unpaired nucleons. Thus such nuclei may have three angular momentum vectors that may form a three dimensional structure, which may possess chiral symmetry (see Fig. 1-1). The three angular momentum vectors include the angular momentum of the unpaired proton  $j_\pi$ , of the unpaired neutron  $j_\nu$  and the collective rotation of the nucleus  $R$ . For this system  $J$  is aplanar, i.e.  $J$  is out of the planes defined by any two individual angular momenta.

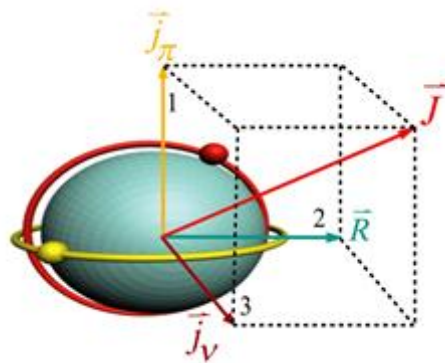


Fig 1-1 The three angular momentum vectors forming a chiral system [Wan10]

Since for this system we have three dimensional object in the angular momentum space we can test it for chiral symmetry. We can use the chiral operator to transform the system shown in Fig 1-1 into its mirror image. This operator has the form  $\hat{O} = \hat{T}\hat{R}_y(\pi)$ , where  $\hat{R}_y(\pi)$  rotates the angular momentum at  $180^\circ$  (anti-clockwise) around the y-axis (axis 2 in Fig.1-1), while  $\hat{T}$  is the time reversal operator and therefore changes to opposite the directions of all angular momentum vectors. One can see this when for instance considering the unpaired proton angular momentum  $\vec{J}_\pi = \vec{r} \times \vec{p}(t)$ , where  $r$  is the radius vector and  $\vec{p}$  is the momentum (which is a function of time  $t$ ). When the time reversal operator operates on  $\vec{J}_\pi$ , one gets  $\hat{T}\vec{J}_\pi = \vec{r} \times \vec{p}(-t) = -\vec{J}_\pi$ . Therefore the chiral operator transforms the system in Fig. 1-1 into that of Fig. 1-2.

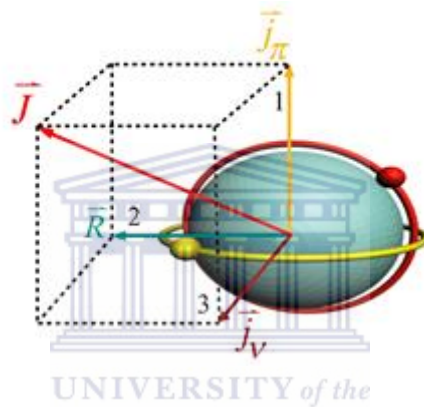


Fig 1-2 Chiral image of the system shown in Fig 1-1[Wan10]

A nuclear chiral system must show two degenerate bands called chiral doublet bands [Fra97]. In an ideal case all properties of the doublet bands should be degenerate (excitation energy, spin, transition probabilities, parity, reduced transition probability  $B(M1)$  and  $B(E2)$ ). These bands should correspond to the same nuclear shape. Many nuclei were studied and several candidate chiral bands were suggested in a number of nuclei. These are nuclei in the mass range of 80, 100, 130 and 190. However no true degeneracy is found thus far. This leaves the question whether chiral symmetry exists in nuclei, without a clear answer. Thus studying the chiral candidates in detail may bring up some new understanding, which could help reveal whether this symmetry is applicable for nuclei.

## 2 CHAPTER 2 Experimental methods

### 2.1 Producing the nuclei of interest

#### 2.1.1 Nuclear Reaction

$^{192}\text{Tl}$  is an isotope of the thallium element that is not found naturally on earth. This is on account of the short half-life of  $^{192}\text{Tl}$  ( $t_{1/2} = \tau \ln 2 = 458\text{s}$ ). When  $^{192}\text{Tl}$  is created it decays via electron capture or positive beta decay to the mercury isobar  $^{192}\text{Hg}$ . Electron capture is a process whereby an orbital electron is captured by a nucleus converting a proton into a neutron,  $p + e^- \rightarrow n + \nu_e$ , where  $\nu_e$  is neutrino emitted in the decay. Positive beta decay on the other hand is the decay of a nuclear proton into a neutron, given by  $p \rightarrow n + e^+ + \nu_e$ .

To create  $^{192}\text{Tl}$  a heavy ion fusion-evaporation (HIFE) reaction was employed [Kra88]. A  $^{37}\text{Cl}$  (chlorine) beam, with energy of 167 MeV and average current of 50 nA bombarded a  $^{160}\text{Gd}$  (gadolinium) target of thickness  $1.26 \text{ mg/cm}^2$ . 167 MeV was chosen to overcome the Coulomb barrier and to maximise the production of high-spin states of the nuclei of interest. Below the Coulomb barrier Coulomb excitation of the target will take place and a fusion reaction will not. The calculated PACE4 (<https://groups.nsl.msu.edu/lise/lise.html>) cross-section as a function of the beam energy is shown in Fig 2-2. It is clear from Fig 2-2 that  $^{192}\text{Tl}$  has the highest probability for production of  $E \sim 167 \text{ MeV}$ .

A classical calculation of the Coulomb potential energy assuming that the two nuclei are spheres that touch each other at the surface gives 147 MeV. This is done as follows. The Coulomb potential is expressed as

$$U = \frac{1}{4\pi\epsilon_0} \frac{Z_1 Z_2 e^2}{r} \quad (2.1),$$

where  $Z_1, Z_2$  are the atomic numbers of the projectile and target respectively and  $e$  is the elementary charge. The total interaction radius is given by  $r = R_{Cl} + R_{Gd}$  with  $R = 1.22A^{1/3} \text{ fm}$ , i.e.  $r = 1.22(37)^{1/3} + 1.22(160)^{1/3} = 10.69 \text{ fm}$ . Inserting  $r$  into (2.1) with the atomic numbers of chlorine (17) and gadolinium (64) and noting that  $\frac{e^2}{4\pi\epsilon_0} = 1.44 \text{ MeV fm}$  gives

$$U = \frac{(17)(64)1.44 \text{ MeV fm}}{10.69 \text{ fm}} = 147 \text{ MeV}.$$

This simplified classical description gives a value which is not far from the PACE4 description, since as one can see in Fig. 2-2 the fusion evaporation channels seem to open only above 150 MeV of beam energy.

Once the projectile can overcome the Coulomb barrier, the two heavy ions undergo fusion. When the compound nucleus is formed it has a high angular momentum. Energy not used to overcome the Coulomb barrier is converted into excitation energy of the nucleus and also into recoil energy. The compound nucleus since it has high energy and angular momentum evaporates light particles (neutrons, protons and/or alpha). Neutrons are favoured over protons and alpha particles because of their lack of charge. This allows the neutrons to be insensitive to the Coulomb barrier, when they are ejected from the compound nucleus.

What is also clear from Fig. 2-1 is that there is a dependence on the number of evaporated neutrons from the energy of the projectile. The higher the energy brought into the system the greater the number of ejected neutrons. The residual nucleus still has a high angular momentum after evaporating light particles. It then decays to its ground state by emitting gamma rays (see Fig. 2-1).

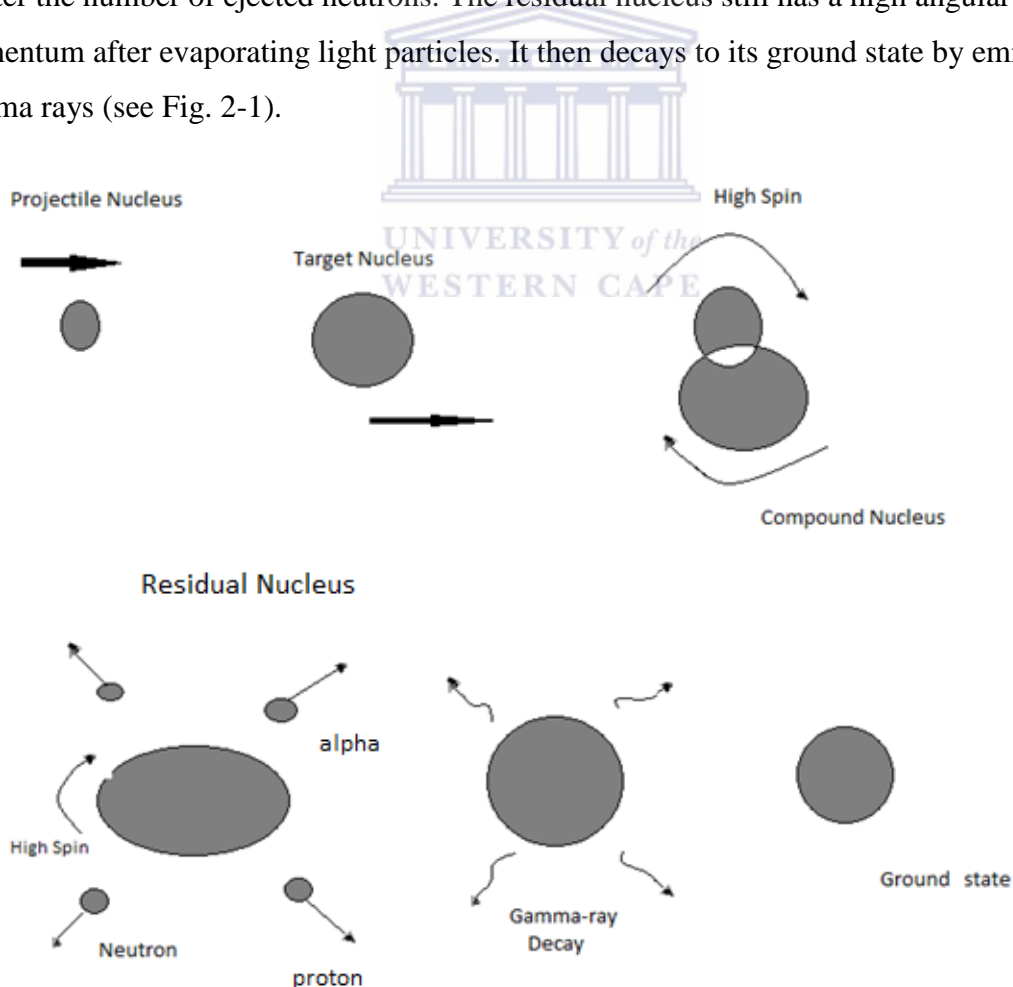


Fig2-1 Fusion Evaporation Reaction

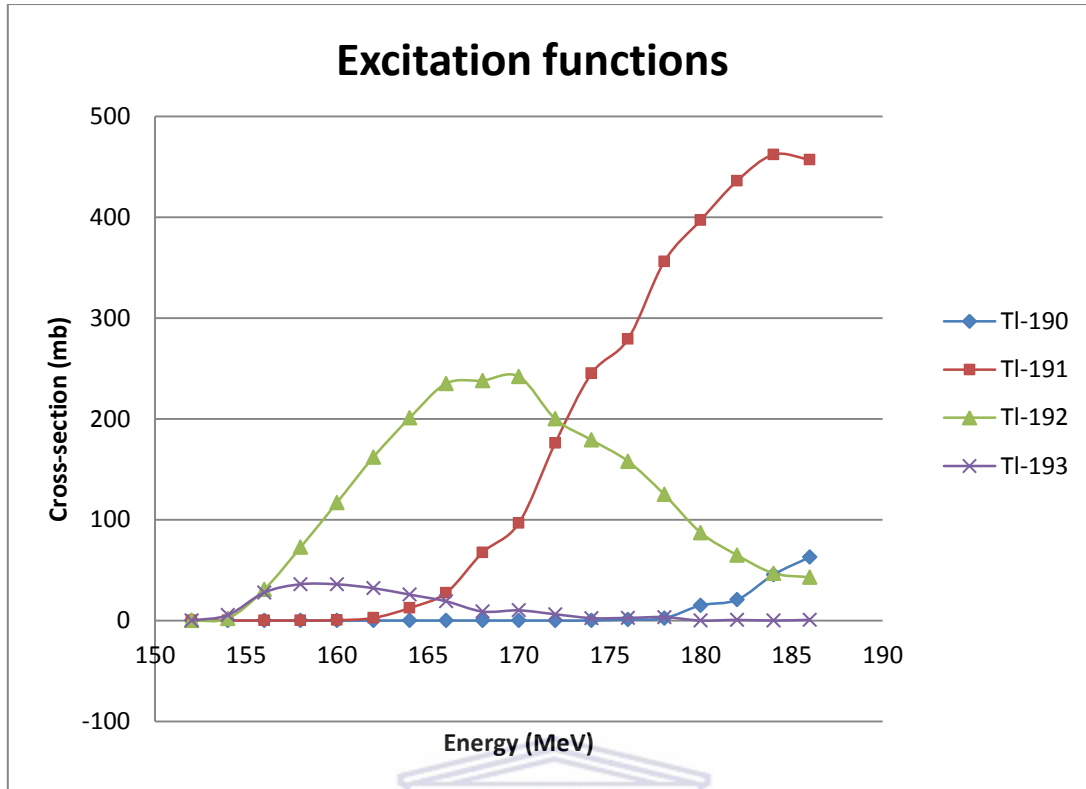
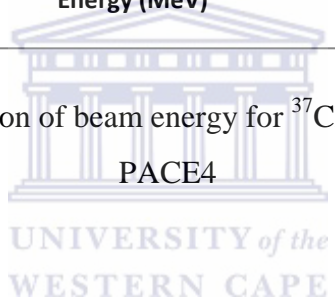


Fig 2-2 Cross-section as a function of beam energy for  $^{37}\text{Cl}$  and  $^{160}\text{Gd}$  target calculated with PACE4



### 2.1.2 Beam

A chlorine beam was created using an electron cyclotron resonance ion source (ECR). Liquid carbon tetrachloride  $\text{CCl}_4$  is atomised and heated to separate chlorine and carbon atoms. This plasma is a mixture of neutral atoms, free electrons, charged carbon and chlorine atoms. Microwave power at frequency of approximately 14.5 GHz is pumped into the chamber holding the plasma. Using  $\omega_e = \frac{eB}{m_e}$  the minimum field needed to create resonance of

electrons in the plasma would be  $B = \frac{\omega_e m_e}{e} = \frac{2\pi(14.5 \cdot 10^9 \text{Hz})(9.1 \cdot 10^{-31} \text{kg})}{1.6 \cdot 10^{-19} \text{C}} = 0.52 \text{ T}$ . The

electrons in the plasma with a gyro frequency of 14.5 GHz, are accelerated by a RF field in particular by the oscillating electric fields which is perpendicular to the magnetic field (see Fig. 2-3)[Uwc11]. In the process electrons are freed when collisions occur, creating plasma with high densities of charged particles ( $10^{12} \text{cm}^{-3}$ ). The electric field is sinusoidal in nature this means that the free electrons experience a maximum acceleration at  $90^\circ$  and  $270^\circ$ . Many

charged states are created ( $Cl^{1+} \rightarrow Cl^{n+}$  and  $C^{1+} \rightarrow C^{n+}$ ). The plasma is extracted and the  $\frac{m}{q}$  ratio is used to single out charged states specific for the experiment beam and energy. For this experiment  $Cl^{6+}$  was extracted.

Once the particles are extracted they are accelerated in one of two solid-pole cyclotrons (SPC1 and SPC2). These are injector cyclotrons. Most of the acceleration of the projectiles is done in the main cyclotron, the SSC (separated-sector cyclotron), which delivered the 167 MeV beam energy needed for this experiment.

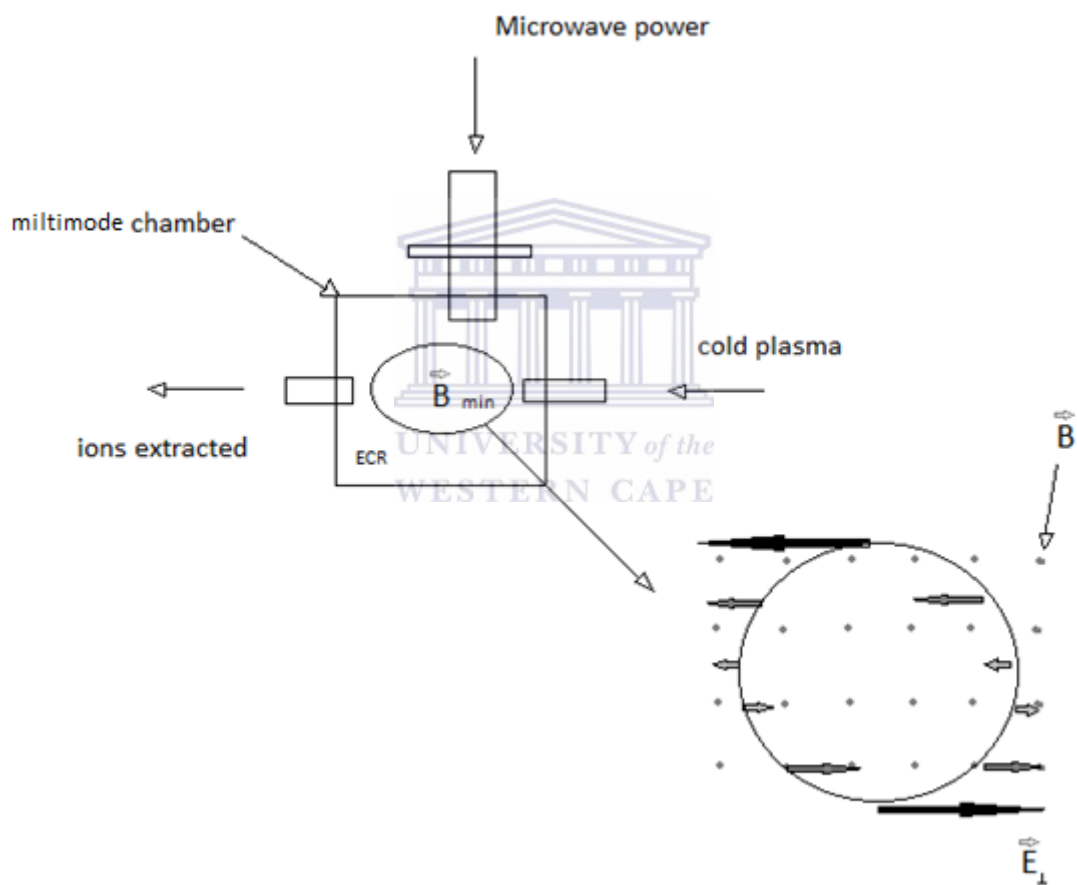


Fig 2-3 ECR ion source

### 2.1.3 Target

This experiment used a thin target of 1.26 mg/cm<sup>2</sup>. The energy of the beam remained relatively constant when moving through the target. Because the linear stopping power

$$S = -\frac{dE}{dx} = \frac{4\pi e^4 z^2}{m_o v^2} NZ \left( \ln \frac{2m_o c^2 \beta^2}{I} - \ln(1 - \beta^2) - \beta^2 \right),$$

where  $N$  is the electron density,  $Z$  the atomic number of target,  $m_o$  the rest mass of electron,  $v$  the velocity of beam,  $I$  the ionization potential and  $\beta = \frac{v}{c}$ .

The stopping power is inversely proportional to  $\frac{1}{v^2}$  and as the chlorine ions move through the target the stopping power increases as the projectile slows down. But because the target is thin, relatively small amount of energy, about 8.8 MeV is lost when moving through the entire depth of the target. Thus the beam energy remains well optimised for the production of <sup>192</sup>Tl.

In a fusion reaction the reaction products move along the beam direction. When a thin target is used the reaction products escape from the target and move away from the centre of the array of gamma-ray detectors. The clover detectors of the AFRODITE array are collimated, thus they cannot detect gamma rays emitted from nuclei far away from the centre of the array. In the present experiment contaminations in the data in the form of gamma-ray decays in <sup>192</sup>Hg produced after beta decay of <sup>192</sup>Tl were greatly reduced, since these gamma rays are emitted much later (half-life to the electron capture beta decay in <sup>192</sup>Tl is about 450ns), when the nuclei have already recoiled outside of the target position. A thick target on the other hand slows and stops the residual nuclei in the target, which is in the centre of the detector array, thus such a data set contains also gamma rays produced after a radioactive decay.

The use of a thin target introduces another complication. Since the reaction products are gamma decaying in motion Doppler effects occur (see below) and one should thus introduce a Doppler correction to the detected energies. Since the target is thin the residual nuclei recoil out of the target and move along the beam direction with speed approximately the same as the speed of the compound nucleus ( $\beta = 1.8\%$ ). This approximately constant speed and direction for all recoiling nuclei makes it possible to correct accurately for Doppler shift, preserving excellent energy resolution. In comparison when a thick target is used, the energy resolution may be worse due to Doppler broadening of the peaks. However, such Doppler broadening

can be used by DSAM (Doppler shift attenuation method) to extract lifetimes. The thick target also brings in much more Coulomb excitation (since we are not too far from the Coulomb barrier).

## 2.2 Gamma-rays in matter

Gamma quanta interact with matter in three fundamental ways. That is the photoelectric effect, Compton scattering and pair production. Each of these has a certain probability to occur. The attenuation in the number of gamma quanta inside a detector or material is a consequence of the three fundamental interactions. These three processes are at the basis of the detection of gamma quanta and also allow us to do different measurements of the properties of the gamma ray.

### 2.2.1 Photoelectric effect

Photoelectric effect happens when an incident gamma ray interacts with the electric field inside an atom, knocking one of the orbital electrons free in the process. The photoelectron is given a kinetic energy

$$T_e = E_\gamma - B_e \quad (2.3),$$

where,  $B_e$  is the binding energy of the electron and  $E_\gamma$  is the total energy of the incident gamma ray. The absorption probability is approximately given by  $\sigma_{pe} \cong 6 \cdot 10^{-37} \frac{Z^{4.5}}{E_\gamma^3}$ , with  $E_\gamma$  in MeV [Lab11]. This means that for a germanium detector  $Z=32$ , low energy ( $\sim 0.1$  MeV) photons are more probable to be absorbed than high energy photons ( $\sim 1.0$  MeV).

When a high energy gamma ray is absorbed it has enough energy to free inner shell electrons. A hole is created which is quickly filled by electrons from higher shells. This process produces characteristic X-rays which are reabsorbed very close to the site of the initial gamma ray absorption. These X-rays in turn free outer shell electrons that are very loosely bound. The kinetic energy of this outer shell electron is given by  $T_x \cong T_{e_x}$ , since the binding energy of the outer most electrons is negligibly small. These events occur in a very short time. Therefore the initial gamma-ray energy, i.e.  $E_\gamma = T_e + T_{e_x}$ , will be fully detected.



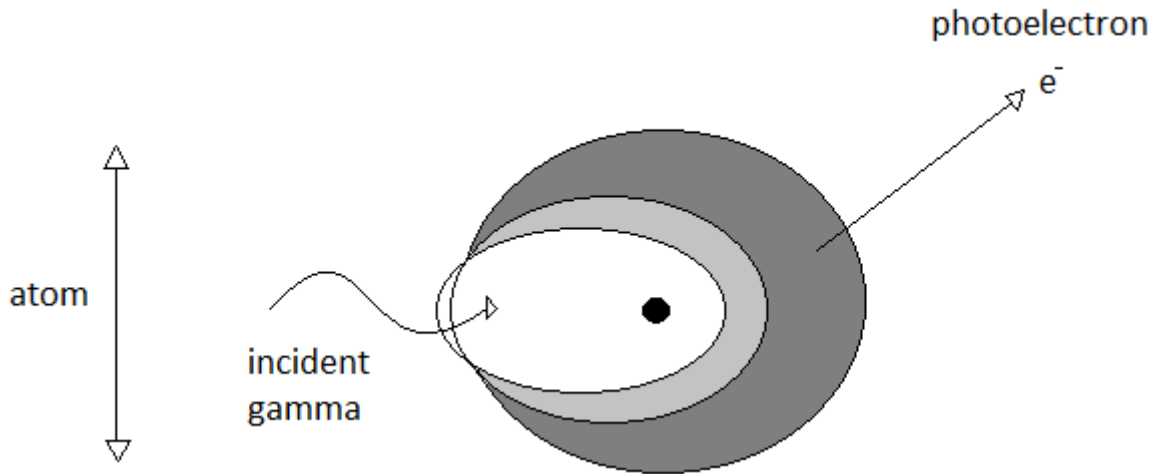


Fig 2-4 Schematic of the photoelectric effect, gamma ray interacts with the electric field in the atom, knocking out an electron.

### 2.2.2 Pair production

In the pair production process, incident gamma-rays interact with the electric field of the nucleus, forming an electron-positron pair (see Fig 2-5) [Kra88]. Only photons with energies greater than  $E_p = 1.022 \text{ MeV}$  can undergo pair production. The rest masses of the electron and positron are  $0.511 \text{ MeV}$  each. If a gamma photon with energy  $E_\gamma > E_p$ , undergoes pair production, the net energy  $E_\gamma - E_p$  is given to the pair as kinetic energy. Conservation of energy gives  $E_\gamma = T_+ + T_- + 2m_e c^2$ . The positron created in the pair production process loses its kinetic energy in the detector and quickly annihilates with a free electron, producing two gamma-rays emitted in opposite directions of  $0.511 \text{ MeV}$  each (see Fig.2-5). If these gammas in turn deposit their energy in the detector, the full energy of the gamma rays will be detected.

If one of the two gamma rays that are emitted in the annihilation process leaves the detector without interacting then energy of  $E_d = E_\gamma - 511 \text{ keV}$  will be registered. This peak in the spectrum is known as the single escape peak. If both emitted gamma rays leave the detector without interaction the energy of the gamma-ray registered in the detector will be

$E_d = E_\gamma - 1022 \text{ keV}$ . This peak is known as the double escape peak. The annihilation peak of  $511 \text{ keV}$  on the other hand comes from detecting  $511 \text{ keV}$  gamma ray, which is produced after the annihilation of the electron and positron (see Fig 2-6).

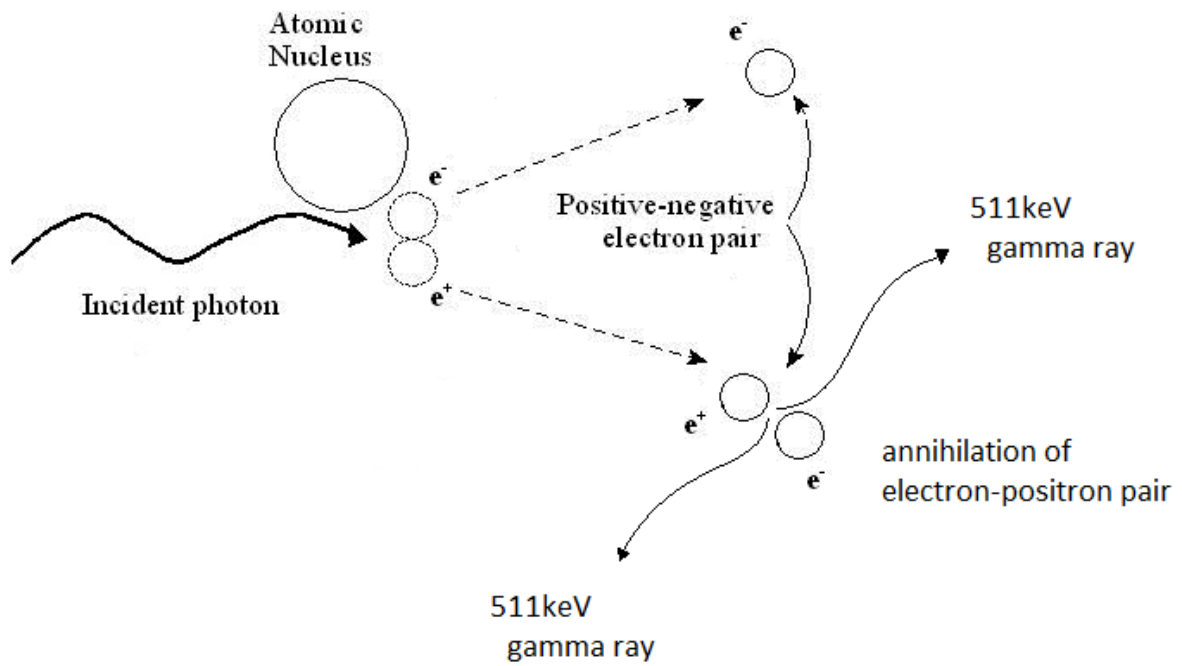


Fig 2-5 Production of electron-positron pair [Fer06]

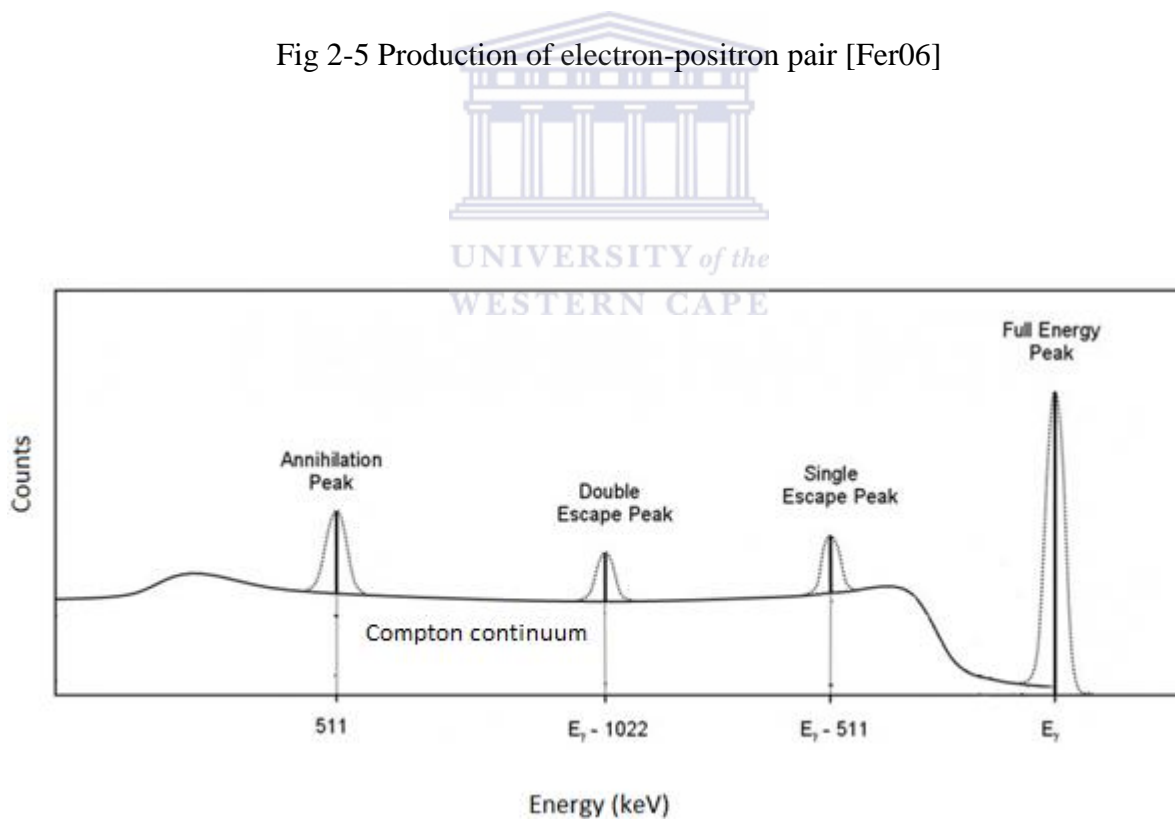


Fig 2-6 Showing peaks produced in pair production process, Compton continuum explained below [Gam11]

### 2.2.3 Compton scattering

Compton scattering occurs when an incident gamma photon scatters off an electron in the loosely bound outer shells of the atom. The incident photon gives part of its energy to the electron and in turn is scattered with a different frequency and energy. The Compton scattering formula is given by  $E_{\gamma'} = \frac{E_{\gamma}}{1+(E_{\gamma}/mc^2)(1-\cos\theta)}$  and the kinetic energy of the

scattered electron  $T_e = E_{\gamma} - E_{\gamma'} = \frac{E_{\gamma}^2(1-\cos\theta)}{mc^2+E_{\gamma}(1-\cos\theta)}$ , is expressed in terms of the angle  $\theta$  (as

shown in Fig. 2-7). If the recoil photon Compton scatters into another crystal of the clover detector, add-back can be used to infer the incident photon energy. One inherent consequence of Compton scattering is the possibility for the recoil photon to leave the detector. Therefore the full energy of the photon is not deposited inside the detector. This results in a Compton continuum background. Compton suppression can reduce this unwanted effect.

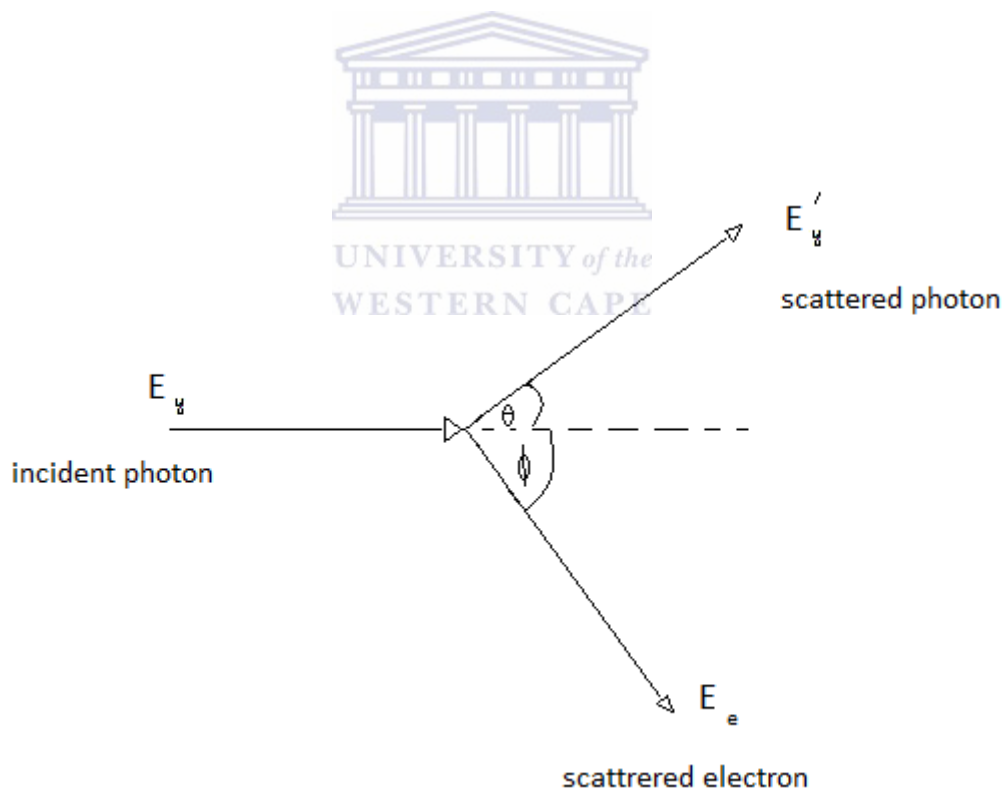


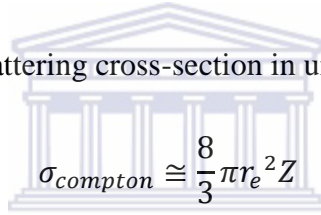
Fig 2-7 Compton scattering

## 2.2.4 Attenuation of gamma rays in matter

All three fundamental processes play a part when gamma rays move through matter. The intensity of the gamma rays decrease exponentially when moving through a material. This gamma ray intensity tells us how many gamma rays make it through the material without interaction. The intensity is a function of thickness  $x$  (cm) of the material already passed and  $\mu$  the mass absorption coefficient. This is given by  $I = I_0 e^{-\mu x}$ . The mass absorption coefficient can be written in terms of cross-section of the three fundamental processes, and is expressed as  $\mu = \frac{N_A}{A} (\sigma_{photoelectric} + \sigma_{compton} + \sigma_{pair})$ , where  $N_A$  is Avogadro's number,  $A$  is the atomic weight and  $\sigma$  are the cross-sections for each process [lab11]. An approximate expression for the photoelectric cross-section  $\sigma_{photoelectric}$  in units of  $m^2$  is given by

$$\sigma_{photoelectric} \cong 6 \cdot 10^{-37} \frac{Z^{4.5}}{E_\gamma^3}$$

When  $E_\gamma$  is in MeV, Compton scattering cross-section in units of  $m^2$  is



$$\sigma_{compton} \cong \frac{8}{3} \pi r_e^2 Z$$

for  $E_\gamma \ll m_e c^2$  where  $r_e = 2.82 \cdot 10^{-15}$  (in units of  $m^2$ ) is the classic electron radius and  $Z$  is the atomic number [Lab11]. If the gamma-ray energy  $E_\gamma$  and  $Z$  is the atomic number is much greater than the electron rest mass  $m_e c^2$  ( $E_\gamma \gg m_e c^2$ ) the Compton scattering cross-section in units of  $m^2$  is

$$\sigma_{compton} \cong \pi r_e^2 Z \frac{(1+2 \ln(2E_\gamma/m_e c^2))}{2E_\gamma/m_e c^2}$$

Finally the pair production cross-section in units of  $m^2$  is, [Lab11]:

$$\sigma_{pair} = Z^2 r_e^2 \frac{\ln\left(\frac{2E_\gamma}{m_e c^2}\right) - 2.6}{44}$$

## 2.3 Detection of gamma rays

### 2.3.1 Detectors

Nine high purity germanium detectors (HPGE) were used in this experiment. Four were placed at  $135^\circ$  with respect to the beam direction and five at  $90^\circ$ . Germanium is a

semiconductor. The germanium crystal has a cubic close-packed structure as shown in Fig. 2-8.

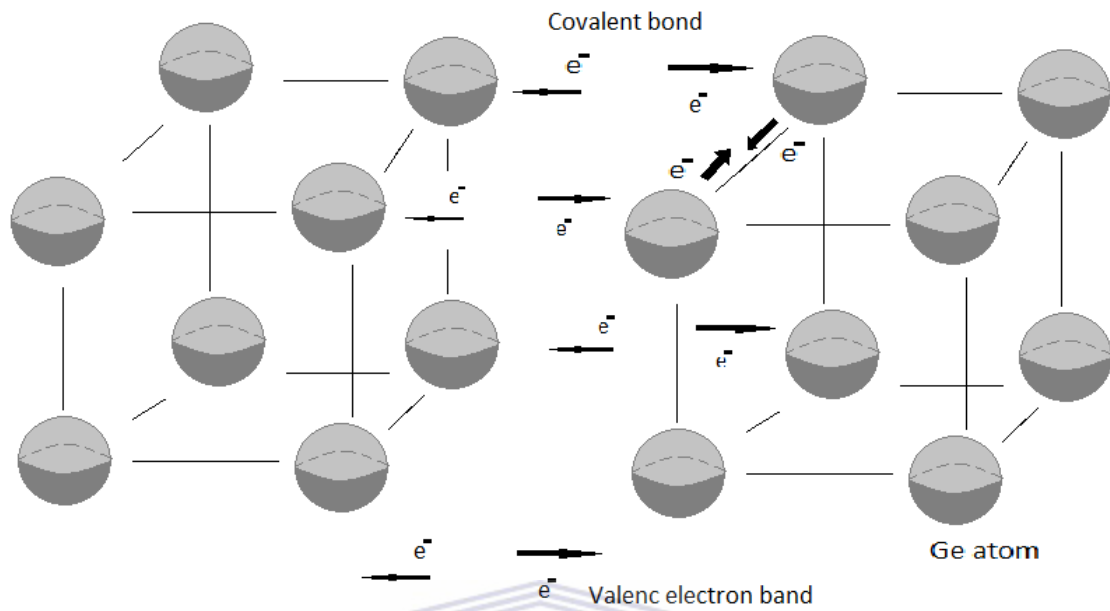


Fig 2-8 Cubic structure of Ge crystal

It has an electron configuration of  $[\text{Ar}] 3d^{10}. 4s^2. 4p^2$ . The  $4p^2$  level is 3-fold degenerate and each atom has two valence electrons free to form covalent bonds with neighbouring atoms. Covalent bonds are formed when neighbouring atoms exchange valence electrons (see Fig.2-8). This is known as the valence band. A conduction band exists for electrons not used for covalent bonding i.e. the shells below valence band. The conduction band is seen as an empty band. For semiconductors like germanium, this band gap is approximately 1eV (see Fig.2-9) [Kra88].

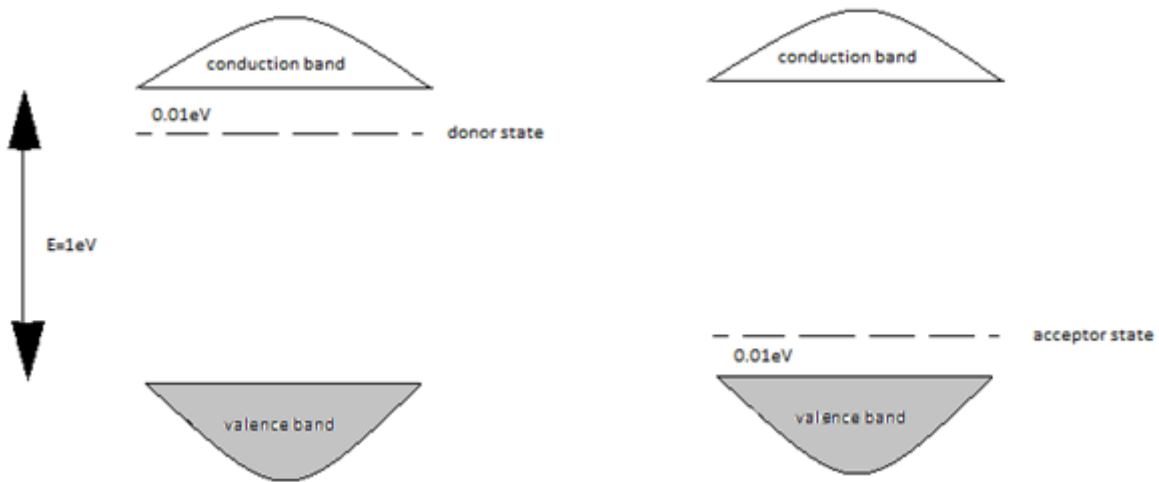


Fig 2-9 Valence and conduction bands

At room temperatures a small amount (one in  $10^9$ ) electrons can be thermally excited across the band gap leaving a hole behind, making the Ge somewhat conductive. To control electrical conduction in semiconductors, small amounts of material called dopants are added [Kra88]. Dopants with five valence electrons are added to the Ge crystal lattice. Four of the valence electrons form covalent bonds with neighbouring Ge atoms and the fifth electron fills the holes of thermally excited electrons. The rest migrate to the conduction band forming a donor state (as shown in Fig. 2-9) [Kra88]. This type of semiconductor is called n-type (because of the excess of negative charged carriers). If dopants with three valence electrons are used, an excess of holes is created above the valence band. These types of semiconductors are called p-type (excess of positive charged holes) (see Fig 2-10) [Kra88].

An electric field is created when p-type and n-type semiconductors are brought together (see Fig.2-10). This electric field is created when electrons from the donor state fill holes in the acceptor state, leaving behind a positive space charge. Similarly holes migrate to the donor state leaving behind a negative space charge. The electric field stops the migration of other charge carriers and creates a depletion region (see Fig. 2-10) [Kra88].

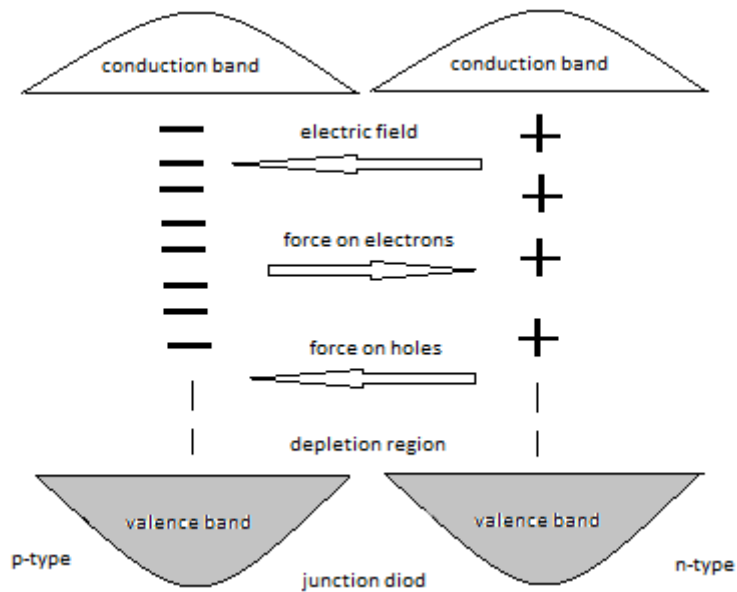


Fig 2-10 A junction diode between p and n type semiconductors

The detectors used in this experiment have n-type material on the inside of the detector and p-type materials on the outside. It is designed this way to prevent attenuation of gamma-rays since the n-type semiconductor is thicker than the p-type. When a gamma ray enters the depletion region it creates an electron hole pair. The electron moves in one direction and the hole in the other. The total number of electrons and holes collected forms a signal pulse, which is proportional to the energy of the incident gamma-ray.

The Ge detectors operate at a high voltage of 1000V-4000V. This has two effects. First, it increases the magnitude of the electric field in the depletion region, making the collection of charge more efficient. Second, by increasing the depletion region it increases the sensitive volume of the detector.

When in operation the Ge detectors are kept cool at liquid nitrogen temperatures. This is to reduce noise in the system. Each of the nine detectors is made out of four Ge crystals shown in Fig. 2-11.

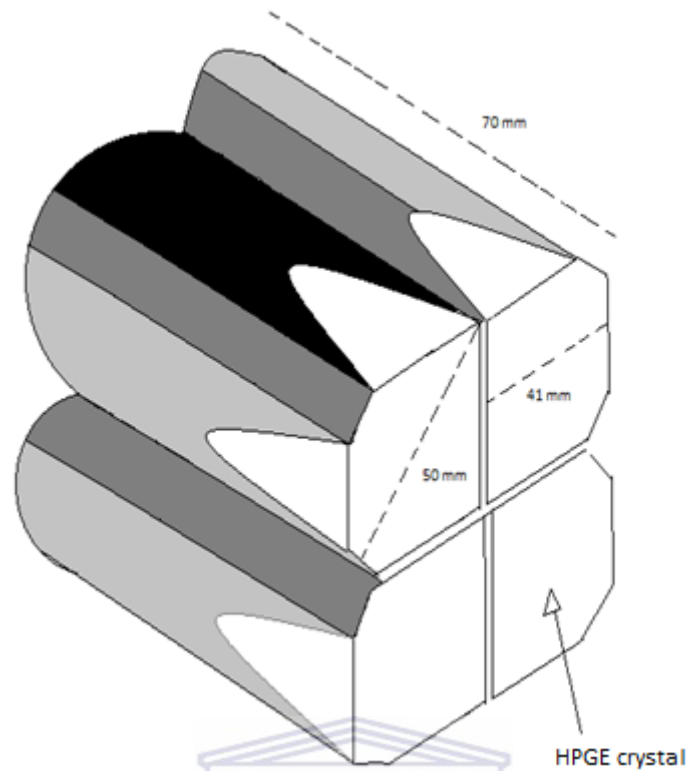


Fig 2-11 Clover Germanium Detector



The use of clover detectors makes linear polarization measurements possible and improves Doppler broadening. Linear polarization is important because it tells us if a transition is electric or magnetic in nature. It is applicable when a gamma-ray hits a crystal of the clover detector (preferably at  $90^\circ$  to the beam direction) and Compton scatters into another crystal where it is absorbed (known as a double hit event), as shown in Fig. 2-12. On average more gamma rays scatter perpendicular to the electric field vector  $\vec{E}$  of the gamma-ray radiation [Law11]. Knowing the Poynting vector  $\vec{p}$ , and measuring the direction of  $\vec{E}$  from the number of double hit event scattered vertically and horizontally one can infer the electric or magnetic nature of the transition (see Fig. 2-12).



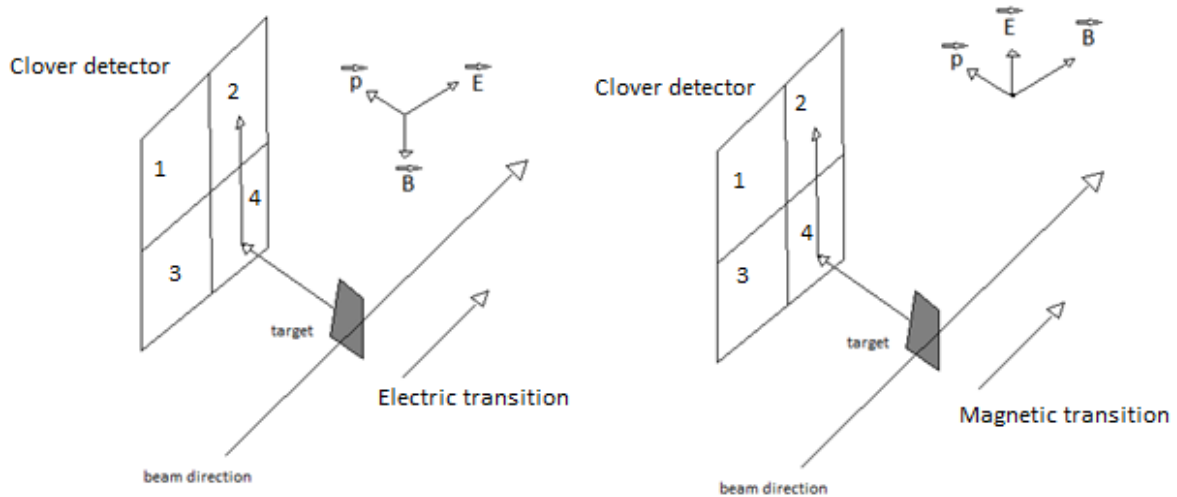


Fig 2-12 Linear Polarization

A consequence of the use of large volume detectors is potential Doppler broadening. Doppler broadening decreases the resolution of photo peaks. It is a function of the opening angle of the detector  $\Delta\theta$  and is expressed as  $\Delta E_\gamma = E_0 \frac{v}{c} \sin(\theta) \Delta\theta$ , where  $E_0$  is the gamma-ray energy,  $\theta$  is the angle of the detector,  $v$  is the velocity of the residual nucleus and  $c$  is the speed of light (see Fig. 2-13). Using composite detectors decreases the opening angle  $\Delta\theta$ , improving the peak resolution (see Fig. 2-15).

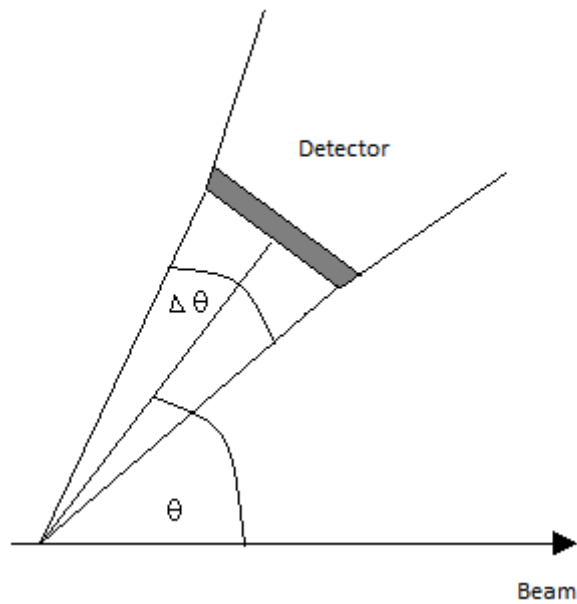


Fig 2-13 Show the opening angel  $\Delta\theta$  for a detector placed at an angle needed to calculate Doppler broadening

Another consequence of the use of a composite clover detector is the need to take into account the add-back. This is important when a gamma ray Compton scatters from one crystal to another. In these cases the gamma-ray deposits part of its energy in one crystal and after scattering deposits the rest of its energy in another crystal. To account for this the method of add-back is employed. If the scattered events happen in a predetermined time interval the energies registered in each crystal are added, which improves the ratio of photo peak efficiency and the total efficiency (see Fig. 2-14). This makes the spectrum cleaner since the add-back eliminates a part of the Compton continuum background. Low-energy gamma rays typically have a lower probability to Compton scatter. This is clearly seen from the efficiency plot as a function of energy (see Fig 2-14).

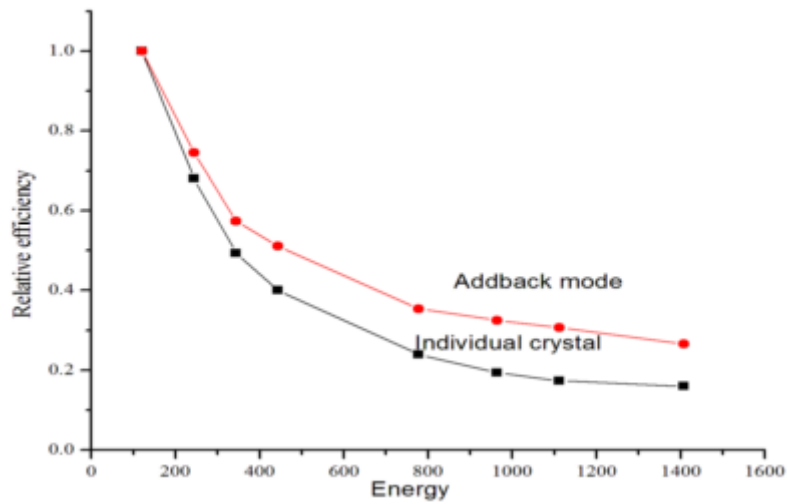


Fig 2-14 Relative efficiency as a function of gamma energy [Pra10]

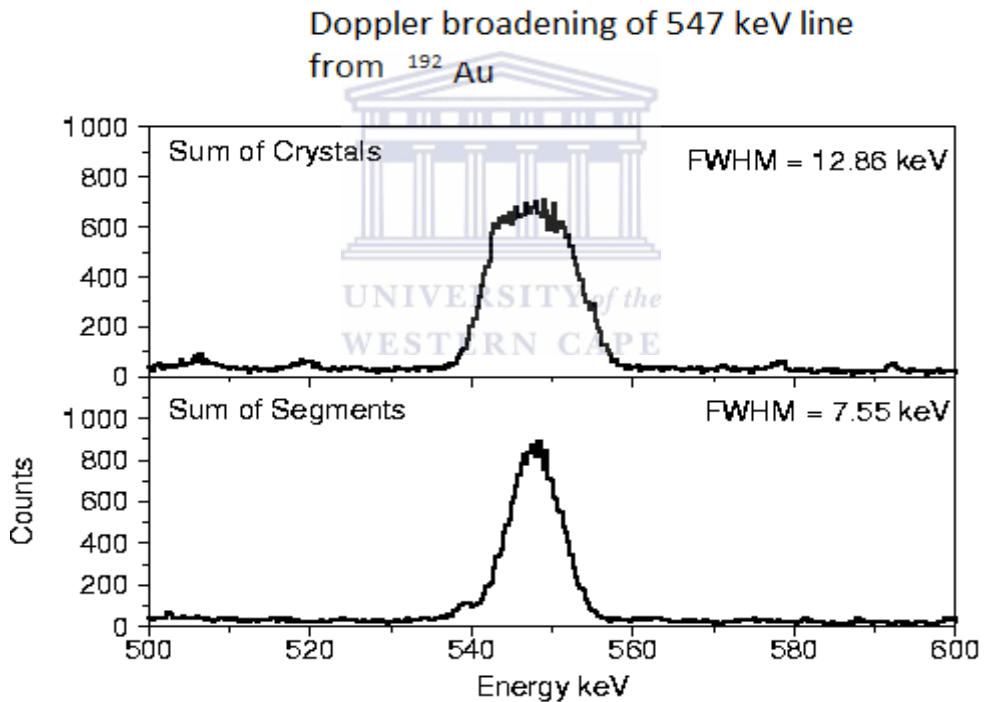


Fig 2-15 Doppler Broadening [She98]

### 2.3.2 Compton suppression

The HPGE detectors are often surrounded by bismuth germanate shield (BGO) (see Fig. 2-16). The BGO is a scintillating detector which vetoes the signals of the HPGE detector when both fire in coincidence. When a gamma ray Compton scatters out of the HPGE crystal, only part of its energy is deposited in the crystal. Another part of the scattered gamma-ray energy

is deposited in the BGO. Rejecting these gammas that deposit part of their energy in the HPGE crystal reduces the Compton continuum background.

Heavy metal collimators are placed in front of the BGO detectors. This is to prevent the detection of gamma rays which have not scattered from the Ge crystal. Without such collimators one may veto good events, if two gamma rays are detected simultaneously in the Ge crystal and in the BGO shield.

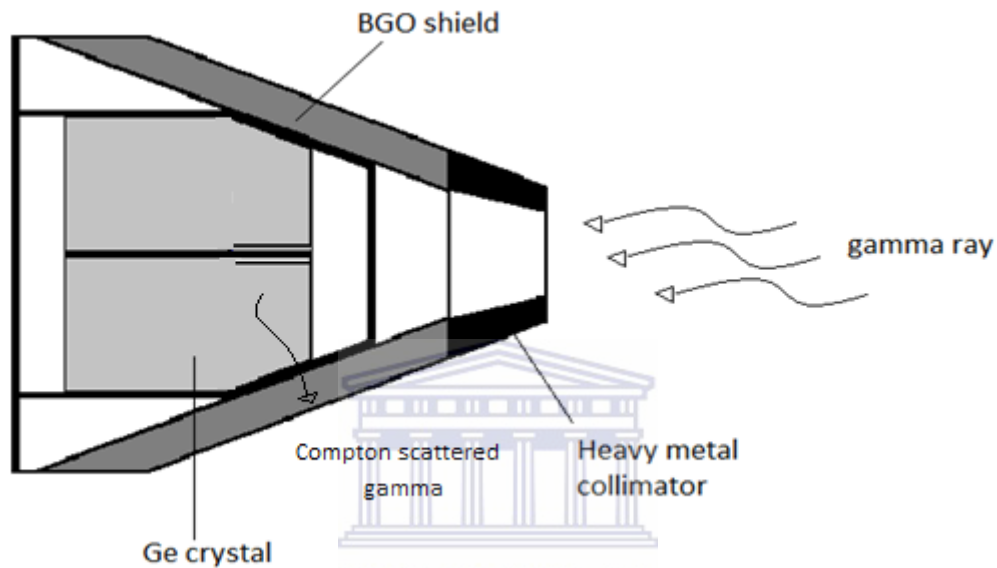


Fig 2-16 BGO shield of the clover detector [Exo11]

### 2.3.3 Detector Placement

For this experiment five clover detectors were placed at  $90^\circ$  and four at  $135^\circ$ . Such placement maximizes the detection efficiency of both E2 and M1 transitions. The angular momentum  $L$  carried away by the gamma ray has projection  $m$ . The intensity of the radiation emitted at different directions in space is the angular distribution of the gamma ray  $S_{Lm}(\theta, \varphi)$ . The angular distributions are in fact functions of associate Legendre polynomials:

$$P(\cos\theta)_2 = P_2 = \frac{1}{2}(3\cos^2\theta - 1) \text{ and } P(\cos\theta)_4 = P_4 = \frac{1}{8}(35\cos^4\theta - 30\cos^2\theta + 3).$$

For  $L=2$  the value of  $m$  are  $m=-2, -1, 0, 1, 2$ . The angular distributions for dipole and quadrupole transitions are shown in Fig. 2-17 [Law11] and are given by

$$S_{10} = \frac{1}{4\pi}(1 - P_2), S_{1\pm 1} = \frac{1}{4\pi}\left(1 + \frac{1}{2}P_2\right),$$

$$S_{20} = \frac{1}{4\pi}\left(1 + \frac{5}{7}P_2 - \frac{12}{7}P_4\right) S_{2\pm 1} = \frac{1}{4\pi}\left(1 + \frac{5}{14}P_2 + \frac{8}{7}P_4\right),$$

$$S_{2\pm 2} = \frac{1}{4\pi}\left(1 - \frac{5}{7}P_2 - \frac{2}{7}P_4\right).$$

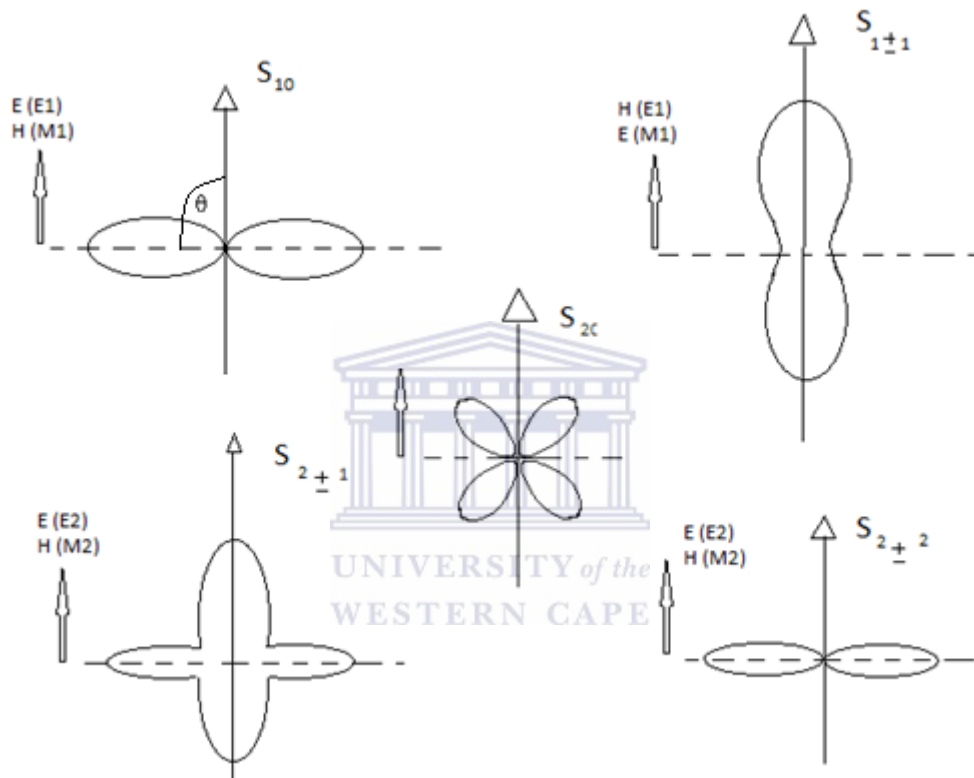


Fig. 2-17 Angular distribution of pure dipole and quadrupole transitions

Consider a fusion evaporation reaction (see Fig. 2-18). Compound nuclei are formed with angular momentum ( $\vec{I} = \vec{r} \times \vec{p}$ ) perpendicular to the beam direction where  $\vec{p}$  is the momentum of the projectile and  $\vec{r}$  is the impact parameter. The angular momentum has an equal probability to point in all directions in the plane perpendicular to the beam axis. The compound nuclei decay by emitting light particles in random directions, which carry away only a small amount of angular momentum. After emitting light particles residual nuclei are

formed. They still carry most of the original angular momentum and remain at a high excitation energy. At this point the angular momentum vector is changed by a very small amount. Therefore in this type of reaction there is a strong orientation of the angular momentum  $I_f$  of the residual nuclei. The angular distribution of gamma rays emitted by nuclei produced in fusion-evaporation reactions is given by

$$W(\theta) = 1 + \sum_{k-\text{even}} \alpha_k A_k(I_f, I_i, L, L') P_k(\cos \theta),$$

where  $L' = L + 1$ ,  $k_{max} = \min(2I_f, 2I_i, L + L')$  and  $\alpha_k$  are attenuation coefficients.  $A_k$  are theoretically calculated coefficients, which depend on the initial and final nuclear spins. The angular distribution function  $W(\theta)$  for pure stretched dipole and quadrupole transitions has a maximum at  $90^\circ$  and  $0^\circ$ , respectively (see Fig. 2-19) [Law11].

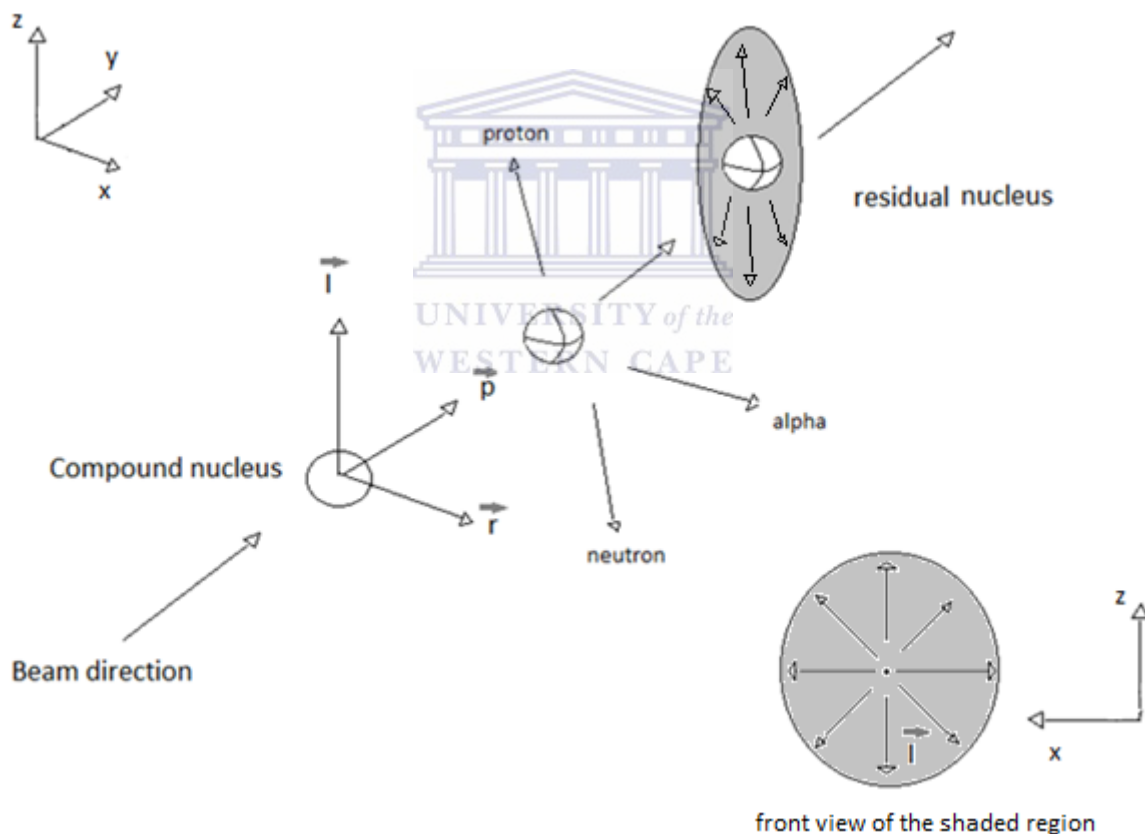


Fig. 2-18 Schematic of a fusion evaporation reaction showing that the angular momentum of the compound nucleus lies in the plane perpendicular to the beam direction

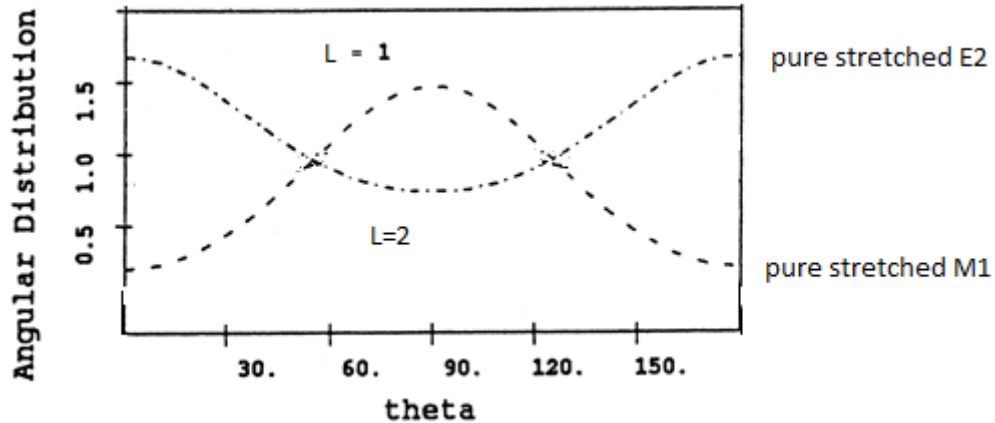


Fig 2-19 Angular distribution functions for stretch dipole and quadrupole transitions [Ran06]

#### 2.3.4 **AFRODITE array**

The AFRODITE array has 16 detector positions relative to the beam. Detectors can be placed at 45°, 90° and 135°. No detectors were placed at 45° for this experiment. Four detectors were placed at 135° and five at 90° (see Fig. 2-20b). As it is seen in Fig 2-20a, the target chamber is the centre of the array. It has micron kapton windows which are transparent to gamma rays, as seen in Fig. 2-20a. In our experiment the kapton windows were replaced with aluminium windows in order to achieve a better vacuum. The detectors are placed in front of these windows.

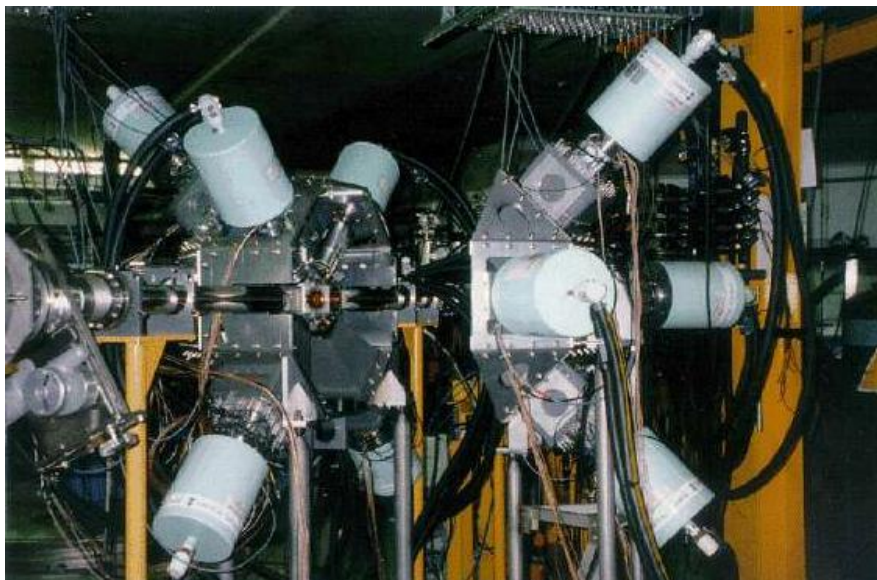


Fig 2-20a AFRODITE array with HPGE clover detectors and LEPS detectors (low energy gamma ray detectors not used in this experiment)

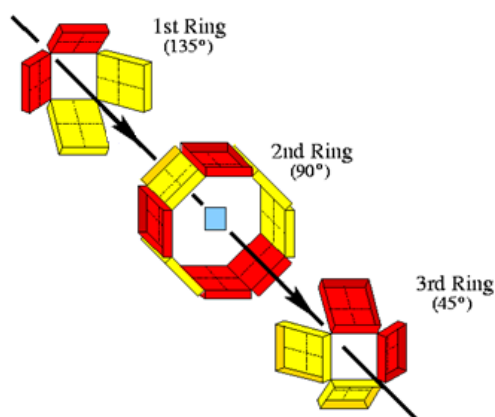


Fig 2-20b bottom schematic of the detector placement possible [Haw98]

### 2.3.4 Absorbers

X-rays are very frequently emitted in heavy-ion-induced collisions. They take away processing power which could be used to process more useful data. Eliminating as much of the X-rays as possible frees up the data acquisition so that more good data can be collected. Absorbers were placed in front of the nine detectors to decrease the yield of X-rays coming from the residual thallium nuclei ( $K_{\alpha} = 70\text{keV}$ ,  $72\text{keV}$  and  $K_{\beta} = 82\text{keV}$ ) produced in the reaction due to internal conversion of K-shell electrons.

The internal conversion process occurs when nuclear excitation energy is transferred to an atomic electron. The electron is ejected and the hole is quickly filled by a higher-shell electron, emitting a X ray in the process. These X-rays are characteristic of the Z of the residual nuclei in our case thallium isotopes. In this experiment 0.15 mm tin (Sn) absorber was placed on top of 0.07 mm brass (copper zinc alloy) absorber.

The linear mass attenuation coefficient  $\frac{\mu(\lambda)}{\rho}$  is a function of the gamma-ray wavelength  $\lambda$ , where  $\rho(\text{g}/\text{cm}^3)$  is the density of the absorber. For X-rays the primary mode of absorption is the photoelectric effect with Compton scattering being negligibly small and pair production vanishing since it can only occur for energies  $\geq 1.022$  MeV. The mass attenuation coefficient is given by  $\frac{\mu(\lambda)}{\rho} = \frac{N_A}{A} \sigma_{photoelectric}$  [Lab11]. Therefore to successfully stop 50% of the thallium 82 keV K-shell X rays



$$d_{1/2} = 0.69 \left( \frac{N_A}{A} \sigma_{photoelectric} \right)^{-1}$$

Tin has a  $\rho = 7.29 \text{ g/cm}^3$  gives, that gives

$$d_{1/2} = 0.69 \left( (7.29) \frac{6.2 \cdot 10^{23}}{119} 6 \cdot 10^{-37} \cdot 50^{4.5} (8.3 \cdot 10^{-2})^{-3} \right)^{-1} = 0.39 \text{ mm}.$$

Placing absorbers that are too thick may completely absorb low energy gamma rays. A balance is needed to reject some of the X-rays in order to avoid collecting too many gamma-X-ray coincidences but to allow low energy gamma rays to be still present in the data.

## 2.4 Electronics-basic ideas

### 2.4.1 Energy measurements

When a gamma ray deposits its full energy into the clover detector the number of electrons released in the interaction is proportional to the incident gamma-ray energy. These electrons are in turn directed by the electric field inside the clover detectors towards the electrodes, where a charged pulse is collected (see Fig. 2-21). The integrated charge pulse amplitude is proportional to the incident gamma-ray energy. This charge pulse is usually very weak and it needs to be amplified and shaped. The HPGE clover detector has a built in preamplifier that integrates the charge pulse and converts the pulse into a voltage pulse. This conversion is done with an integrating capacitor. The capacitor is placed in parallel with a discharge resistor. This gives the output signal a fast rise time and long decay time  $\tau = RC$  (see Fig. 2-22). The energy of the incident gamma is still preserved in the amplitude of the output voltage pulse  $V_{out} = \frac{Q}{C}$ . At this point the output voltage pulse needs to be shaped. This is done by an amplifier. The amplifier gives the voltage pulse a Gaussian shape with amplitude still proportional to the incident gamma-ray energy (see Fig. 2-23). The shaping of the voltage pulse may not be perfect. An overshoot or undershoot can occur. This needs to be corrected and is referred to as pole zero correction (see below) [Cae11].

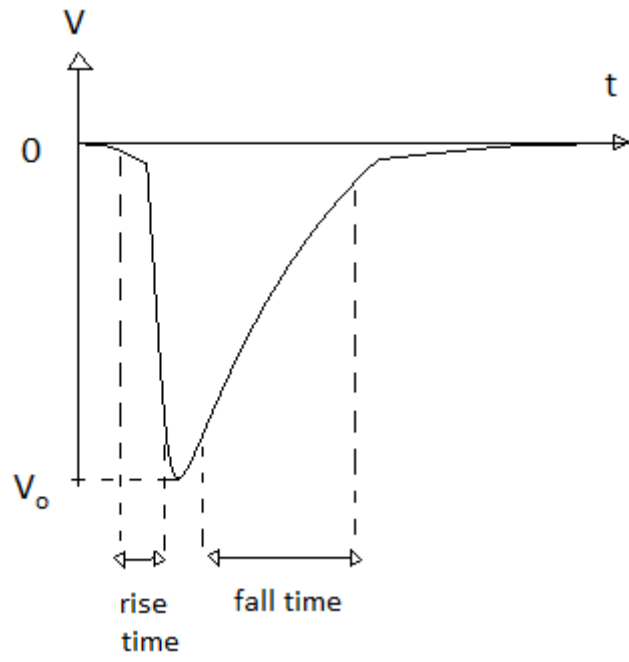


Fig 2-21 Charge pulse from the clover detector

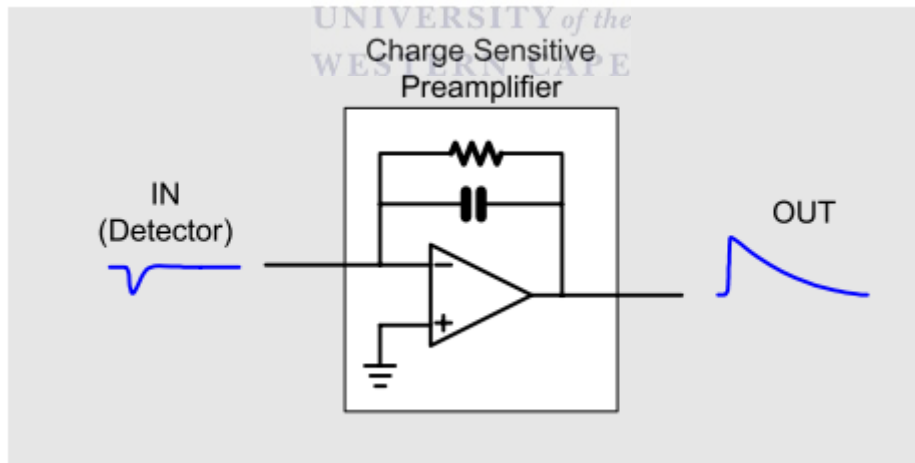


Fig 2-22 Output integrated voltage pulse [Cae11]

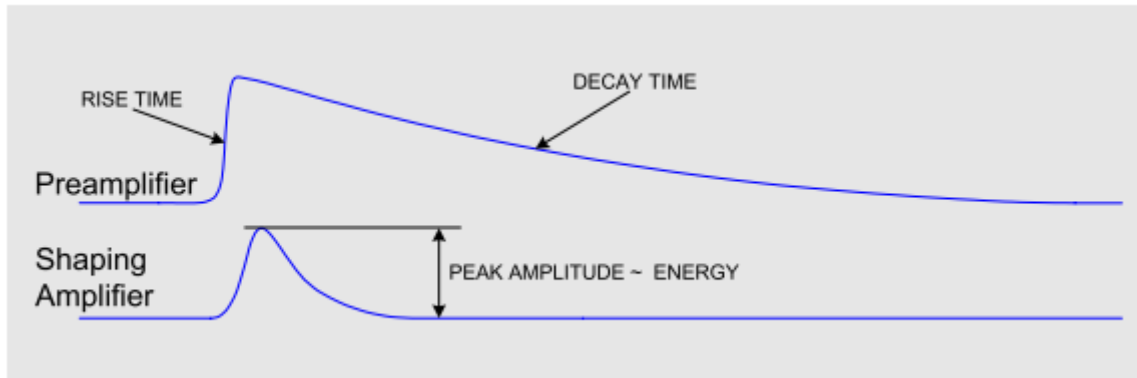


Fig 2-23 Amplifier signal after shaping [Cae11]

From here the voltage pulse is converted into a digital signal with the aid of an ADC (analogue to digital converter). The ADC converts the voltage pulse amplitude to a digital number. This number is proportional to the amplitude. Consider an example. Suppose the ADC accepts input voltage in the range 0-10 V and outputs digital numbers in the range 0-1000. This means that a 2.5 V = 2500 mV signal would be converted to the digital number 250, i.e. 10 mV per digit [Ele06]. Once the voltage amplitude is digitised it is passed to the data acquisition system which sorts the digital number and increments the counts in that particular channel. Thus the channel number is proportional to the amplitude of the signal and therefore to the gamma-ray energy. The data acquisition system records and displays this information in a histogram.

#### 2.4.2 Timing circuits

Not only is the energy of the gamma ray important but the time when it is detected is important too. Timing allows us to do coincidence measurements, which helps us for example to build level schemes. The fundamental operation in a timing measurement is the generation of a logic pulse whose leading edge indicates the time of occurrence on the input pulse [Ele06]. A threshold level is set that allows a logic pulse to be registered once the signal voltage passes the threshold voltage. Anything below the threshold is ignored (see Fig. 2-24) [Ele06].

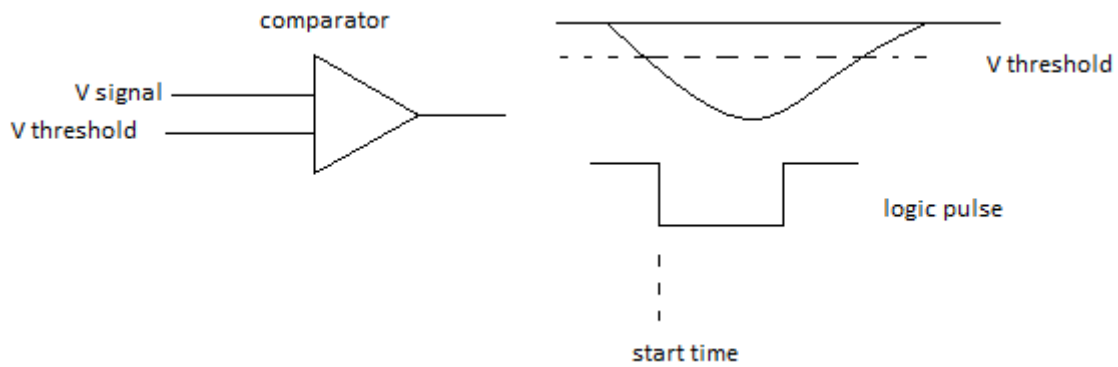


Fig 2-24 Logic pulse above the threshold

This method of triggering has inherent in it two problems, amplitude walk and time jitter. Amplitude walk can occur when two incoming coincident pulses differ in amplitude and/or rise time. The difference in amplitude causes the discriminator to trigger at different times even though the signals are exactly coincident. Noise and statistical fluctuations in the detector signal can cause timing fluctuations. This can cause two identical signals to trigger at different points. This time variation is dependent on the amplitude of the fluctuation. This effect is called time jitter. To minimise these problems in this experiment a CFD (constant fraction discriminator) was used. The incoming pulse is first split into two. One part  $V_a$  is delayed by a time  $T_d$  the signal takes to rise from a constant fraction level to the pulse peak [Ele06]. The second part is inverted and attenuated by a factor  $f$  to give a pulse  $V_c = -fV_a$ . The two pulses are summed to produce a bipolar pulse whose zero crossing is the start time of the logic pulse (see Fig 2-25).

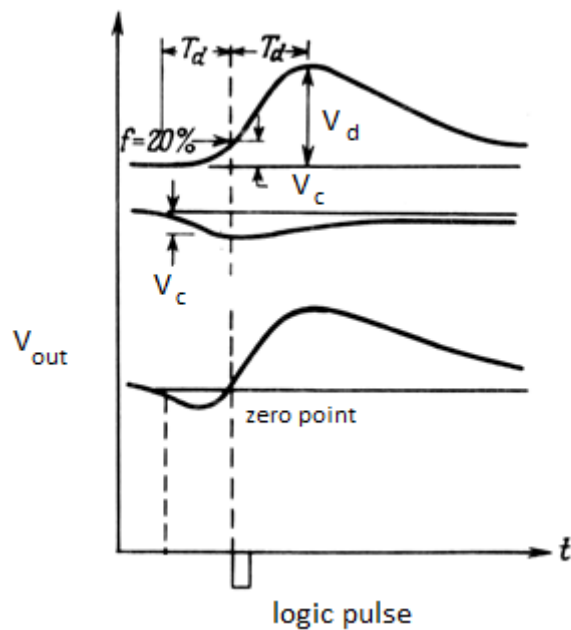


Fig 2-25 CFD showing the transformation of the input pulse into a bipolar output pulse

[Kol11]

Coincidence electronics are then used to do coincidence measurements. The coincidence window for each clover detector was set to 150 ns, i.e. the length of time within which the logic signals from other detectors firing in coincidence should arrive. The logic signal from all detectors are summed if the amplitude of this summed signal passes a threshold a coincidence measurement is registered. If for any reason the sum was less than the threshold the event would be ignored (see Fig. 2-26). The threshold corresponds to the required number of detectors in coincidence. For this experiment it was two gamma rays in coincidence.

The coincidence window of 150 ns was chosen to prevent random coincidences summing. Random coincidences may occur if gamma rays from the decay of two different nuclei (usually produced by consecutive beam pulses) arrive within the coincidence window. Although they will then be considered as belonging to the same decay path, in fact these are random coincidences. The probability for random coincidences depends on the production rate of the excited nuclei, on the multiplicity of the gamma-ray cascade, on the solid angle covered by the detector array, and also on how long the coincidence window is [Dra96]. One can decrease the probability for random coincidence by decreasing the coincidence window but if it becomes too short one starts losing efficiency for detecting low energy transitions, which in principle need longer time for charge collection [Dra96]. With coincidence window

of 150 ns the probability for random coincidences in the AFRODITE array is small, while the efficiency for low energy transitions is still good.

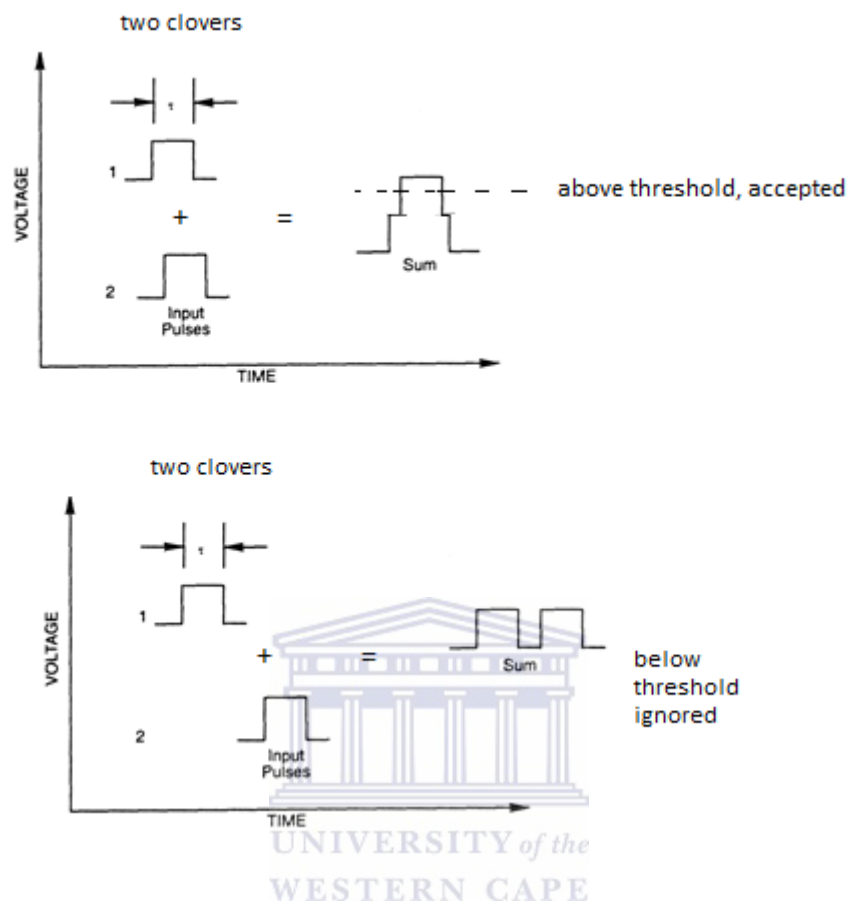


Fig 2-26 coincidence electronics, top two gamma rays in the coincidence window, while bottom the second gamma ray is outside the coincidence window. [Kol11]

### 2.4.3 Pole Zero adjustment

Between consecutive experiments (two weeks or more) settings of the electronics may change. Adjusting the pole zero was thus a necessity for this experiment. Many factors may affect electronics. These include temperature fluctuations and more intrusive factors like turning equipment on and off, moving detectors around and so on. Adjusting pole zero brings the right hand side of the signal peaks to the zero-baseline. A primary cause of both is the RC pulse shaping which is done by differentiation of the tail pulse coming from the preamplifier of the detector [Ele06]. Each pole zero needs to be adjusted correctly because it may influence the pulse amplitudes. A pole zero needs adjusting when the tail of the signal pulse undershoots (below the Fig. 2-27) or overshoots (above the zero baseline Fig. 2-27). This

affects the second signal pulse which rides on the first pulse undershoot, consequently changing the measured pulse amplitude and therefore the detected gamma-ray energy.

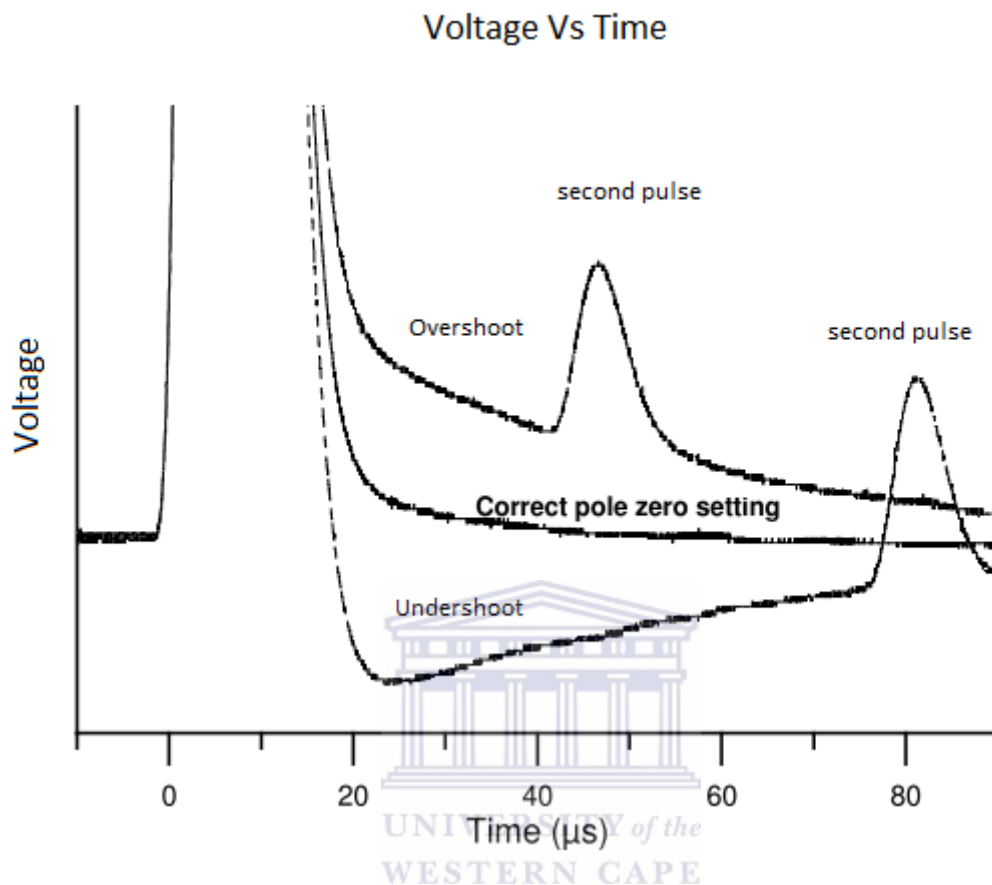


Fig 2-27 Correct pole zero setting and setting causing overshoot and undershoot [Bru11]

#### 2.4.5 Threshold

The threshold is an electronic level that is set to minimise the intrinsic noise being detected. Setting this level too high might exclude low energy gamma rays that are just above the noise. Setting it too low lets some noise to come through and leads to collecting unwanted coincidence events. This results in less computer processing time for the events of interest.

#### 2.4.6 Trigger and Gamma-Gamma coincidence

For this experiment, the trigger selected two gamma rays within a coincidence window of 150 ns. The trigger is an electronic gate set to count signal pulses in a specific time interval. When an excited nucleus decays, the decays happen consecutively in a very short time. A typical Weisskopf estimate for the life-time of an electric quadrupole transition is given by

$\frac{1}{\lambda(E2)}$  where  $\lambda(E2) = 7.3 \cdot 10^7 A^{4/3} E^5$ . For  $^{192}\text{Tl}$  and an E2 energy transition of 1 MeV, gives a life-time =  $\frac{1}{\lambda(E2)} = (7.3 \cdot 10^7 \cdot 192^{4/3} (1 \text{ MeV})^5)^{-1} \approx 1 \text{ ps}$ . Therefore the life-time of a typical nuclear transition is very much shorter than the trigger window. Thus the whole gamma ray cascade corresponds to the whole nuclear decay path is emitted in much shorter time than the coincidence window. Since the small number of detectors and the relatively small photo peak efficiency of the AFRODITE array (1.8% at 1.3 MeV) only a small number of all total gamma rays emitted are usually counted. In most experiments the AFRODITE array is most effective when detecting two gamma rays in coincidence.

The number of detected events also depends on the dead time in the data acquisition. Dead time is the time when the system is busy processing data and cannot accept any incoming new events.

For a  $E_\gamma - E_\gamma$  coincidence measurement to work a minimum of two detectors are needed. In a  $E_\gamma - E_\gamma$  experiment, two gamma photons from the same decay path enter each detector separately. Since they meet the trigger condition of two gamma rays detected within a 150 ns coincidence window, the event is accepted and recorded by the data acquisition. This experiment requires at least two gamma rays within the coincidence window of 150 ns. The coincidence data rate was typically close to 5 kHz and the dead time was about 30%, while the count rate in a single clover detector was  $\sim 25 \text{ kHz}$ .

The electronics needed to process signals coming from the clover detectors is built in the RIS clover modules. All electronics needed for digitising both the time and energy signals, while at the same time can veto unwanted signals if the BGO signal that arrive in coincidence is done by the electronics in the RIS modules. These modules can monitor and have controlling capabilities, which includes the ability to adjust the pole zero. With these modules it is also possible to set the CFD and BGO thresholds. They can also monitor Compton suppression Ge signals and other signals (like LEPS signals when applicable). Trigger windows need to be set separately. Logic signals carrying information about whether the trigger condition is met are fed into the RIS modules for processing. Data from the RIS modules are passed on for further processing to MIDAS data acquisition system through FERA read-out ribbon cables.



### 3 **Chapter 3 Preliminary data analysis**

#### 3.1 **Data Acquisition**

MIDAS [Mid11] is a software package that was used to set parameters to the RIS clover modules, to control, collect and monitor data, to sort and construct all online spectra and  $E_\gamma - E_\gamma$  matrices and also in the offline analysis. When starting MIDAS for this experiment, it was necessary to include the following apparatus: the tape server, CAMAC, VME histograms and VME modules. The tape server controls all the flow of the incoming data, including a 40-80 Gb digital linear tape that records the raw data. The VME histogram allows us to visualise the raw data that is collected into histograms. Every two hours all histograms were saved in separate directories. This was done in case one had to compare data collected in different runs. Three tapes were used in this experiment for the 144 hours of beam time. The tapes were then copied to hard disk and stored for future use. The CAMAC bins hold mostly computer controlled modular electronics and in particular the RIS clover modules. All communications with CAMAC bins are controlled by the crate controller, with the host computer being pistol, linked to the crate controller. Many CAMAC crates can be connected in series or in parallel. All of them are controlled by the one host computer. VME on the other hand can be controlled by multiple hosts. Each crate could be controlled by a computer, making them a much faster system.

MIDAS was also used to do online sorting. In this case, the host computer (pistol) is linked to another computer (feste) which process data coming in live. The online sort gain matches the data and sorts it into matrices and spectra. Online spectra and matrices are saved directly to hard disk at the end of the beam time. Online spectra and matrices are used to monitor the data through initial rough sorting and to assess its quality while the experiment is running.

Once the experiment was completed offline sorting was done to build various matrices. Depending on the kind of measurements one wants to do, different matrices are needed. For this experiment a level scheme was one of the main objectives, so sorting a  $E_\gamma - E_\gamma$  matrix was most important.

### 3.2 $E_\gamma - E_\gamma$ Matrix

To construct a  $E_\gamma - E_\gamma$  matrix we select events in which, at least x number of gamma rays are in coincidence. To build a  $E_\gamma - E_\gamma$  matrix x should be greater or equal to two. Consider the case of x=3 for example. If  $E_{\gamma_1}$ ,  $E_{\gamma_2}$  and  $E_{\gamma_3}$  are energies of gamma rays in coincidence, then all possible pairs of gamma are formed.  $(E_{\gamma_1}, E_{\gamma_2})$ ,  $(E_{\gamma_1}, E_{\gamma_3})$ ,  $(E_{\gamma_2}, E_{\gamma_1})$ ,  $(E_{\gamma_2}, E_{\gamma_3})$ ,  $(E_{\gamma_3}, E_{\gamma_1})$  and  $(E_{\gamma_3}, E_{\gamma_2})$ . Each pair is placed on the x-y axes while z coordinate is the number of times this pair was encountered in the data. Since the number of  $(E_{\gamma_1}, E_{\gamma_2})$  pairs is equal to the number of  $(E_{\gamma_2}, E_{\gamma_1})$  pairs the z coordinates are identical incremented in the same way with each event. Therefore the  $E_\gamma - E_\gamma$  matrix formed in this way is symmetric with identical x and y projections (see Fig 3-1).

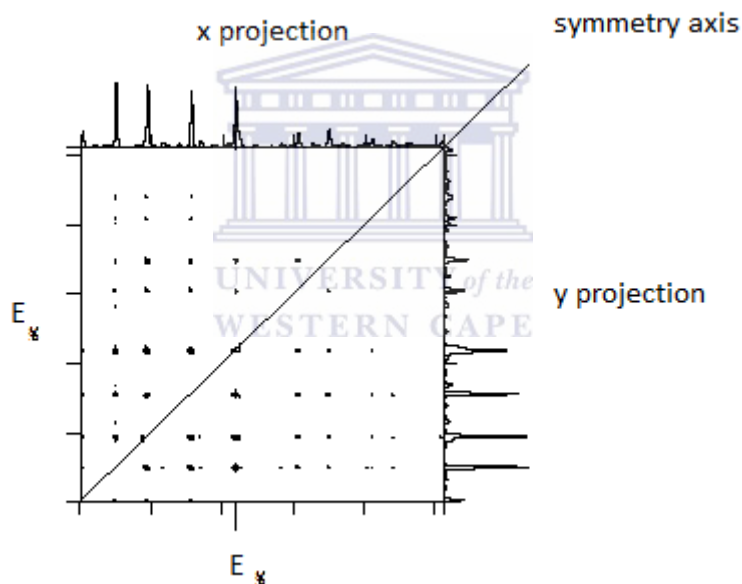


Fig 3-1  $E_\gamma - E_\gamma$  matrix, the dots being counts on z-axis [Dra96]

### 3.3 Data analysis

#### 3.3.1 Programs

MIDAS data acquisition uses a sort code with a unique syntax, called MTsort. When the sort code is loaded MIDAS checks the syntax and translates it into C language. The MTsort code is thus compiled and the commands are executed. Once the sorting is complete and matrices

are constructed, Radware software package [Rad00] was used for building the level scheme. This is a software package specifically designed for gamma spectroscopy analysis.

When the two weekend of data were sorted into two  $E_\gamma - E_\gamma$  matrices another Radware program Addmat was used to add the two matrices together. Then the Slice program projected the symmetric  $E_\gamma - E_\gamma$  matrix into its x and y projection spectra. Xmgf3 program is another Radware program designed to perform manipulations on the spectra. It was used to create the background spectra needed for the XMesc program and also for peak fitting needed to correct for gain drifts. The Xmesec program was used to analyse  $E_\gamma - E_\gamma$  matrices. This program allows to gate on specific peaks and produces background subtracted gated spectra, which were needed in the  $E_\gamma - E_\gamma$  coincidence analyses. It was also used to draw the newly obtained level scheme.

### 3.4 Energy and time-gain matching, Doppler correction and gain drifts

#### 3.4.1 Energy gain matching and calibration

Each of the nine clover detectors has four elements, making 36 elements in total. Each element collects data independently so that each element has to be gain matched. The difference in the gains of each element could be quite large. Gain matching was done to calibrate all clover crystals to the same energy relationship of  $N = 2E_\gamma$ , where N is the channel number and  $E_\gamma$  is the gamma-ray energy. This was done at the beginning of each weekend.

Europium source was used to do such matching.  $^{152}\text{Eu}$  emits gamma-rays in the energy range (45-1408) keV. Europium source was chosen to do the gain matching because it was expected that the residual thallium nuclei would decay within a similar energy range as  $^{152}\text{Eu}$ . A quadratic relationship was obtained

$$kE = ax^2 + bx + c = N \quad (3.1),$$

for each element of the clover detectors. In this equation a, b, and c are the gain matching coefficients, x is the channel number in the original (non-gain matched) spectrum of the  $^{152}\text{Eu}$  peak with energy E, N is the channel number of this peak in the gain matched spectrum. The

coefficient  $k$  was chosen here as  $k=2$ , which means that the gain matched spectra have a gain of 0.5 keV/channel.

To perform this gain matching a few programs were run. The  $^{152}\text{Eu}$  source was placed in front of the detectors and data for about 30 minutes were collected. Then the energy histograms were saved. The saved histograms (clover# \*.Ge\* files) were then converted to ascii format (.dat files). A fitting program identified the europium peaks using as input two channel numbers which defined a range in which the peaks 344 keV and 778 keV (see Fig. 3-3). This was done for each crystal of each clover detector. The fitted centroid, area, chi squared etc for as many of the  $^{152}\text{Eu}$  peaks as possible, were obtained and saved (see Fig. 3-4). Once this was done, the centroid and energy values were used to run a calibration program (see Fig. 3-5) for each crystal element (see Fig. 3-6), which produced an initial set of gain matching coefficients.

```

$ R/nodebug S_FIT
IN CLOVER-SPECTRA.DAT
OU CLOVERS

PFND 6,4
TAIL n
STEP y

UNIVERSITY of the
WESTERN CAPE

VSTAT N
RAS 152EU

PFIL EU1521.PKS

PLIM 800,2100
FIT 1,1

PLIM 1200,3200
FIT 2,2
.
.
.
PLIM 2200,6000
FIT 37,37

PLIM 2000,5000
FIT 36,36

END

$ set noverify
$ EXIT
```

Fig 3-3 An example of the fitting command file run by the s\_fit program. PLIM being the range in which the program looks for the 344keV and 778keV peaks to fit.



The next step was to perform a Doppler shift correction because this experiment was performed using a thin target. Since the gamma rays were emitted while the residual nuclei recoiled in vacuum, shifts in the peak energies were observed, which were different for detectors placed at different angles. To correct for these shifts in energies, the recoil velocity needs to be calculated. The reaction  $a + X \rightarrow Y^*$  can be considered a linear inelastic reaction. Conservation of momentum requires equality of initial and final momentum

$$p_i = p_f \quad (3.2)$$

Thus

$$m_a v_a + m_X v_X = m_{Y^*} v_{Y^*} \quad (3.3).$$

But since the target is stationary,  $v_X = 0$ . For non-relativistic energies

$$v_a = \sqrt{\frac{2E_k}{m_a}} = \sqrt{\frac{2 \cdot 167 \text{ MeV}}{37 \cdot 931 \frac{\text{MeV}}{c^2}}} = 0.098 c,$$

where  $E_k$  is the beam energy,  $m_a = 37u$ ,  $m_X = 160 u$ ,  $m_{Y^*} = 197 u$  and the mass unit  $u = 931 \text{ MeV}/c^2$ . Inserting these in (3.3) and solving for recoil velocity of the compound nucleus gives

$$\beta = \frac{v_{Y^*}}{c} = \frac{37u \cdot 0.098}{197 u} = 0.018 \quad (3.4).$$

The Doppler correction program used this recoil velocity of 1.8% and the detector angles to correct the gain matched energies for Doppler shifts. The new gain matched coefficients (see Fig. 3-7), were put into the sort code and used in the online sorting. This experiment was done during two separate weekends. This meant that energy and Doppler corrections had to be done for both weekends. These gain matching coefficients produced data in which all detectors were gain matched to  $N = 2E_\gamma$ .

Clov.NR	GAINARRAY clovergains		
	a0	a1	a2
1	( 3.98370E+00	7.92582E-01	-2.26008E-07 )
2	( 2.72553E+00	5.13389E-01	-1.78710E-07 )
3	( -1.00198E+01	7.55278E-01	-2.08489E-07 )
4	( 8.42759E-01	5.01651E-01	-1.58173E-07 )

Fig 3-7 After Doppler correction the final gain matching coefficients were obtained. This figure shows these calibrated coefficients for the four elements of clover one.

### 3.4.4 Time gain matching and calibration

Time spectra needed to be gain matched too. One can use the gain matched time for selecting gamma rays detected within specific time window. Such time gated matrices were not analysed in this work but can be considered in the future using the gain matched times done here. An example of a time spectrum is given below in Fig. 3-8.

Each of the 36 time spectra had its gain adjusted to 1ns per channel. The prompt time peak was then shifted to an arbitrarily chosen position (channel 2000 in this work). This was accomplished with the aid of the equation,  $T = a_0 + a_1 t$ , where the gain matching coefficients are  $a_0$  and  $a_1$ . Here  $t$  and  $T$  are the channel numbers in the original and gain matched spectra. The  $a_1$  coefficient was calculated using the number of channels  $\Delta t$  between 20 small peaks to the right of the prompt peak and the requirement that in the gain matched spectra this number,  $\Delta T$ , should be equal to 19 times the time between two beam pulses (which is this expression 60 ns), i.e.  $\Delta T = a_1 \cdot \Delta t = 19$  therefor  $t_{bp} = 19 \cdot 60 \text{ ns} = 1140 \text{ ns}$ . Knowing  $a_1$  and setting  $T_0 = 2000$  for the gain matched centroid of the tallest peak and measuring  $t_0$  for the centroid of this peak in the original spectrum is sufficient to calculate  $a_0$ . These coefficients were used in the code for subsequent sorting (see Fig 3-9).

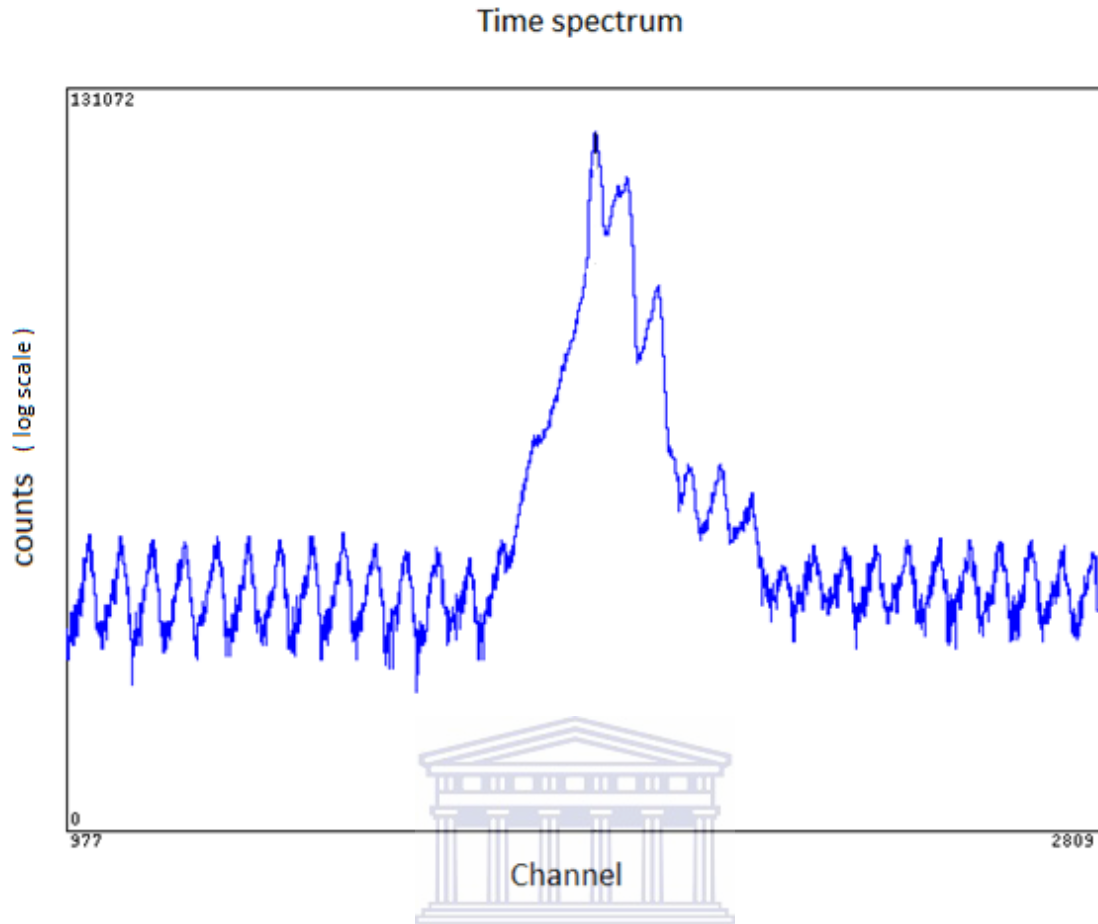


Fig 3-8 An arbitrary time spectrum, shown in a semi-logarithmic scale

GAINARRAY tdcgains			
1	(249.0	1.029678982	0.0)
2	(544.0	1.0	0.0)
3	(241.0	1.015531661	0.0)

Fig 3-9 An example of time gain matching coefficients for the first three spectra.

### 3.4.3 Gain drift of the energies

Temperature fluctuations during the experiment often alter slightly the gains of the clover elements. These shifts are small in comparison to the original differences in gains. Typical gain drifts for low energy peaks are less than 1 keV and about up to 2 keV-3 keV for high energy peaks. To correct this gain drifts two reference peaks were needed. The quadratic gain matching relationship

$$N = 2E = a_2x^2 + a_1x + a_0 \quad (3.5)$$



can be reduced to a linear one since  $a_2$  was found to be very small for all detectors

$$N = a_1x + a_o \quad (3.6).$$

Each of the 36 spectra has a unique energy equation (3.6) and for each of the 36 spectra there were 44 runs, for which the originally found gain matching coefficients  $a_1$  and  $a_o$  may need adjustment. The new coefficients  $a'_1$  and  $a'_o$  are thus to be calculated for each element and for each run, and this will ensure perfect gain matching for all detectors and all runs. A relationship was thus needed between shifted (P+S) reference peak (P) centroids the channel number  $x$  in the original (non-gain matched spectrum) and the old and new gain matched coefficients. In order to do this one has to choose two reference peaks, one at high energy and the other at low energy. Then to measure the shift in channel number of these two peaks in all spectra. The shift could be positive or negative (see Fig. 3-10).

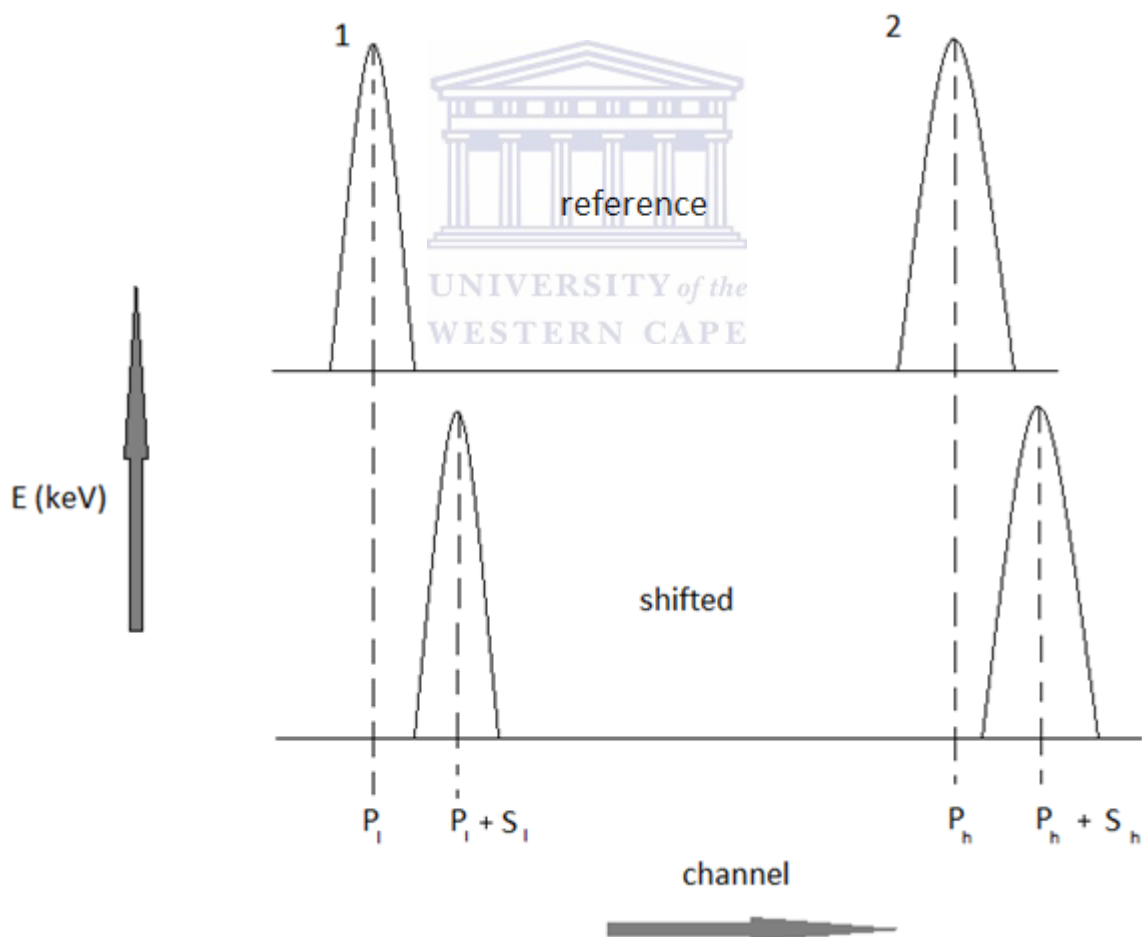


Fig 3-10 Shifted and reference peaks at low and high energies. The bottom spectrum show gain drift with shifts of  $S_l$  and  $S_h$  for the low and high energy centroids.

The positions of the reference and shifted peaks are,

$$P_l = a'_1 x + a'_o \quad (3.7)$$

$$P_l + S_L = a_1 x + a_o \quad (3.8)$$

$$P_h = a'_1 y + a'_o \quad (3.9)$$

$$P_h + S_h = a_1 y + a_o \quad (3.10)$$

These are four equations with four unknowns  $a'_1, a'_o, x$  and  $y$ . Inserting (3.10) into (3.9) and (3.8) into (3.7) gives

$$P_h = a'_1 \left( \frac{P_h + S_h - a_o}{a_1} \right) + a'_o \quad (3.11)$$

$$P_l = a'_1 \left( \frac{P_l + S_l - a_o}{a_1} \right) + a'_o \quad (3.12).$$

Solving (3.11) and (3.12) for  $a'_1$  and  $a'_o$  gives

$$a'_1 = \frac{a_1(P_h - P_l)}{(P_h - P_l) + (S_h - S_l)}$$

$$a'_o = \frac{(P_l S_h - P_h S_l)}{(P_h - P_l) + (S_h - S_l)} + a_o \frac{(P_h - P_l)}{(P_h - P_l) + (S_h - S_l)} \quad (3.13).$$

Knowing the new gain and offset for each spectrum and for all of the runs produced better gain matching throughout all data sets.

In order to determine the shifts of the peaks of interest for each detector for and each run the Radware program Xmgf3 was used. First a manual fit was done for one of the peaks at high and low energy to get its position, area and energy etc. (see Figs. 3-11 and 3-12).

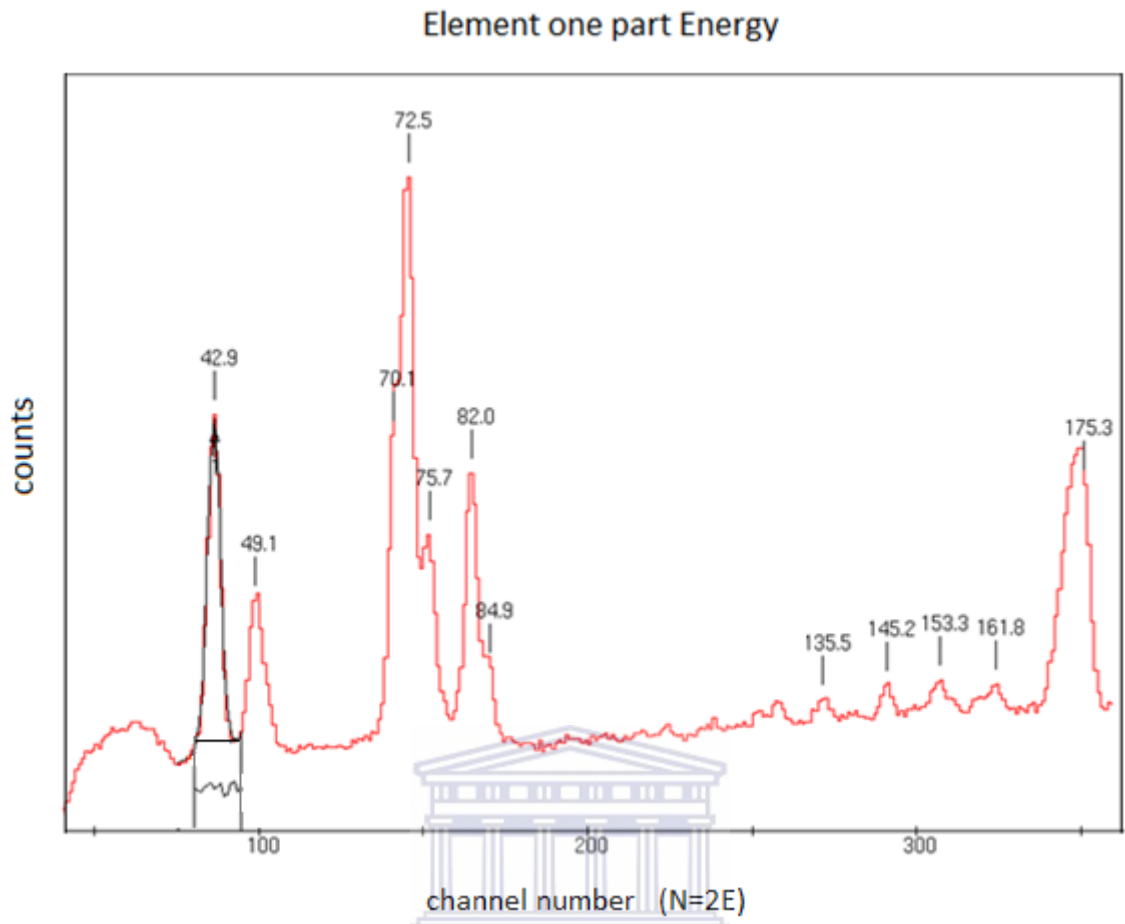


Fig 3-11 fit of the peak 42.9 keV

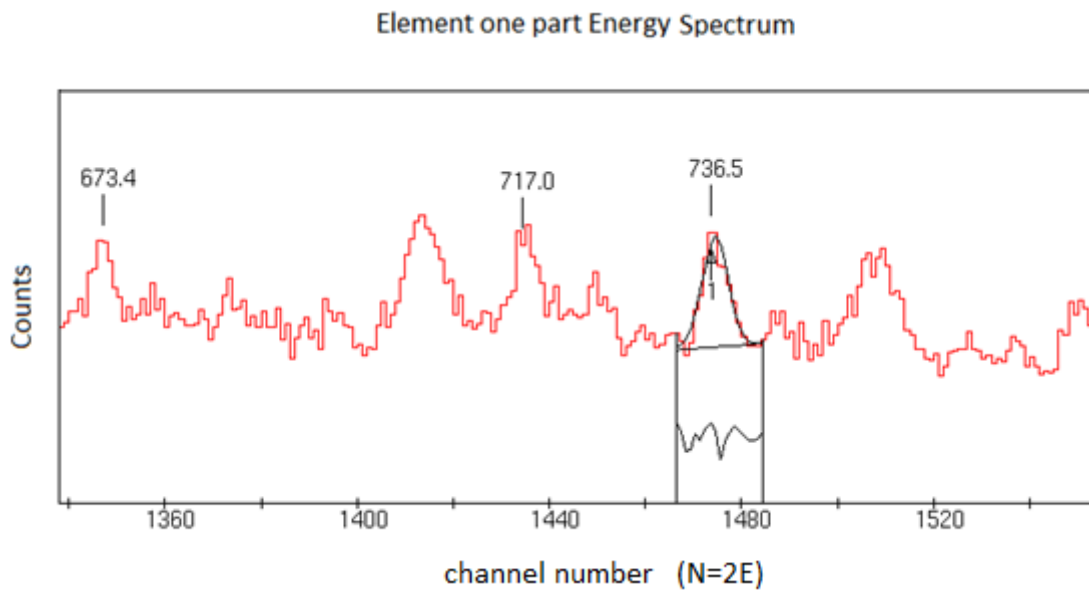


Fig 3-12 fit of the peak 735.6 keV

Then a fitting code was utilised that automatically fits and saves the centroids of these peaks in all spectra from that particular run in the storage file (see Fig.3-13).

<pre> nx 300 x0 0 col  sp cloverenergy.0.spe ds ft-1 y  sa10 sa-1 cfchk  sp cloverenergy.1.spe ds ft-1 y  sa1 sa-1 cfchk </pre>						
No.	Centroid + error	Area + error	Energy + error	Sp.name	Date	Time
0	85.6863 0.0193	20592	203 42.8432 0.0096	cloveren	22-Jun-1116:19:10	
1	85.6068 0.0194	15309	172 42.8034 0.0097	cloveren	22-Jun-1116:19:11	
2	85.6630 0.0165	19330	185 42.8315 0.0083	cloveren	22-Jun-1116:19:12	
3	85.6224 0.0152	17662	173 42.8112 0.0076	cloveren	22-Jun-1116:19:12	

Fig 3-13 The top is a portion of fitting code used, while the bottom is a portion of the storage file.

The storage files, one low energy peak and one high energy peak, for each run were fed into a program called Physica, which arranged the centroids for each element of every run into a file and produced figures illustrating the gain drifts for each detector (see Fig. 3-14).

```

device\colour postscript
clear
defaults
orientation landscape
destroy *v

generate R 1 1 32

read R3_737.sto\[2:37] e2[1,1:36]\6
read\append R4_737.sto\[2:37] e2[2,1:36]\6
read\append R5_737.sto\[2:37] e2[3,1:36]\6

read R3_40.sto\[2:37] e1[1,1:36]\6
read\append R4_40.sto\[2:37] e1[2,1:36]\6
read\append R5_40.sto\[2:37] e1[3,1:36]\6

RR=[3.0;4;5;6;7;8;9;10;11;12;13;14;15;16;17;18;19;20;21;23;24;25;27;28;29;30;31;32;33;34;35;36
]

write\format shifts2.dat (F4.1,8(F10.4)) RR e1[*],1] e2[*],1] e1[*],2] e2[*],2] e1[*],3] e2[*],3]
e1[*],4] e2[*],4]
write\append\format shifts2.dat (F4.1,8(F10.4)) RR e1[*],5] e2[*],5] e1[*],6] e2[*],6] e1[*],7]
e2[*],7] e1[*],8] e2[*],8]

scales 0 25 5 38 44.5 5
label\x `run number'
label\y `Energy (keV)'

setcolor 1
graph\axesonly
legend frame 80 15 95 40
legend on
setpchar 12
setcolor 2
graph\noaxes `c11' R e2[1:32,1]
setpchar 1
setcolor 3
graph\noaxes `c12' R e2[1:32,2]
setpchar 10
setcolor 4
graph\noaxes `c13' R e2[1:32,3]
setpchar 4
setcolor 1
graph\noaxes `c14' R e2[1:32,4]
replot
hardcopy s c1-737.ps

```



```
VALUEARRAY shifts [0:8, 1:31, 0:8]
```

2.0	42.8170	736.9659	42.8050	736.0169	42.8003	736.4330	42.8141	736.7668
3.0	42.8054	736.8480	42.7875	736.6832	42.8214	736.4561	42.7979	736.7247

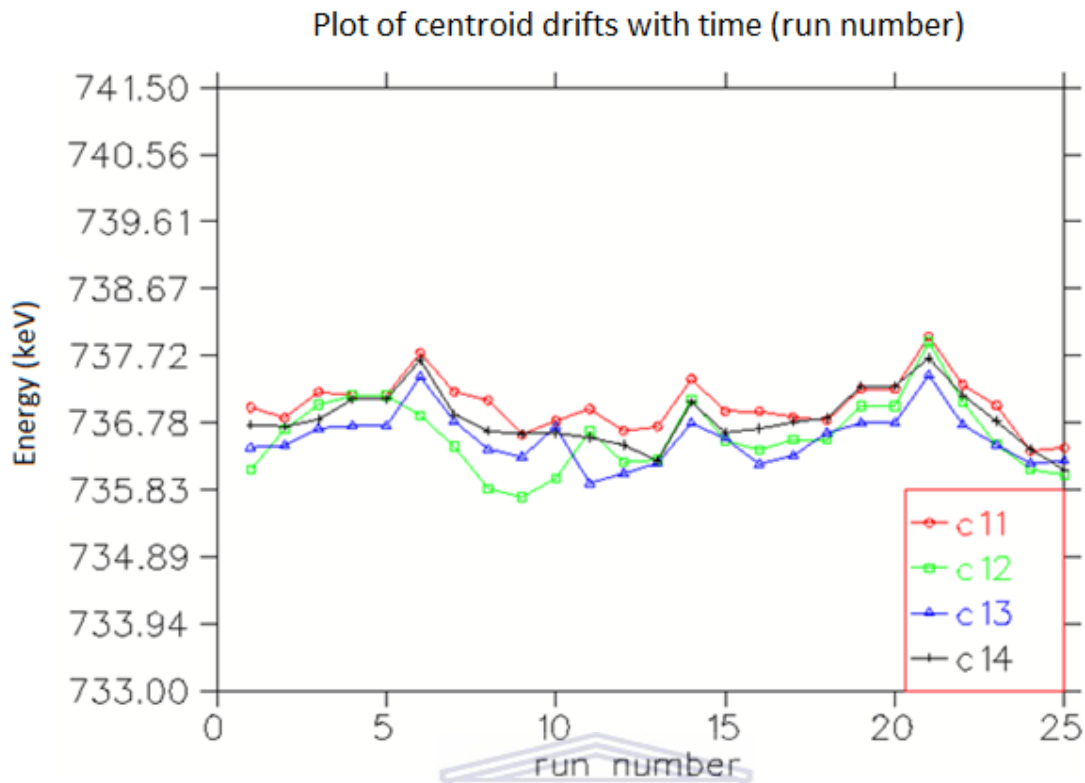


Fig 3-14 The top panel is the command file used by Physica to read the storage files and to produce the output files with all centroids (a portion of which is shown in the middle panel) and figures illustrating the gain drifts for each clover element throughout the weekend (such an example for clover one is shown in the bottom panel).

With the aid of these shifts file the sorting code calculated the new gain matching coefficients  $a'_1$ ,  $a'_0$  for all clover elements and for each run (a set of 44\*36 gain matching coefficients) Using these gain matching coefficients the data for the two weekends were sorted into several matrices and spectra.

### 3.4.4 Gamma coincidence analysis

Gating is a way of identifying when a gamma ray is in coincidence with other gamma rays. When a gate is set on a certain photo peak in the total projection spectrum, only gamma rays that are in coincidence with this photo peak are shown. Gating in succession on the peaks of interest allows us to build level schemes such as the example shown in Fig. 3-15.

A gamma ray is in coincidence with another gamma ray when they both belong to the same decay path. When a fusion evaporation reaction happens residual nuclei are formed with high excitation energy and angular momentum and decay to their ground states. The residual nuclei are produced with a statistical distribution within certain excitation energy range. This means that the starting point for the decay path is not always the same. But each excited level has a decay path to the ground state. Different decay paths may have a common part. Gamma rays that do not belong to the same decay path are said to be in anti-coincidence.

As an example consider Fig. 3-15.

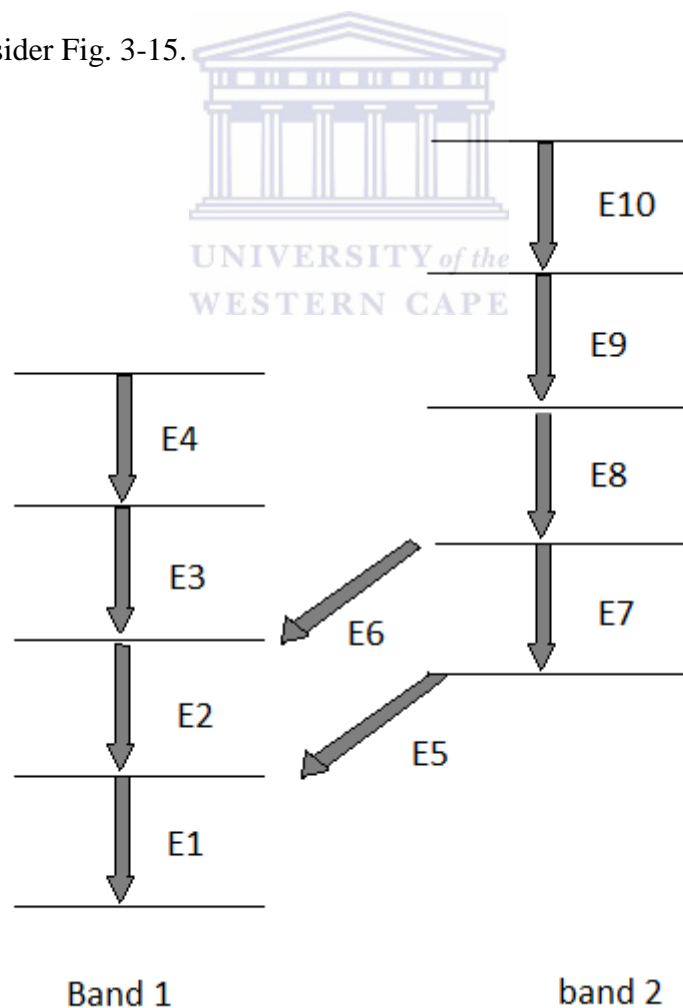


Fig 3-15 An example of a level scheme (E=gamma energy)

Band1 consists of E1, E2, E3 and E4 gamma rays all of them in coincidence with each other, whereas E5, E6, E7, E8, E9 and E10 are in anti-coincidence with E4 and E3 transitions. E2 on the other hand is in anti-coincidence with E5 and E7 but in coincidence with all the rest of the gamma rays in the level scheme. In band2, E10 for example is in anti-coincidence with E4 and E3 but in coincident with all the rest of the gamma rays in the level scheme.

## 4 **Chapter 4 Data analysis, results and discussion**

### 4.1 **Contaminants**

Contamination in the data may come in many forms. Contaminants can originate from external sources, e.g. contamination in the target (oxidation or targets that are not 100% enriched with one specific isotope), neutron peaks, an annihilation peak, X-rays, Coulomb excitation of the target and random coincidences. The data itself may present additional complications for the analysis, since it may contain gamma rays that belong to other residual nuclei. There might be doublets, i.e. two or more gamma rays with similar energies which belong to one or more residual nuclei, etc.

#### 4.1.1 **External sources of contaminants**

This experiment used a thin gadolinium target. If one uses targets that are sensitive to oxidation, it is advisable when removing the target from the target chamber to vent with an inert gas. Usually these gasses are nitrogen or argon. After the first weekend when the target was removed from the target chamber we did not vent with an inert gas, since gadolinium is not sensitive to oxidation in dry air. However the data from the second weekend showed that the target did oxidise. Later analysis showed that the oxidation was only around the spot where the beam hit. The lack of oxidation on the whole surface of the target shows that this effect is related to irradiation with the chlorine beam. Such increased oxidation may have been caused by radiation damage.

The fusion evaporation reaction of the oxygen in the target with the  $^{37}\text{Cl}$  beam produced a few residual nuclei during the second weekend. PACE4 calculations showed  $^{49}\text{Cr}$ ,  $^{49}\text{V}$ ,  $^{47}\text{Ti}$



and  $^{46}\text{Ti}$  as the most probable fusion products with the largest cross-sections of 211 mb for  $^{49}\text{Cr}$ . Furthermore these fusion products have very high recoil velocities,  $\beta \sim 8.7\%$ , which causes their gamma rays to show large Doppler shifts. Such peaks particularly at high energy appear as broad bumps in the spectra. The first weekend data does not show these contaminations but they are relatively strong in the second weekend data. These gamma rays include 159 keV from  $^{47}\text{Ti}$  and several high energy peaks,  $E > 800$  keV from  $^{46}\text{Ti}$  and  $^{47}\text{Ti}$ . In most cases gating on the peaks of  $^{192}\text{Tl}$  cleaned the gated spectra from this contamination, although the presence of these contaminants seemed to worsen the background subtraction in the data from the second weekend. These contamination peaks can be seen in the total projection of the  $E_\gamma - E_\gamma$  matrix sorted from the data of weekend two, while they do not show in the weekend one data (see Fig. 4-0). When constructing the level scheme two matrices were extensively used, the matrix that contained both weekend data (more statistics but more contamination) and the other matrix that contained data from the first weekend only (less statistics but cleaner spectra).



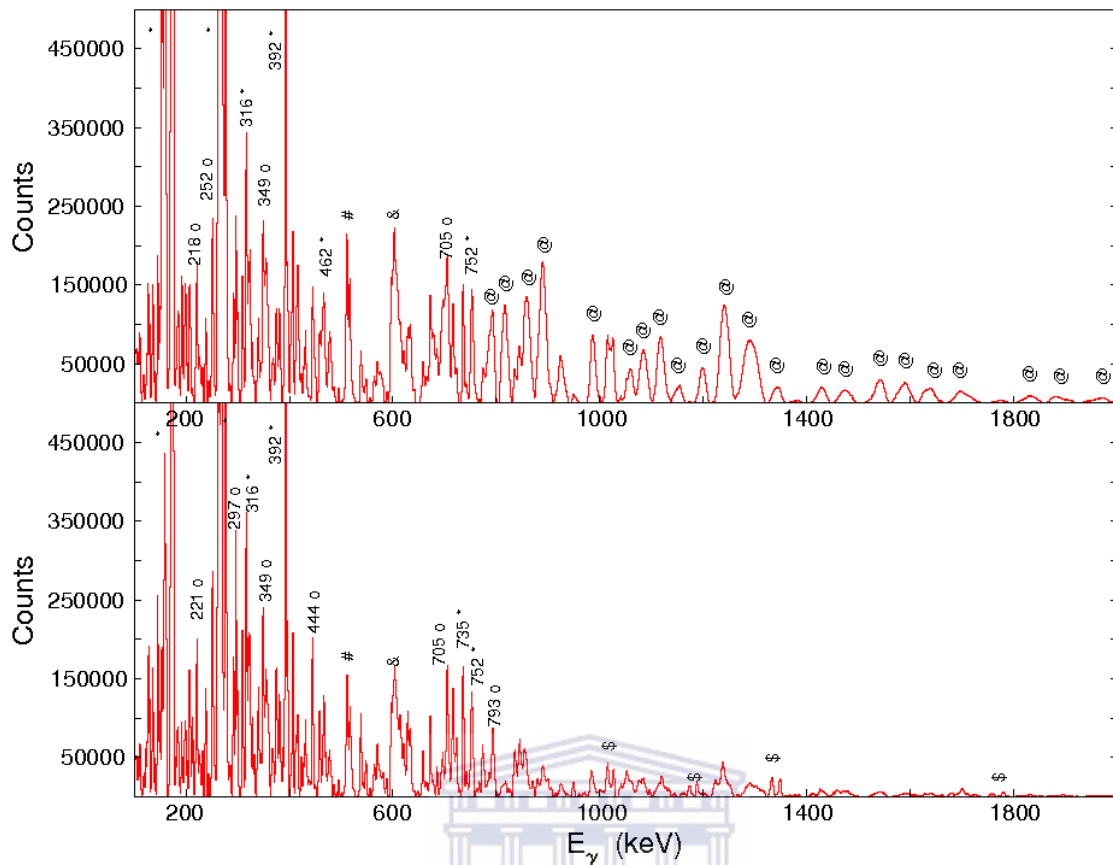


Fig 4-0 Show the total projection of the individual matrices for weekend one (bottom) and weekend two (top). In the figure the contamination appears in the second weekend, with the peaks: \*=Coulomb excitation, #=511keV, &= neutron damage, \$=aluminium excitation and @= contamination due to oxygen. Peaks labelled as, for example 750 o, are peaks in <sup>192</sup>Tl and peaks labelled as, 752 \*, are <sup>193</sup>Tl transitions.

Neutron damage happens when evaporated neutrons interact with the clover detector crystals. This reaction excites germanium isotopes to the first few excited states. When they de-excite they emit characteristic gamma rays. This is the cause of the observation of the so called neutron peaks in the data. Strong neutron peaks that were observed were 596 keV (from <sup>74</sup>Ge) and 834 keV (from <sup>72</sup>Ge). Neutron peaks exist for other germanium isotopes too but occur for E > 800 keV.

The annihilation peak as discussed above was observed at 511 keV. It appears as two peaks in our data due to the Doppler correction applied. Since these gamma rays are emitted from a stationary source they do not need Doppler correction. The Doppler correction applied shifted the peak detected at 135° from 511 keV to 517 keV.

X-rays come from internal conversion in the residual nuclei and target. They are thus characteristic of thallium and gadolinium element and their specific isotopes. They are found in the lower part of the spectrum, typically 40 keV-85 keV. The thallium X-rays can be found in the range 71-73 keV and 83 keV and gadolinium X-rays are found at approximately at 43 keV and 49 keV.

Peaks that originated from Coulomb excitation of the gadolinium target include 75 keV, 174 keV and 266 keV peaks. These peaks are reasonably strong in the data.

During the experiment there was a problem with the read out of the detectors resulting in dropping bits in the spectra of the affected detectors. This problem occurs when the data cables do not make good contact with the electronic modules. The problem was fixed quickly but approximately four hours of good data in one clover detector had to be excluded from the data analysis.

#### 4.1.2 Internal sources of contaminants

A few isotopes of thallium were produced in this experiment, with the dominant isotope being  $^{192}\text{Tl}$ . Isotopes of thallium produced in this reaction are present in the data with percentages proportional to the excitation functions cross-section (see Fig. 2-2).

When gating on known peaks in  $^{192}\text{Tl}$ , peaks from  $^{193}\text{Tl}$  and  $^{194}\text{Tl}$  were sometimes observed too. This happens when transitions with similar energies to the gate in  $^{192}\text{Tl}$  belong to other thallium isotopes. The 392 keV peak which is a doublet in  $^{193}\text{Tl}$  shows strongly in all gated spectra that bring  $^{193}\text{Tl}$  transitions.  $^{194}\text{Tl}$  has many gamma rays with identical energies to transitions in  $^{192}\text{Tl}$  a few of them are 396 keV, 300 keV, 376 keV, 458 keV and 628 keV. Its strongest gamma ray has energy of 278 keV. Checking the gated spectra for the presence of these transitions can indicate whether contamination from neighbouring  $^{193}\text{Tl}$  or  $^{194}\text{Tl}$  may be present.

To combat the difficulties that the presence of such gamma rays presents it was necessary not only to examine the coincidence relationship, but also to investigate the intensity of the observed gamma rays. For example assume that one wanted to check whether an observed gamma ray with energy of 377 keV was in coincidence with a particular gamma ray in  $^{192}\text{Tl}$  (on which we gate and which may have a doublet in another thallium isotope) or whether it is a contamination (for instance from  $^{194}\text{Tl}$ ). In this case one can inspect the intensities of the

gamma rays that are known to be in the same decay paths with 377 keV transition in both isotopes. If the 377 keV peak under investigation had relative intensity consistent with the intensities of the gamma rays in the 377 keV decay path in  $^{192}\text{Tl}$ , while the gamma rays in coincidence with 377 keV in  $^{194}\text{Tl}$  did not show, one could conclude that the 377 keV gamma ray belonged to  $^{192}\text{Tl}$  and was in coincidence with the gamma ray used as the gate.

Doublets, i.e. gamma rays with similar energy, were frequently encountered when building the level scheme. They are quite difficult to place in the level scheme in particular if they are in coincidence with each other, because spectra gated on such doublets show gamma rays that are in coincidence with both members of the doublet. Some doublets of this nature encountered in this work included 252 keV, 297 keV and 328 keV transitions.

A similar problem is encountered with gamma rays that have energies differing by  $\approx 1$  keV because their peaks overlap. Consider the peaks 657 keV and 658 keV. When gating on 657 keV the gate includes part of the 658 keV peak. The gamma rays that are in coincidence with 658 keV will show in this gated spectrum too. Similarly when gating on the peak 658 keV gamma rays that are in coincidence with 657 keV will also be seen in the 658 keV gated spectrum. In this case though, the spectra are not identical.

## 4.2 **Results**

### 4.2.1 **Building the level scheme**

#### 4.2.1.1 **Confirmation of the known level scheme Band 1**

The starting point in building any level scheme is to start with the yrast band and the part of it that is already known. The yrast band is the most intense band. This means that most gamma ray decay paths pass through the yrast band bringing all their intensity through the yrast band to the ground state. In our case the implied state is an isomer which decays to Hg via electron capture and positive beta decay. The lowest lying level observed in this data is the  $8^-$  isomeric state with a lifetime of approximately 300 ns. In these data the most intense peaks in the total projection are generally the X-ray peaks and the Coulomb excitation peaks. These include the X-rays with energies 43 keV, 75 keV and 83 keV and the Coulomb excitation peaks at 175 keV and 266 keV. We excluded these and started investigating the next most intense peaks in the total projection, i.e. the 276 keV and 262 keV transitions, (see Fig. 4-1).

The 276 keV transitions was previously known and placed just above the  $8^-$  isomer and it was the starting point in building a level scheme.

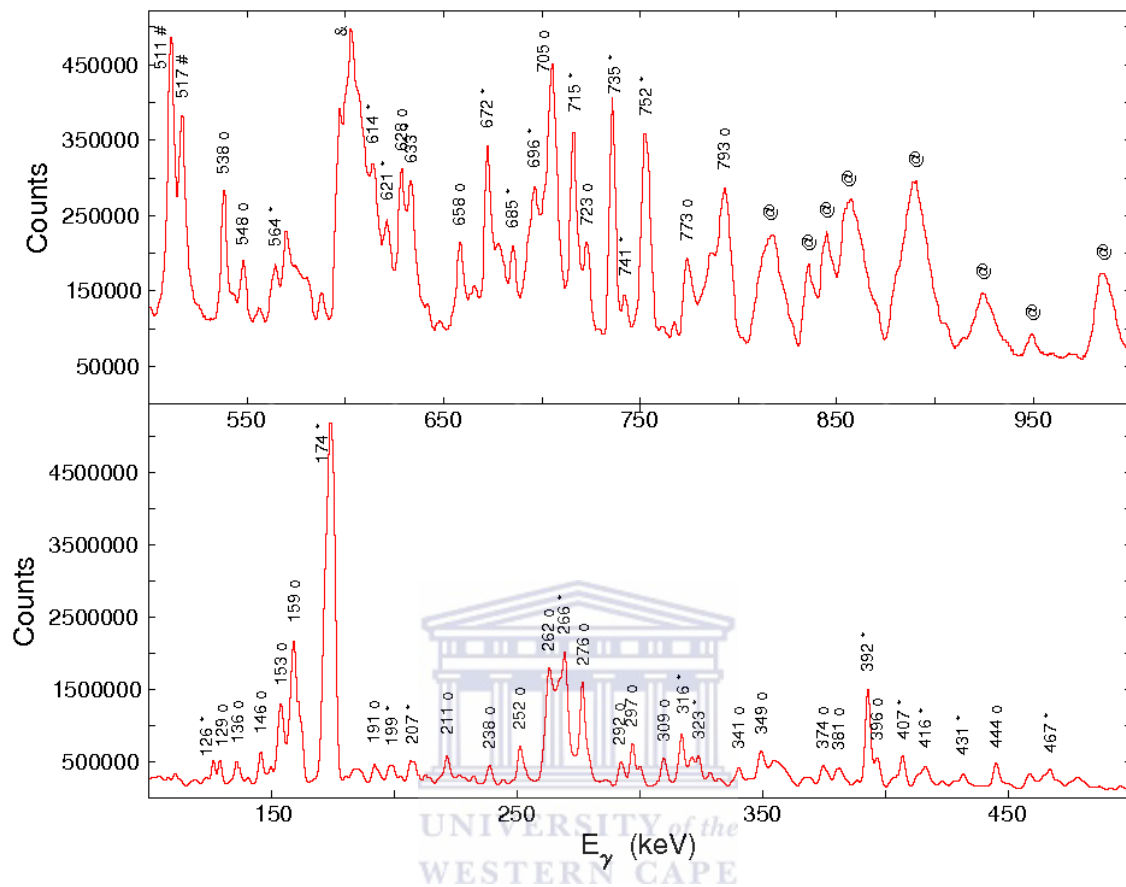


Fig 4-1 The total projection of both weekends with \* being other thallium isotopes and other contaminants, o are  $^{192}\text{Tl}$  gammas and @ are contamination due to oxygen.

In the previous level scheme [Kre79] (see Fig. 4-3), an 83 keV transition is placed just below the 276 keV gamma ray. But there is an inherent problem with 83 keV as a starting point. This gamma ray has an energy that is close the thallium X-ray 82.5 keV. It appears on the shoulder of the 82.5 keV X-ray and is very difficult to gate on. In this previous work it was suggested, based on the systematics of the odd-odd thallium isotopes that another low energy gamma ray (with energy  $\sim 20$  keV) probably lies below 83 keV transition. Such transition has not been experimentally observed in their work. Furthermore since the target is thin the  $^{192}\text{Tl}$  nuclei recoil outside of the target with velocity  $0.018 c$ , which is  $5.4 \text{ mm/ns}$ . By the time the 250.6 keV gamma ray (transition linking the  $8^-$  and the  $7^+$  isomers) is emitted the nuclei may have left the field of view of the gamma detectors (see Fig. 4-2).

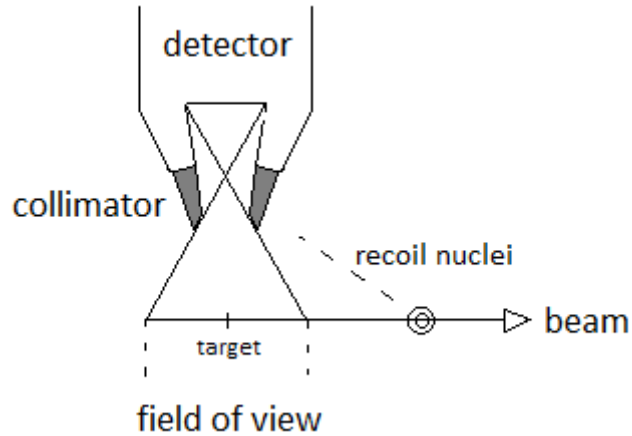


Fig 4-2 Field of view seen by the recoiling nuclei

Confirmation of the known level scheme was done by gating. A gate was set on 276 keV transition. In this gated spectrum the 262 keV peak was the most intense and thus its placement directly above the 276 keV transition is very likely. Gating on 262 keV peak in turn shows a strong 276 keV peak confirming that these two transitions are in coincidence. Additional confirmation of the placement of these transitions came from the establishment of the cross over 538 keV. Cross overs are gamma rays in rotational bands which carry away  $2\hbar$  units of angular momentum away (E2 transitions) and are placed in parallel to two dipole (M1) transitions. Then the sum of the energies of the two M1 transitions equals the energy of the E2 cross over transition. For example  $276 \text{ keV} + 262 \text{ keV} = 538 \text{ keV}$  which is a cross over transition. Thus as a first step the placement of the transitions in the known level scheme was confirmed.

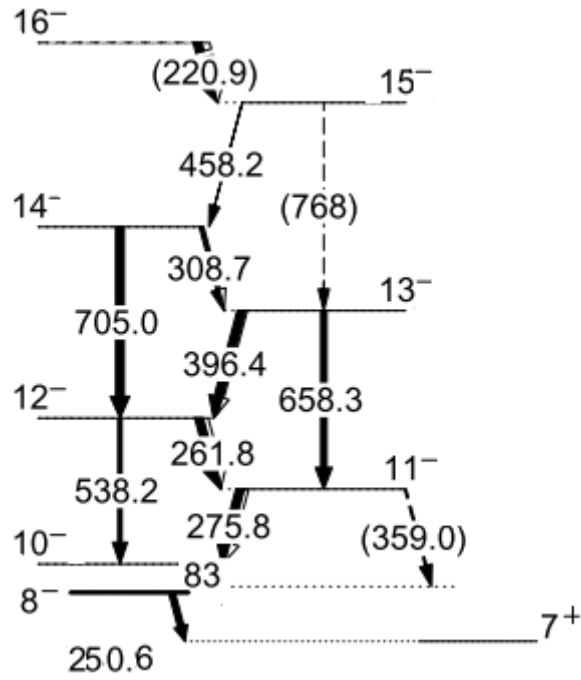


Fig 4-3 The known level scheme of  $^{192}\text{Tl}$  [Kre79]

#### 4.2.1.2 Extension of band 1

In the known level scheme the 458 keV gamma-ray was placed above the 309 keV transition. The logical next step was to gate on 458keV transition and to search for new transitions (see Fig. 4-4).

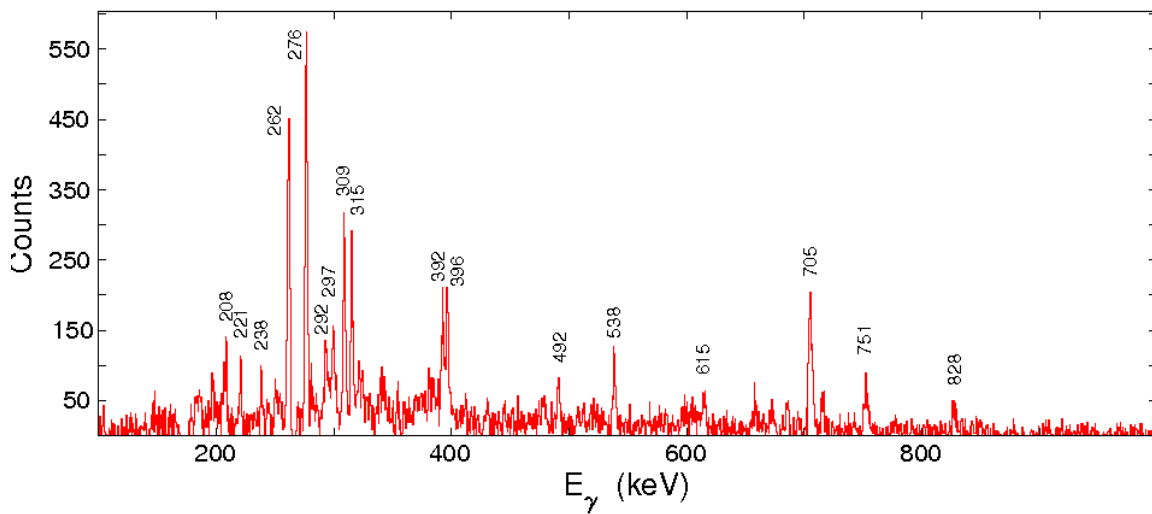


Fig 4-4 gate on 458 keV transition

When gating on 458 keV the 309 keV gamma ray (which is placed just below it in the known level scheme) is very strong (see Fig 4-4). All strong peaks in the spectrum gated on 458 keV transitions are accounted for (i.e. they are already placed in the level scheme) except the 315 keV and 492 keV peaks. When gating on 315 keV transition (see Fig 4-5) we see the 458 keV transition, meaning it is in coincidence with 315 keV gamma ray, interestingly there is at peak 316 keV. One can note that in  $^{193}\text{Tl}$  there is a doublet of 315-316 keV transitions. This means that when gating on the 315 keV transition it brings  $^{193}\text{Tl}$  gamma rays that are in coincidence with the peaks 315 keV and 316 keV because they are so close to each other. This conclusion is confirmed in Fig 4-5 by the presence of strong peaks of  $^{193}\text{Tl}$  such as the 392 keV and 735 keV transitions. On the other hand peaks of  $^{192}\text{Tl}$ , such as 276 keV, 262 keV, etc are very strong too, confirming that  $^{192}\text{Tl}$  also has a gamma-ray with 315 keV energy.

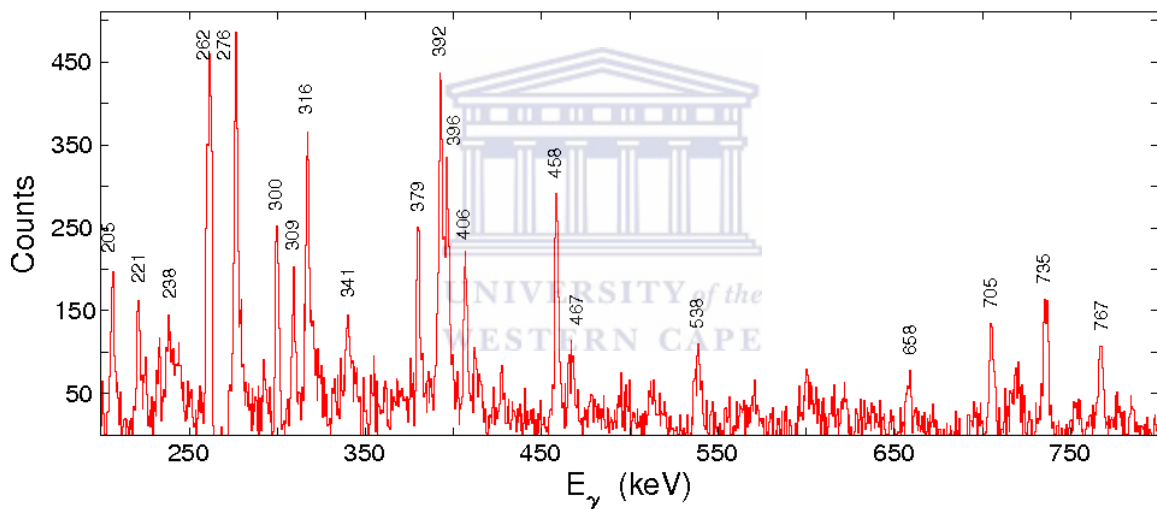


Fig 4-5 gate on 315 keV transition

The gate on 492 keV transition shows a few important things (see Fig. 4-6). The 458 keV gamma ray is in coincidence with 492 keV transition, while the 315 keV peak is not. Therefore this suggests that 492 keV transition should be placed in anti-coincidence with 315 keV gamma-ray. At this point it is not known how far above 458 keV transition the peaks 315 keV and 492 keV should be placed although one suspects that they should be placed close, since they were the strongest unidentified peaks in the spectrum gated on the 458 keV gamma ray. To confirm the placement of 315 keV and 492 keV peaks a cross-over transitions are needed.



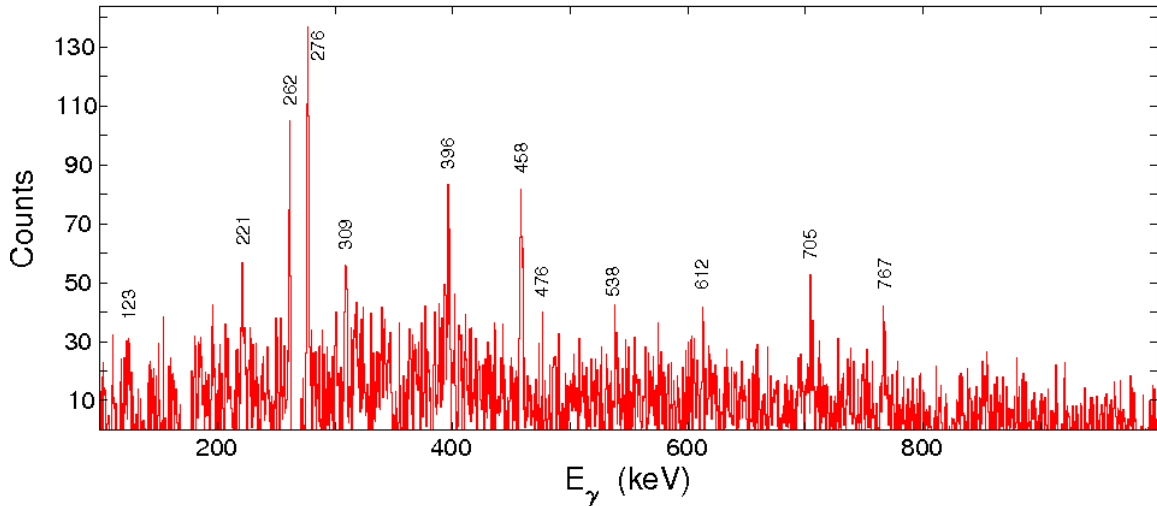


Fig 4-6 gate 492 keV transition

Gating on the gamma ray below 458 keV transition, i.e. 309 keV peak, one notices another interesting feature that the spectra gated on 315 keV, 458 keV and 492 keV transitions do not have (see Fig. 4-7). These are the peaks at 773 keV and 950 keV. This shows that the 773 keV and 950 keV transitions are in coincidence with 309 keV peak but in anti-coincidence with 458 keV, 315 keV and 492 keV transitions. Furthermore the sums 315 keV+458 keV and 458 keV+492 keV are exactly equal to 773 keV and 950 keV respectively.

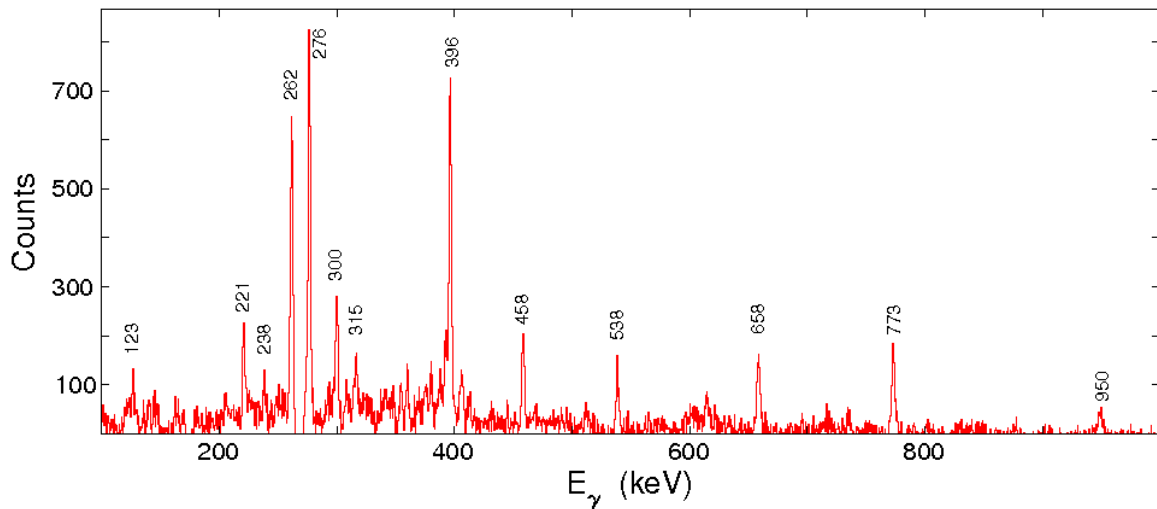


Fig 4-7 gate on 309 keV transition

This suggests that the 773 keV and 950 keV peaks can be cross-overs to the 315 keV and 458 keV peaks, and to 492 keV and 458 keV transitions respectively. This is further confirmed by gating on 773 keV and 950 keV transitions. The 773 keV gated spectrum

confirms that 773 keV transition is in anti-coincidence with 315 keV and 458 keV transitions (by their absence) and in coincidence with the other transitions in band1 (see Fig 4-8). Similarly gating on 950 keV transition confirms the anti-coincidence of 950 keV peak with the 492 keV and 458 keV peaks while 950 keV transition remains in coincidence with the other transitions of band1 (see Fig 4-8). Thus the placement in band 1 of these new transitions is established. It is shown in Fig. 4-14.

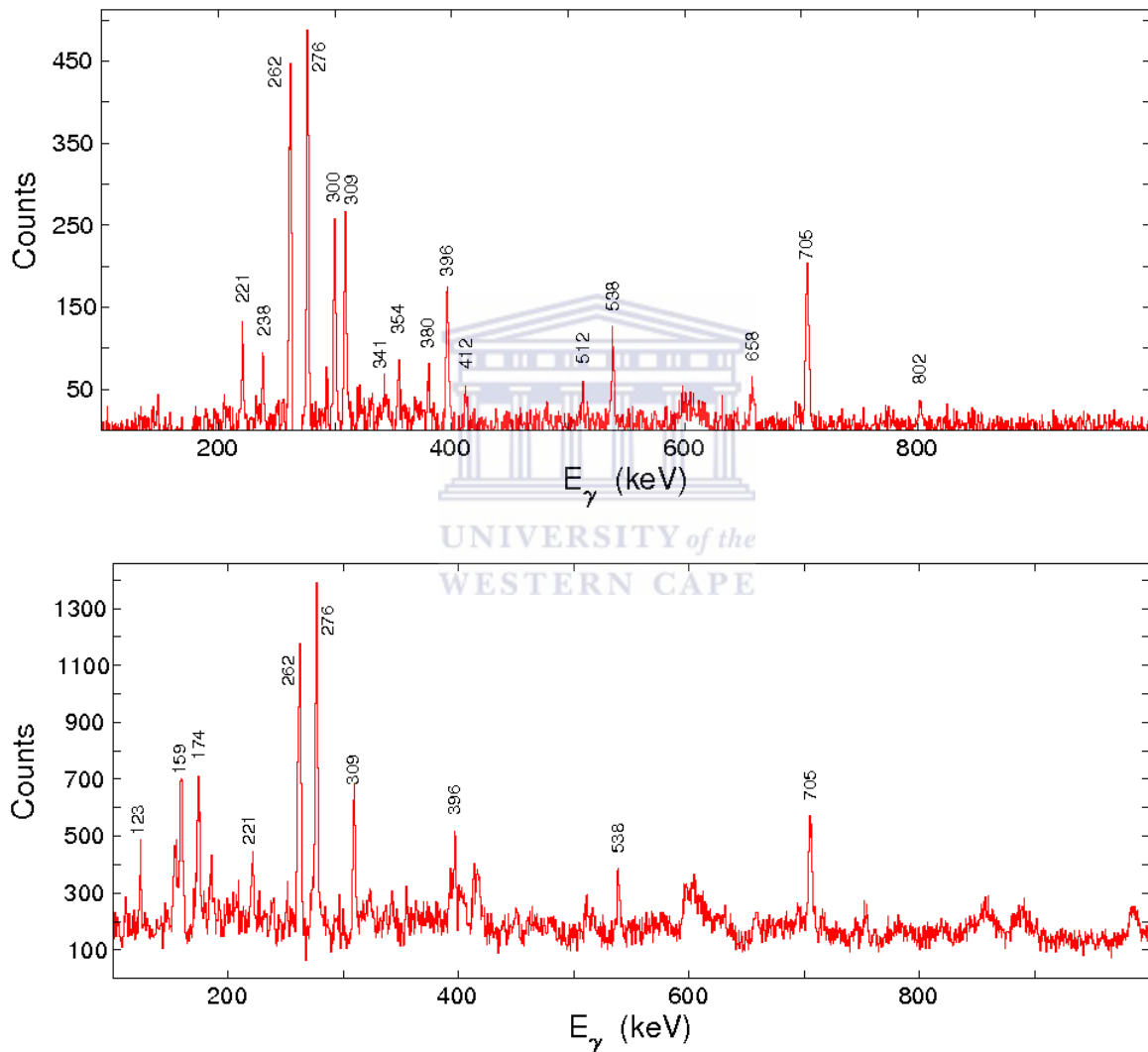


Fig 4-8 gates on 773 keV (top) and 950 keV (bottom) peaks

Gating on 315 keV transition (see Fig. 4-5), we see that 300 keV peak is equally strong as 458 keV peak suggesting that 300 keV peak may be placed directly above 315 keV transition. To confirm such a placement a cross-over transition is needed. The cross-over would be seen in the spectrum gated on 458 keV transition but would disappear in the spectra gated on

transitions 300 keV, or 773 keV, or 315 keV, or 492 keV, or 950 keV. The peak 615 keV is indeed observed in the spectrum gated on peak 458 keV (see Fig 4-3) while it is not seen in the spectra gated on peaks 300 keV, 773 keV, 315 keV, 492 keV and 950 keV. The cross-over is expected to have energy of  $315 \text{ keV} + 300 \text{ keV} = 615 \text{ keV}$ . The spectrum gated on 615 keV peak, Fig. 4-9 further confirms the placement of 615 keV as a cross-over of 315 keV and 300 keV transitions.

There could be a transition linking the levels at the excitation energy of 2669 MeV and 2546 MeV. If so its energy will be  $615 \text{ keV} - 492 \text{ keV} = 123 \text{ keV}$ . In Fig. 4-7 which shows a spectrum gated on 309 keV peak, a transition with energy 123 keV is observed. Furthermore the spectrum gated on 123 keV transition (see Fig. 4-10) shows a coincidence with the other transitions in band1, including 492 keV and 950 keV gamma rays, but not with 615 keV and 300 keV gamma rays. Thus the 123keV transition was placed above the 492 keV transition in anti-coincidence with the 615keV transition.

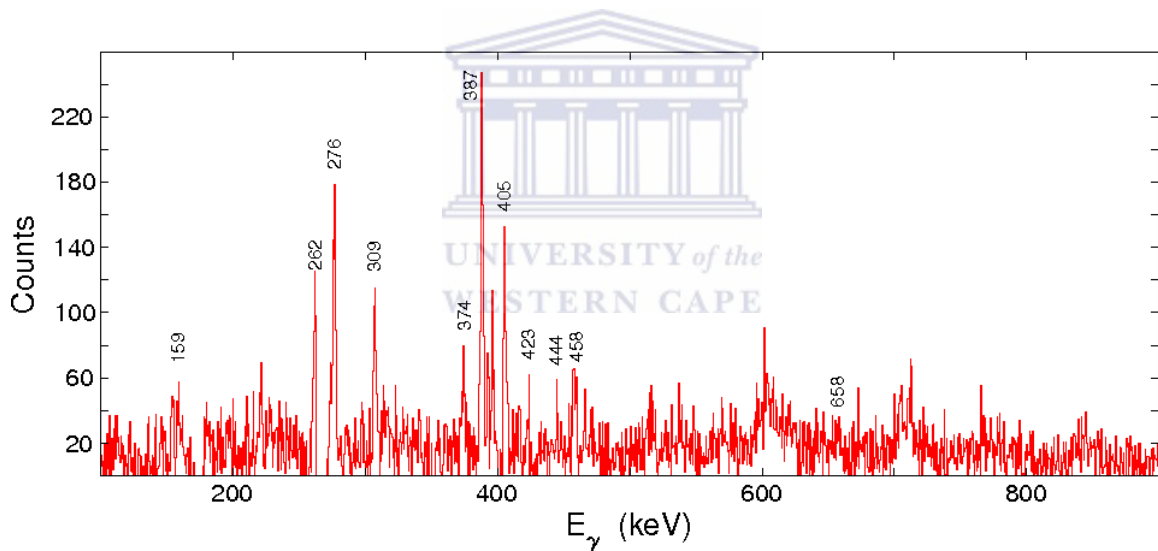


Fig 4-9 Gate on 615 keV transition

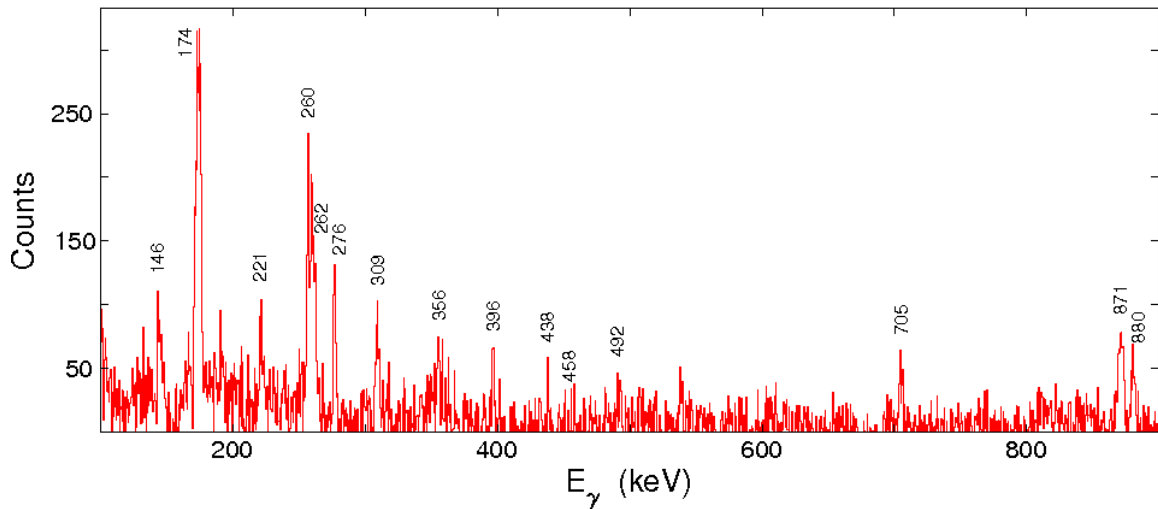


Fig 4-10 gate on 123 keV transition

In the spectrum gated on 300 keV (see Fig. 4-11) one notices a strong, still to be placed, peak, i.e. 221 keV. Furthermore a closer look at 262 keV (see Fig. 4-11) shows that the peak is very broad thus suggesting that another peak is located at a very close energy to 262 keV. In the gate on 221 keV spectrum (see Fig. 4-12), a very strong peak with energy closer to 260 keV is seen. Further gating proved that both of the transitions, 260 keV and 221 keV are in coincidence with the gamma rays of band 1 and with each other and should thus be placed above the 300 keV transition. Since no cross-over transition could be found at this time the ordering of these two transitions is not unambiguous.

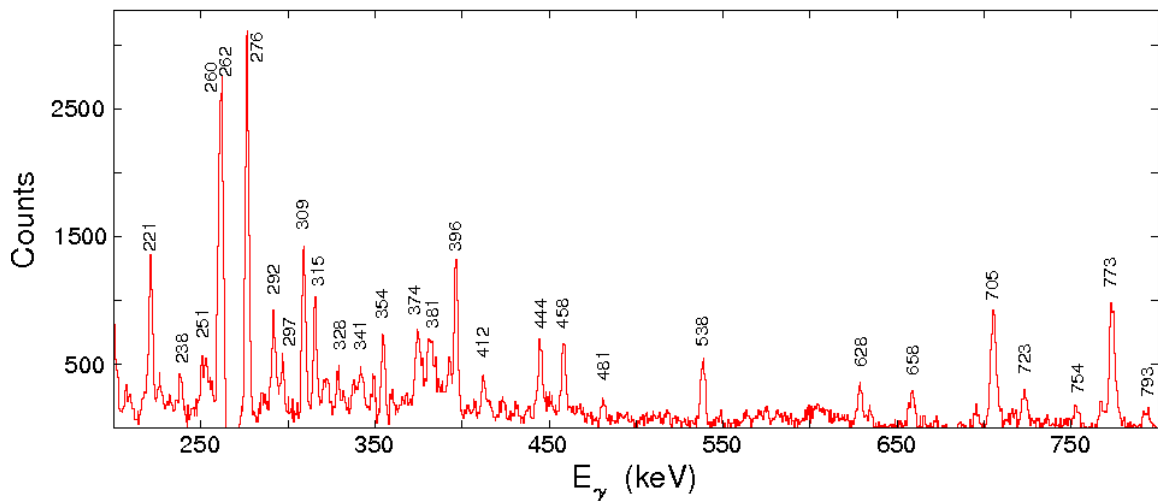


Fig 4-11 Gate on 300 keV transition

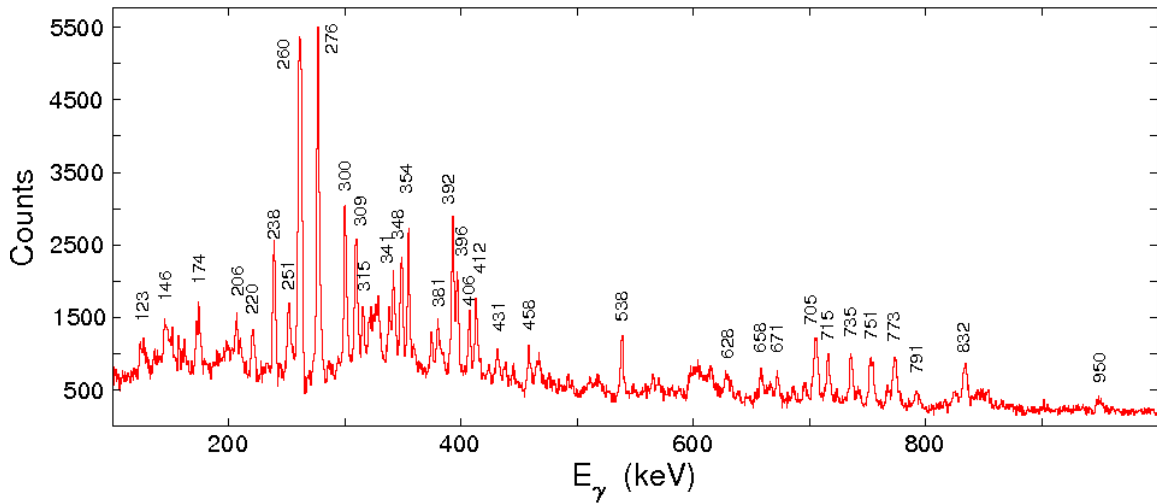


Fig 4-12 Gate on 221 keV transition

Similarly the transitions 354 keV, 341 keV and 412 keV were placed above the 221 keV gamma ray in the level scheme (see Fig. 4-14). Since no cross-overs were found, the ordering of these gamma rays could be different. Another transition, 238 keV is found in anti-coincidence with 354 keV, 341 keV and 412 keV peaks (see Fig. 4-13), which explains the placement shown in Fig. 4-14.

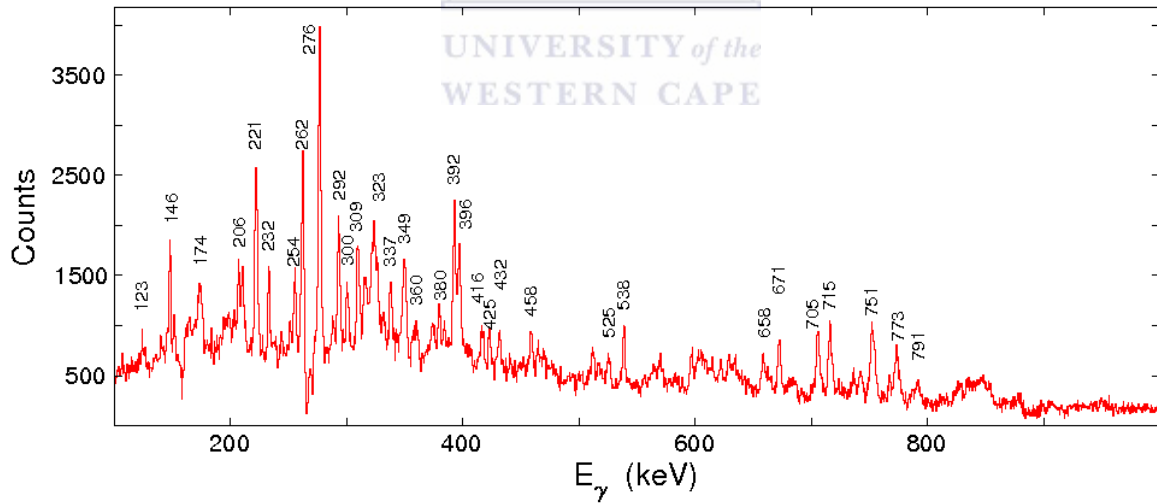


fig 4-13 Gate 238 keV transition

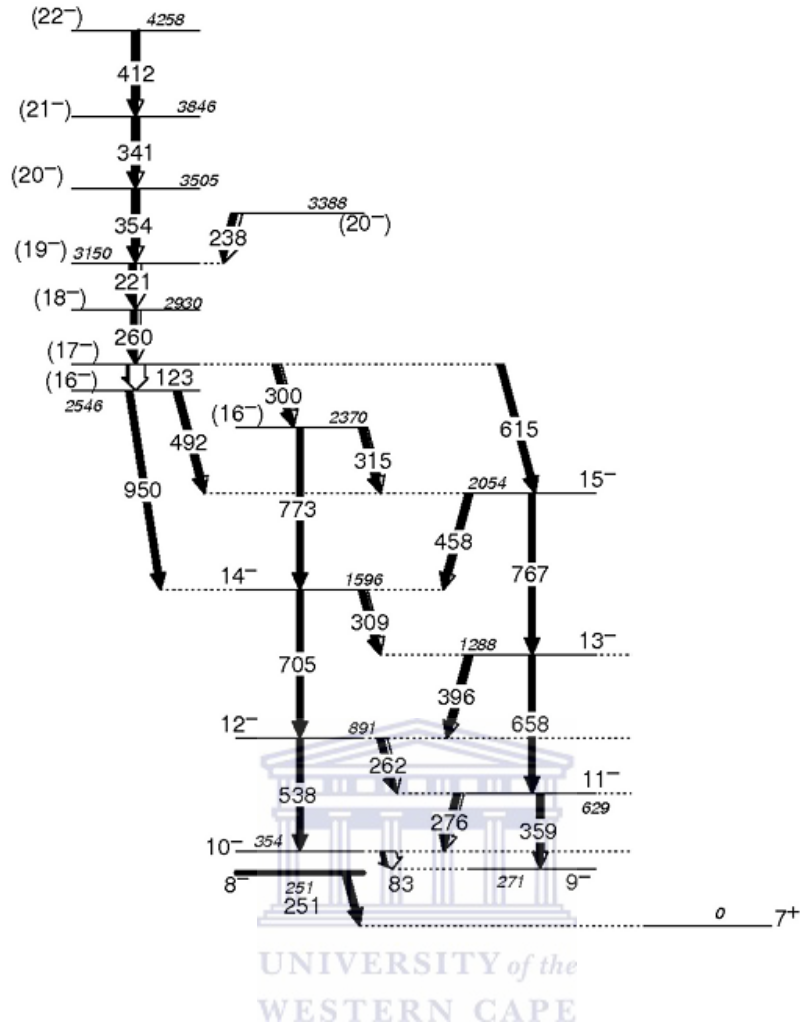


Fig 4-14 Yrast band1, known band plus new transitions

#### 4.2.1.3 **Band2**

Looking at the total projection as shown in Fig. 4-1, the peak 297 keV is quite dominant and not yet placed in the level scheme. Gating on 297 keV transition (see Fig. 4-15) one sees a few interesting features.

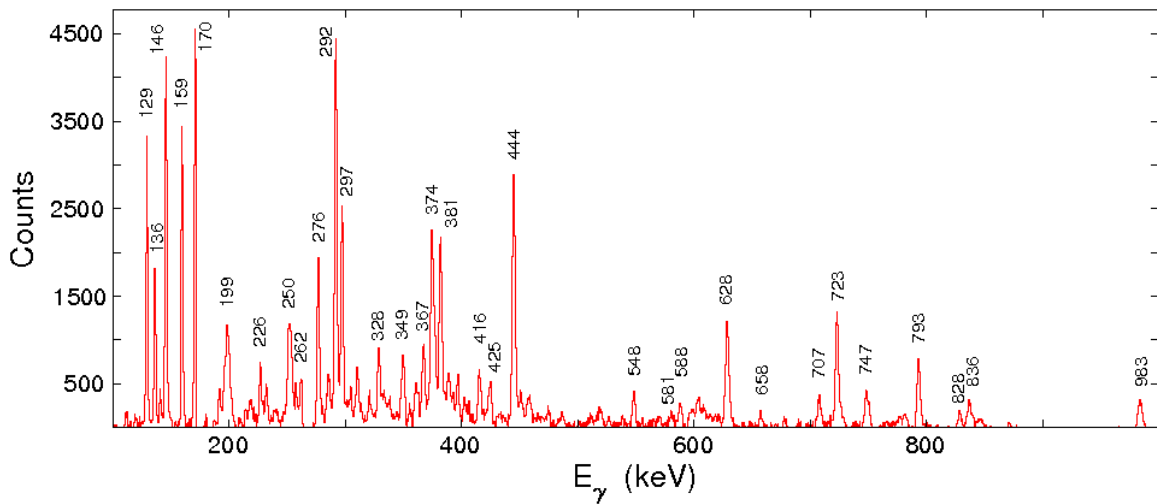


Fig 4-15 Gate on 297 keV transition

The first thing one notices is the several new and very intense gamma rays with energies of 292 keV, 170 keV and 146 keV. The second thing one notices is that the peak 297 keV is a doublet. Doublets are tricky to place. 297 keV transition is a doublet since a peak at 297 keV appears in the spectrum gated on the 297 keV transition. Thus one 297 keV transition has to be in coincidence with another 297 keV transition. Further analysis of the coincidences shows that the strong peaks at 297 keV, 146 keV, 159 keV, 170 keV and 292 keV are all in coincidence with each other, thus they have to be in one decay path. Fig 4-15 shows two out of several possible placements. When examining the intensity of 297 keV transition as seen from the spectrum gated of 297 keV peak, as in Fig. 4-15, one would think that the 297 keV transitions should not be placed on top of each other but rather further away from each other, since the peak 297 keV is not very strong. Another important feature observed in this gated spectrum is the absence of transitions from band1 placed above the 396 keV gamma-ray.

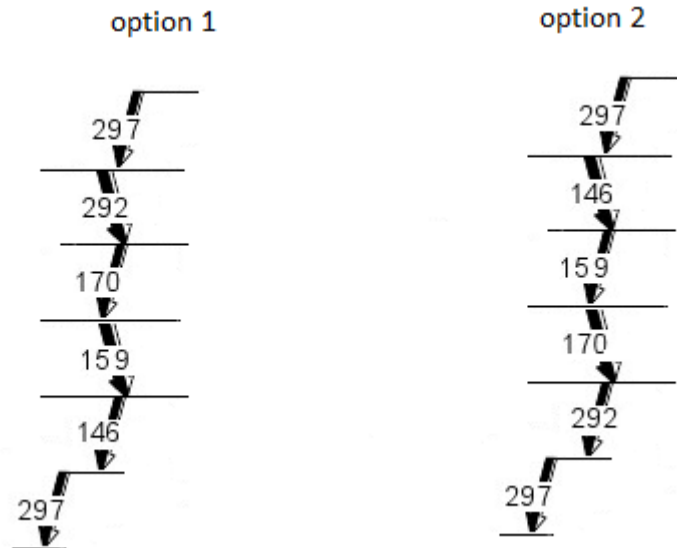


Fig 4-16 Two possible placements of the six transitions which belong to one decay path

Thus the 297 keV transition should in some way be linked to the lower part of band1. The third important feature in this gated spectrum is the presence of strong high energy gamma rays. These include the transition 445 keV, 628 keV, 707 keV, 723 keV, 747 keV, 793 keV, 836 keV and 983 keV. The high energy transitions have two important roles in a level scheme. The first role is that they can be potential cross-overs and the second role they play is that they may link different bands. Investigation of these high energy gamma rays could potentially link the new structure to band1. Starting with the highest energy gamma ray we examined them. The spectrum gated on 983 keV transition is shown in Fig. 4-17.

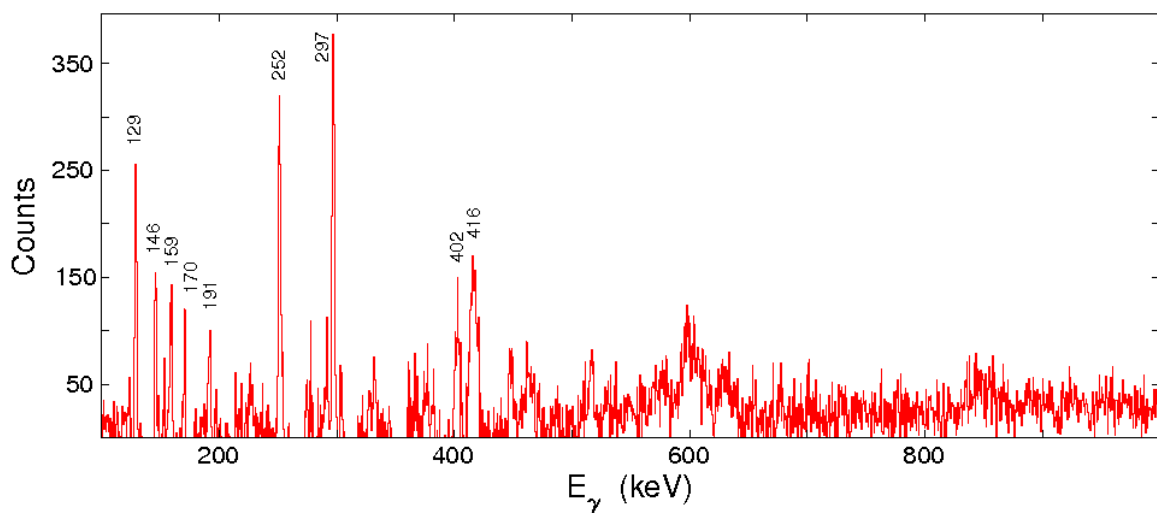


Fig 4-17 Gate on 983 keV transition



This spectrum shows strong 297 keV, 252 keV and 129 keV peaks. The gate on 983 keV transition does not present any evidence yet for the placement of 983 keV peak, except that it is in coincidence with the transitions of the new structure (as shown in Fig. 4-16).

Gating on 836 keV transition, which was the next highest energy gamma ray we see the spectrum shown in Fig. 4-18

There are two strong peaks at 276 keV and 297 keV, while the peak at 129 keV disappears. This shows that 129 keV transition is in coincidence with 983 keV and 297 keV peaks (see Fig. 4-17), while 836 keV transition is in coincidence with 276 keV and 297 keV peaks but anti-coincidence with 129 keV gamma-ray (see Fig. 4-18). One can also notice that  $983 \text{ keV} + 129 \text{ keV} = 276 \text{ keV} + 836 \text{ keV}$ . Further analysis of the gated spectra convinced us to place 836 keV transition directly on top of the  $11^-$  level of band1 and 983keV transition on top of the  $10^-$  level of band1 with 129 keV transition in anti-coincidence with 836 keV peak, as shown in Fig. 4-19.

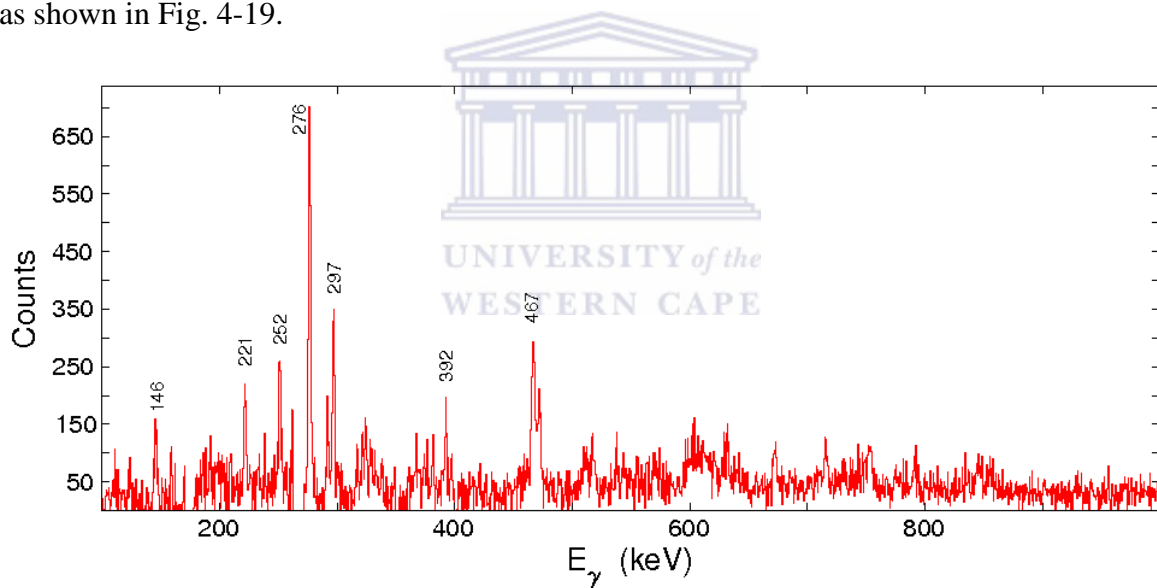


Fig 4-18 Gate on 836 keV transition

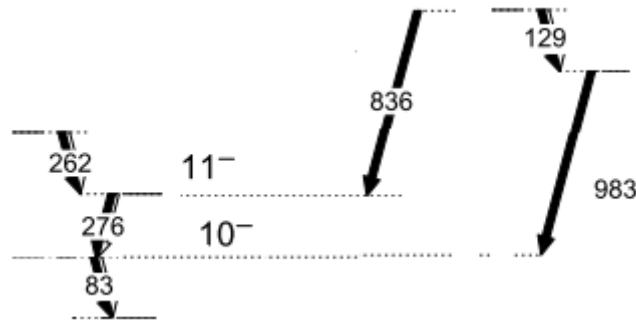


Fig 4-19 The placement of 129 keV, 836 keV and 983 keV transitions.

The next step was to figure out how to place the remaining strong transitions, i.e. 297 keV, 146 keV, 159 keV, 170 keV, 292 keV transitions, etc. Gating on 145 keV transition (see Fig. 4-20) we see the 297 keV peak very strongly.

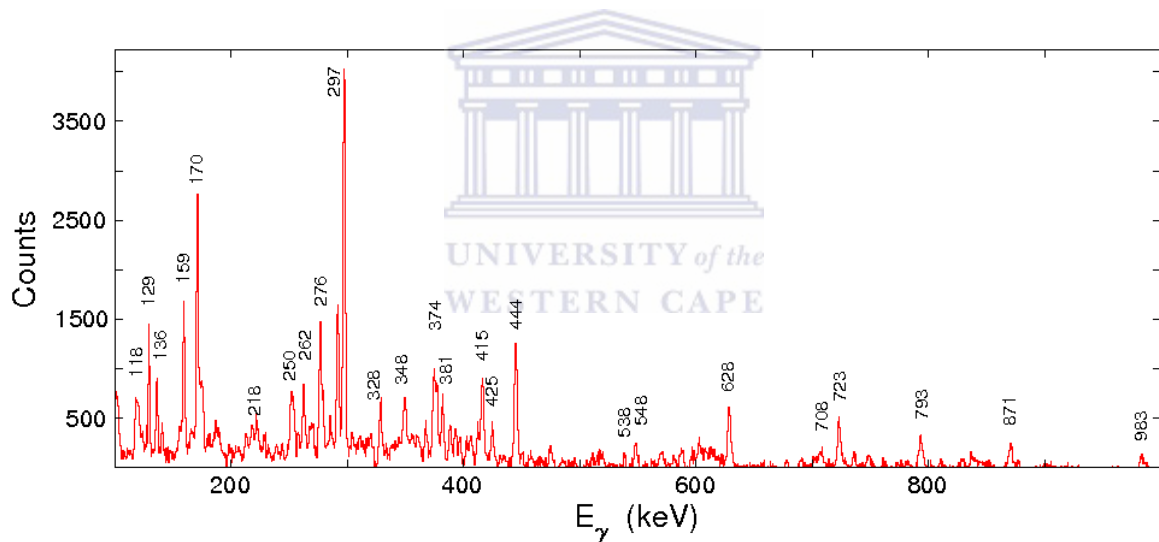


Fig 4-20 Gate set on 146 keV transition

We also see the high energy gamma ray 871 keV. Gating on 871 keV transition (as shown in Fig. 4-21) the peaks 276 keV and 262 keV appear very strongly with 146 keV, 292 keV and 159 keV transitions, etc. showing in coincidence too. It seems as if only one of the members of the 297 keV doublet transition is in coincidence with the 871 keV transition, since the 297 keV peak is very weak. Another observation to note is the energy sum  $871 \text{ keV} + 262 \text{ keV} = 297 \text{ keV} + 836 \text{ keV}$ . The suggested placement of one of the 297 keV transitions and the 871 keV gamma rays as is shown in Fig. 4-22. The 871 keV transition is

placed directly above the 262 keV and 276 keV transitions, linking the new structure to band 1 as shown in Fig. 4-22.

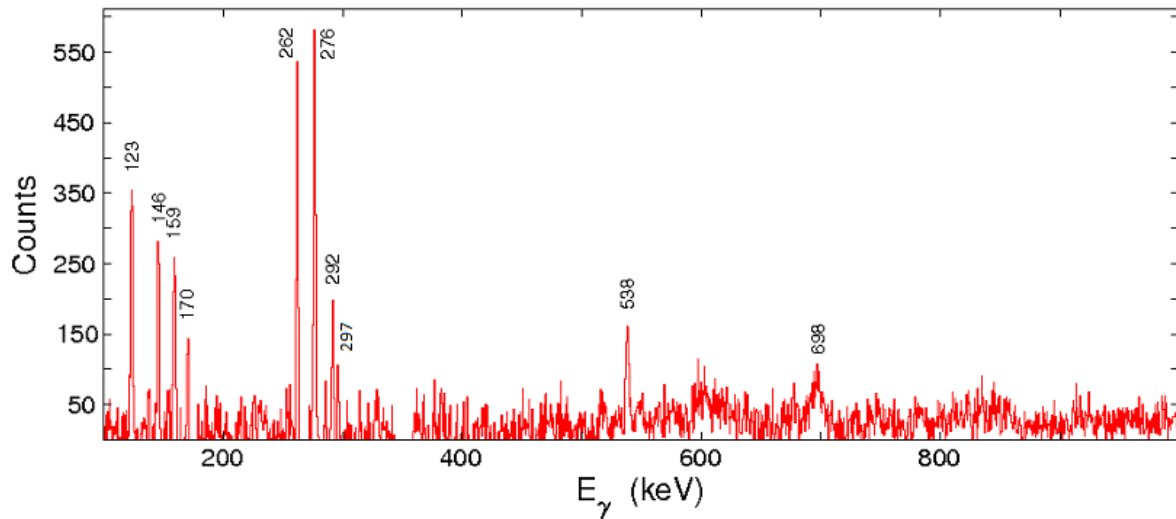


Fig 4-21 Gate on 871 keV transition

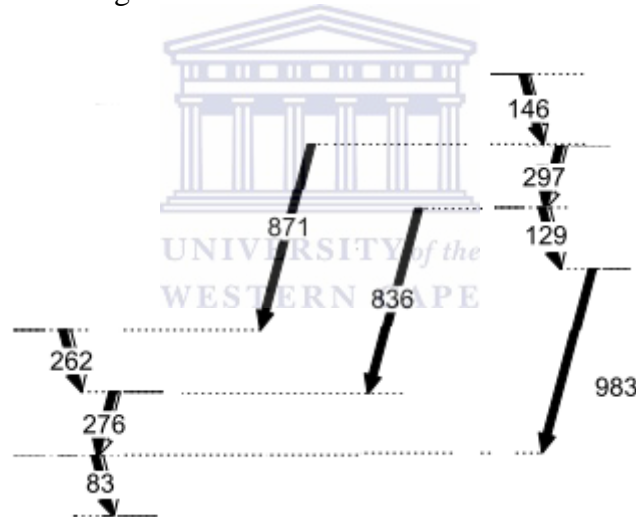


Fig 4-22 Partial level scheme showing building of the level scheme for band2

Before building the level scheme at higher excitation energies, we note the presence of the 191 keV and 252 keV transitions, which are in coincidence with several transitions of this part of band2. Furthermore  $191 \text{ keV} + 252 \text{ keV} = 297 \text{ keV} + 146 \text{ keV}$  while 191 keV transition is found in anti-coincidence with 146 keV transition (see Fig. 4-20) since 191 keV transition is not seen in the spectrum gated by the 146 keV transition. Further coincidence analysis confirmed the placement of the peaks 191 keV and 252 keV in parallel to the peaks 297 keV and 146 keV (see Fig. 4-23). The peaks 170 keV and 159 keV were placed above 146 keV

transition and then the remaining transitions from band2 were placed on top. No cross-overs were found in parallel to 159 keV and 170 keV transitions, thus their order is arbitrary.

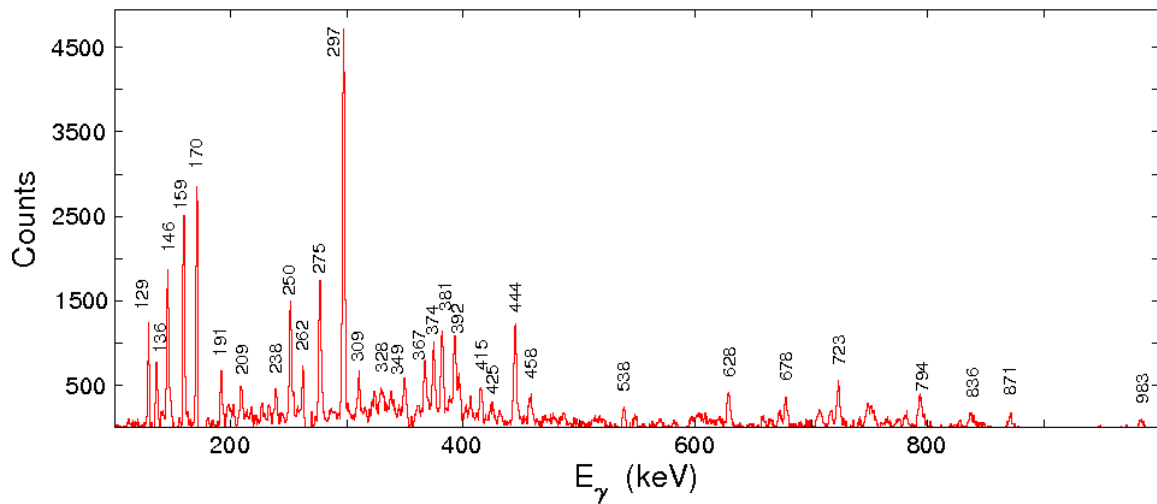


Fig 4-23 Gate on 292 keV transition

The placement of the rest of the transitions in band2 was confirmed by establishing the cross-overs, like 678 keV, 748 keV and 588 keV. The level scheme thus far is seen in Fig. 4-24.

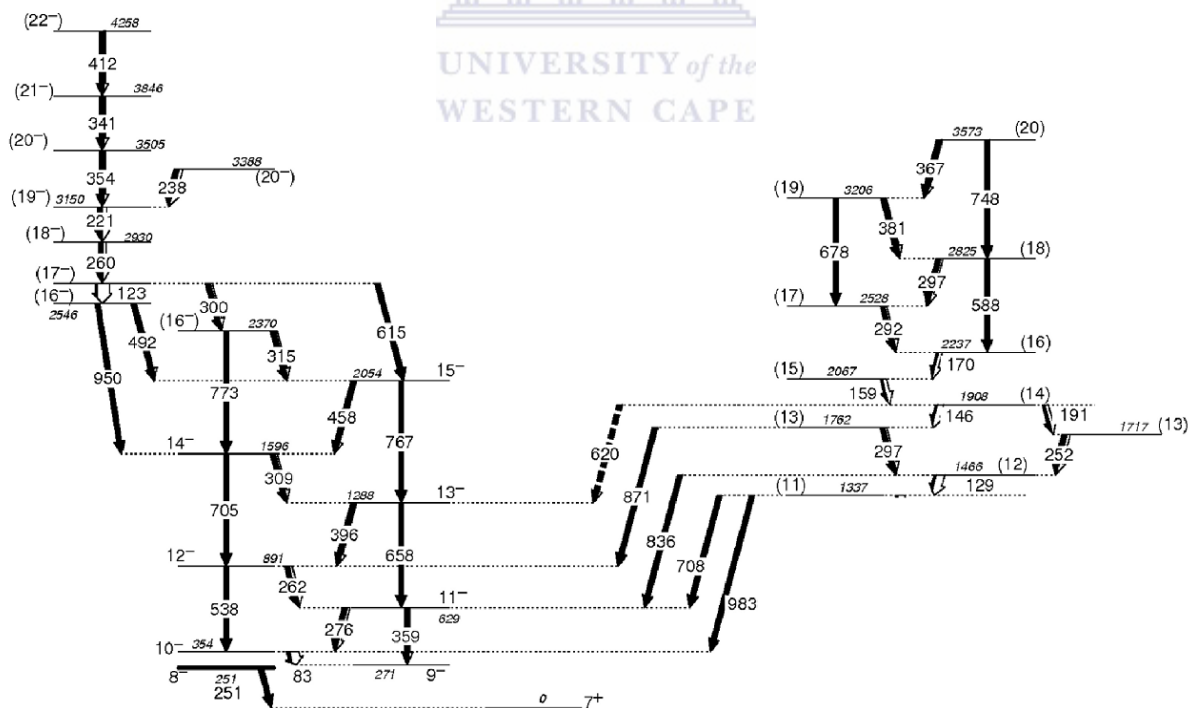


Fig 4-24 The level scheme thus far showing the extension of the known level scheme (band1) and the new band2.

#### 4.2.1.4 Other decays of band 2

Two small structures of transitions were discovered below the 129 keV gamma-ray. They are in anti-coincidence with each other. Gating on 129 keV transition (see Fig. 4-25) the peaks 136 keV, 374 keV and 444 keV are very strong. These strong peaks are not accounted for yet.

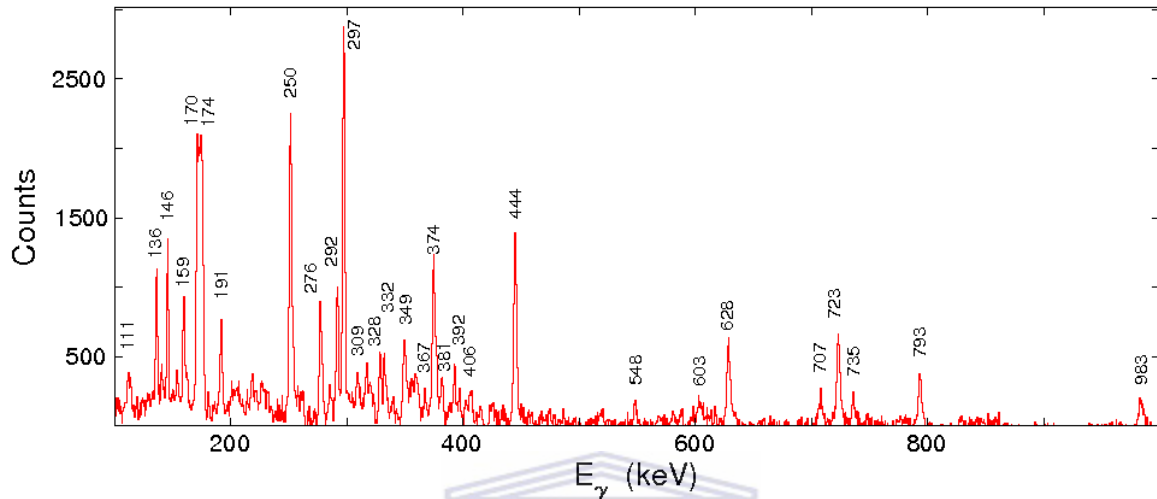


Fig 4-25 gate on 129 keV

Gating on the 444 keV transition (Fig. 4-26) we see that 136 keV, 723 keV, 374 keV and 349 keV peaks are the dominant peaks. Gating on 374 keV transition (see Fig. 4-27) the peak 723 keV disappears and a new peak 793 keV is seen. Therefore 723 keV gamma-ray should be placed in anti-coincidence with 374 keV and 793 keV transitions and should be in anti-coincidence with 444 keV. When gating on 349 keV peak (see Fig. 4-28) both 444 keV and 374 keV transitions are seen but now 793 keV and 723 keV transitions disappear. Furthermore  $444 \text{ keV} + 349 \text{ keV} = 793 \text{ keV}$  and  $349 \text{ keV} + 374 \text{ keV} = 723 \text{ keV}$ . This analysis resulted in the placement of these peaks in the level scheme as shown in Fig. 4-29.

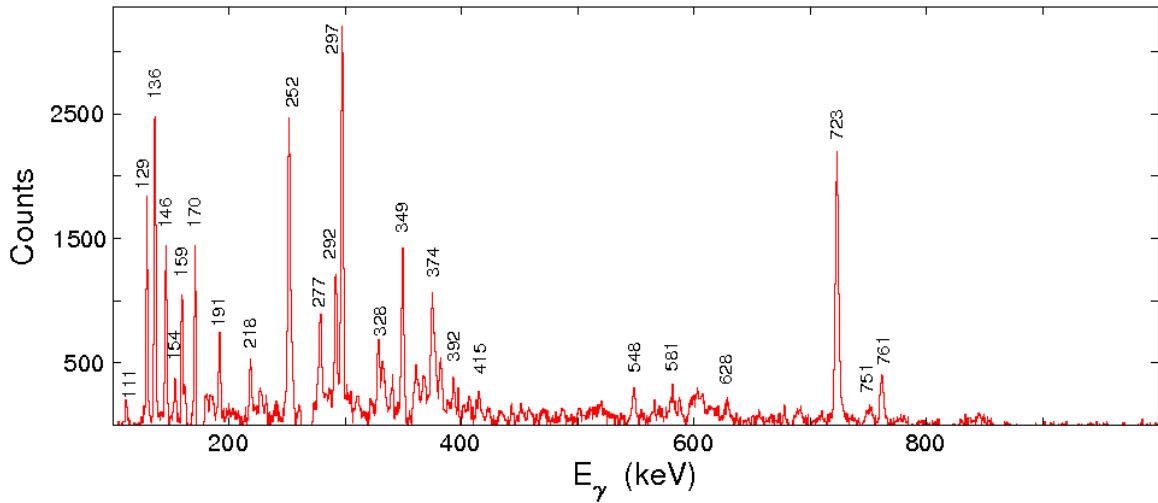


Fig 4-26 gate on 444 keV transition

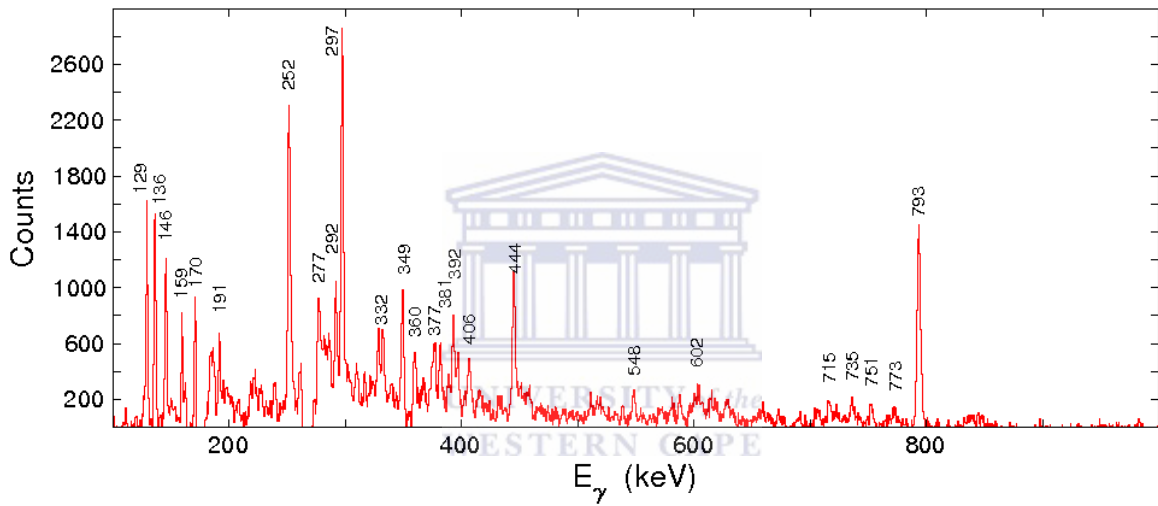


Fig 4-27 Gate on 374 keV transition

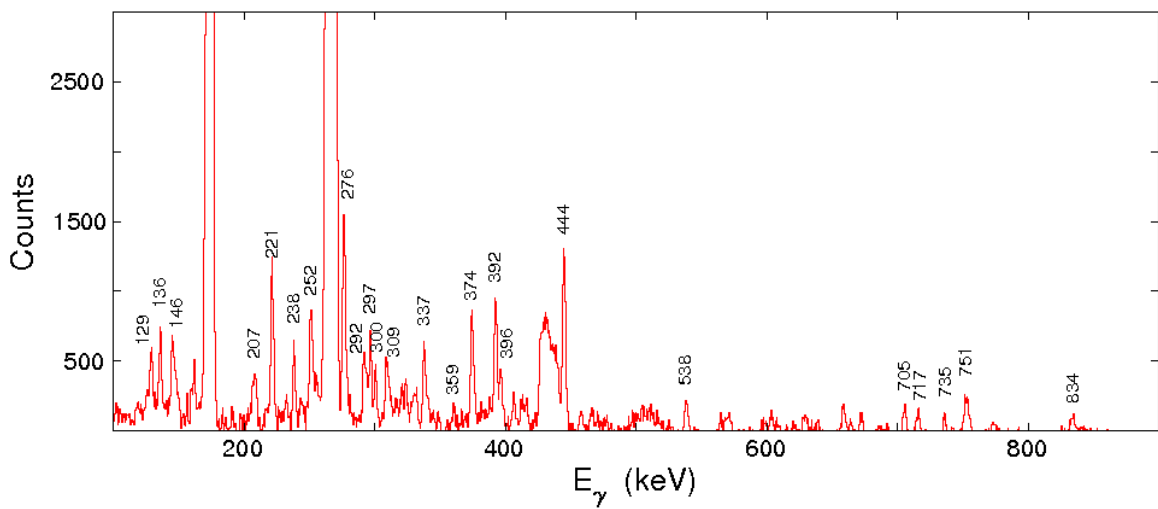


Fig 4-28 Gate on 349 keV transition

This placement is also consistent with the observation that the 136 keV, 444 keV and 374 keV transitions are in anti-coincidence with all of the high energy transitions linking band 2 to band 1, peaks like 983 keV, 836 keV and 871 keV and also with band1 gamma rays. The orientation of this structure could not be unambiguously confirmed. For instance it is possible to place 136 keV transition below the 444 keV transition. Alternatively one could turn around the placement of the gamma ray transitions in this structure. They could have been placed with the 444 keV transition directly below the 129 keV transition and rest of the transitions could be placed accordingly.

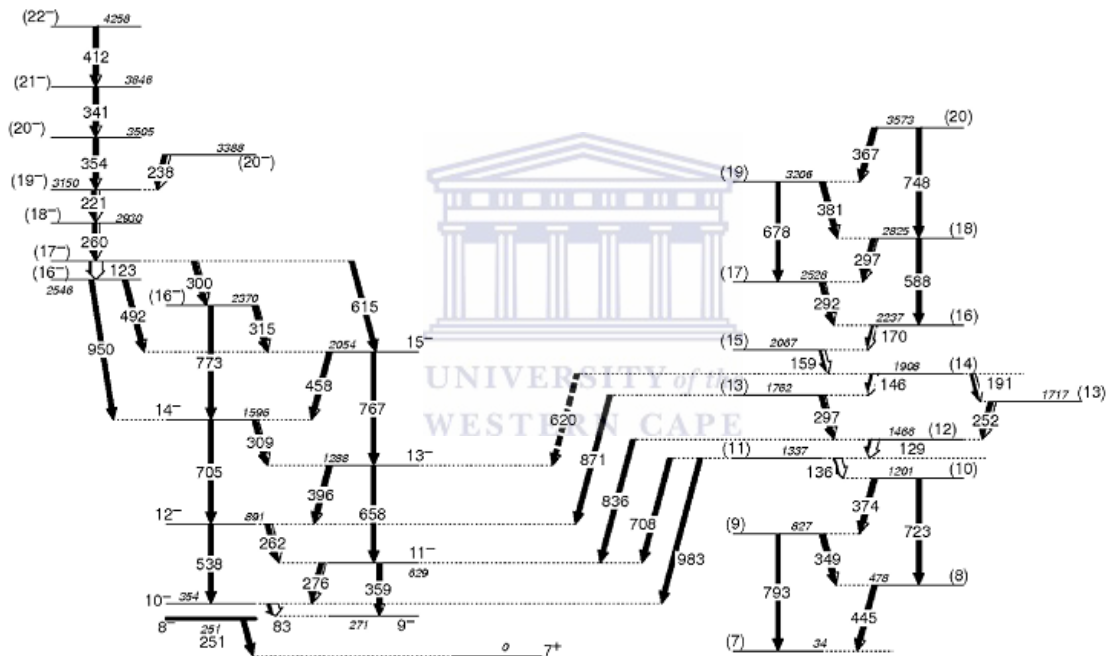


Fig 4-29 The level scheme thus far for <sup>192</sup>Tl

Another structure links the levels at excitation energies 1337 MeV and 34 keV. It consists of the 628 keV, 140 keV, 285 keV, 250 keV, 258 keV, 277 keV and 425 keV transitions. The coincidence analysis of these transition resulted in the placement shown in Fig. 4-30.

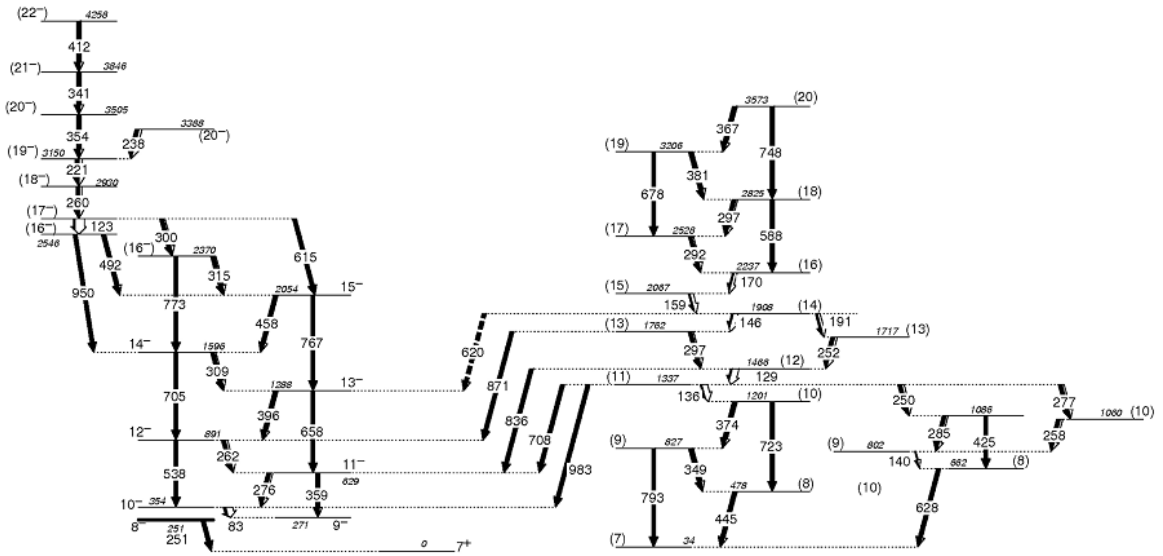


Fig 4-30 the placement of the levels below 129 keV transition



#### 4.2.1.5 **Band3**

This band consists of 328 keV, 377 keV, 360 keV, 581 keV, 657 keV and 688 keV gamma ray transitions. Among them there is the 328 keV doublet transition. Doublets are interesting pairs of transitions because when gating on a doublet transition one observes a spectrum gated on both members of the doublet, as in the case with 328 keV transition (see Fig. 4-31).

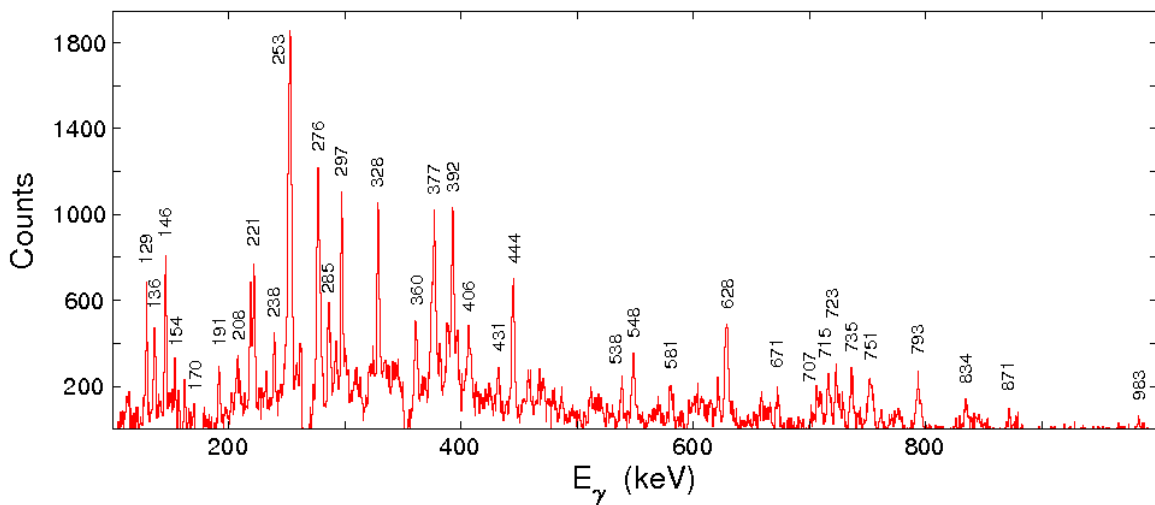


Fig 4-31 The doublet transition 328 keV



One examines such spectra trying to identify close to which other gamma rays the two members of the doublet may be. Looking at Fig. 4-31 two strong peaks 253 keV and 328 keV are noticeable. One can assume as a first step that the two 328 keV and the 253 keV transitions lie close to each other. Two possible ordering of these three gamma rays are shown in Fig. 4-32. Crucially in determining the placement is the observation E2 cross-over transitions. In this case 657 keV cross-over was observed which established that the two 328 keV gamma rays were to be placed on top of each other. Studying the coincidence relationships the other transitions in band3 were placed as shown in Fig. 4-33.

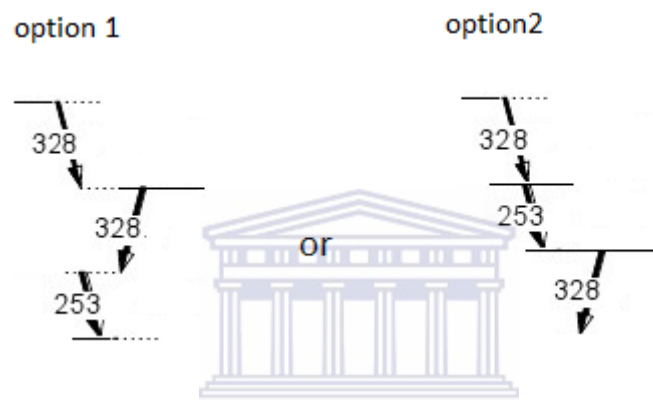


Fig 4-32 two of the several possible placements of the doublet transition 328 keV in band3

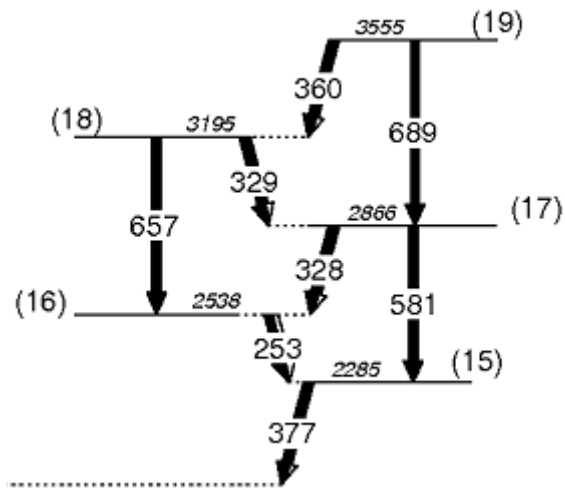


Fig 4-33 showing the placement of the doublet 328 keV, cross-over 657 keV and other coincidence transitions

#### 4.2.1.6 Other difficult cases

Another placement that proved difficult was the 252 keV gamma-ray. These are in fact 250 keV, 252 keV and 253 keV transition all in coincidence with each other. This excludes the 251 keV transition lying below the 8<sup>+</sup> isomer.

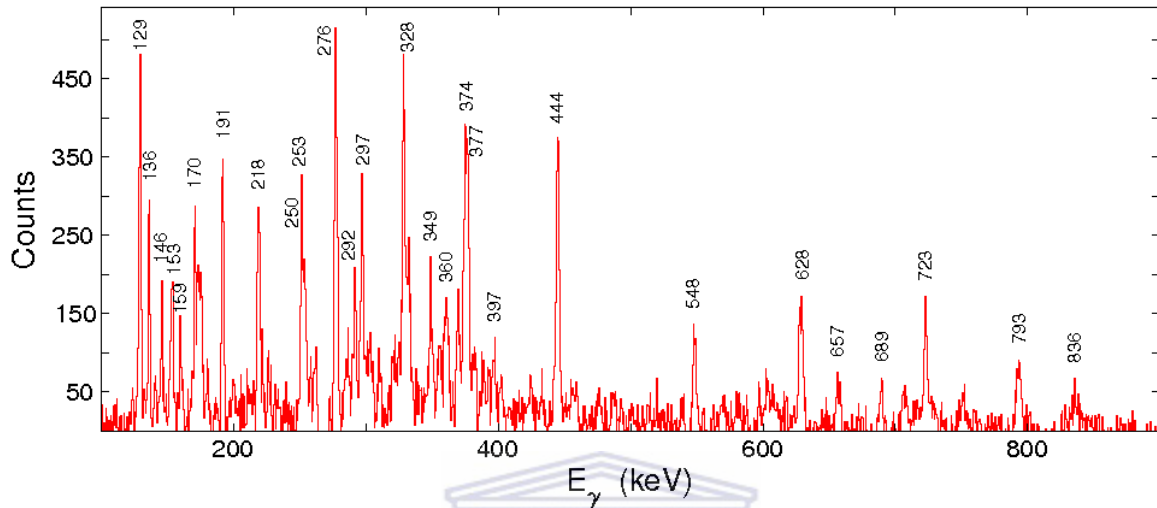


Fig 4-34 gate on 252 keV transition

In the spectrum gated on 252 keV transition (as shown in Fig 4.-34) one sees that 250-253 keV peak is not very strong, meaning that it is most likely that the members of the triplet are not in immediate proximity to each other. Crucially for the placement of this triplet, was to determine other transitions that lie close to the members of the triplet and also to observe cross-overs. In this case gating on the 253 keV member of the triplet showed an increased intensity of the 328 keV doublet transitions, when compared to the spectra gated on 252 keV and 250 keV transitions. The spectrum gated on 253 keV gamma-ray (see Fig. 4-35) shows the transitions 444 keV and 723 keV much weaker. The first assumption is that 444 keV and 723 keV transitions are much further away from the 253 keV transition. Also one notices the appearance of the 377 keV and 360 keV transitions, when gating on 253 keV gamma-ray. Thus the placement of the 253 keV transition is in band 3.

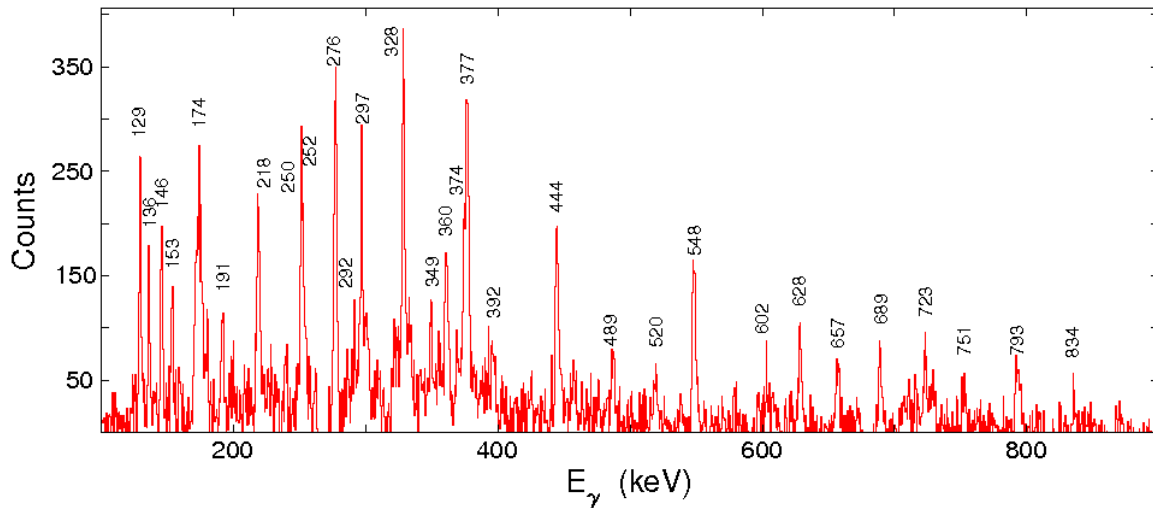


Fig 4-35 gate on 253 keV transition

#### 4.2.1.7 Almost doublet

Peaks that differ by about 1-2 keV are a little easier to place, because they overlap only partly (see Fig. 4-36). This means that when gating on one of them (P2 for example) the gated spectrum shows peaks that are in coincidence with peaks P1 and P3 too. If one has to gate on P1 it is possible to obtain a clearer gated spectrum if instead of gating on the centroid of P1, one gates on the low energy side, choosing energy with say 1-2 keV lower. One problem with this method is that the peaks seen from such a gate are not as intense. But is a helpful way to see the true coincidences.

Consider the real case of peaks like 374 keV and 377 keV transitions which are in coincidence (see Fig. 4-37).

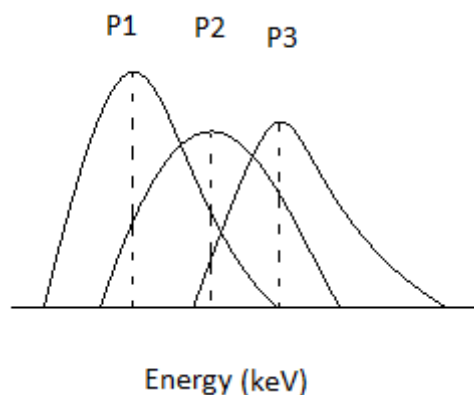


Fig 4-36 overlap of peaks that differ by 1 keV in energy

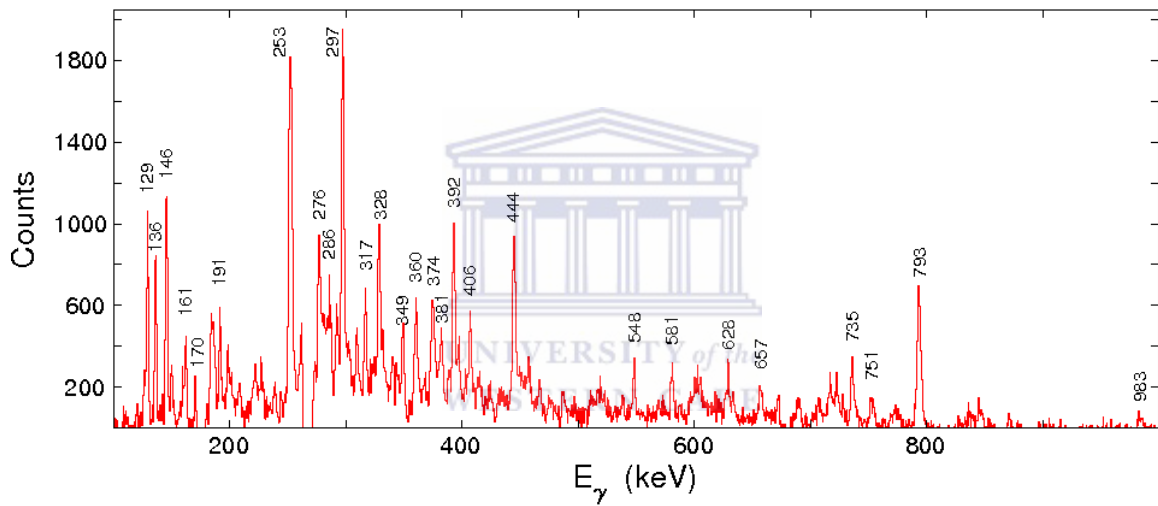
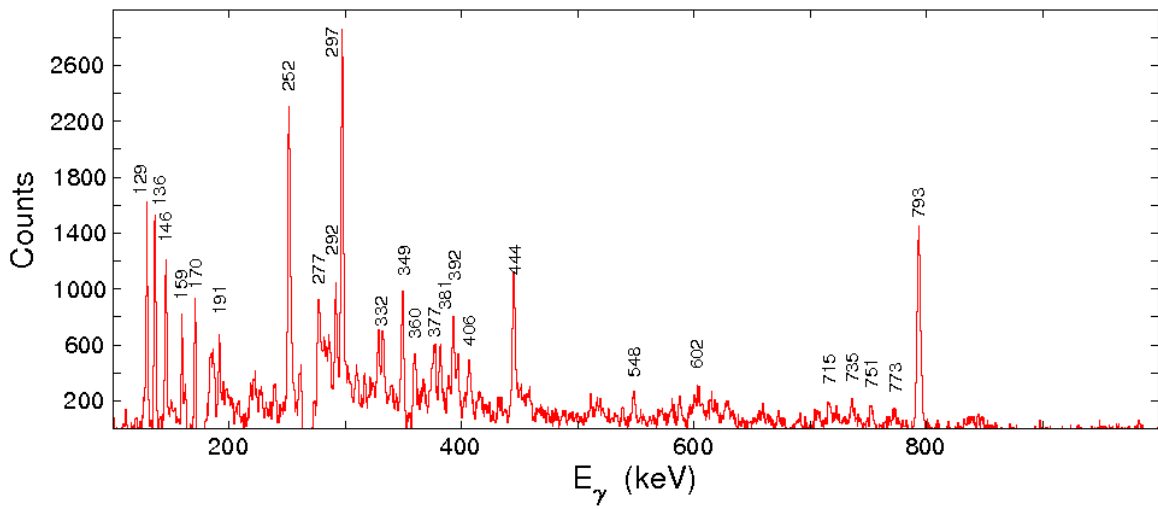


Fig 4-37 top panel is a gate on 374 keV and the bottom is a gate on 377 keV transitions

The two spectra in Fig. 4-37 look very similar but gating on 378 keV and 373 keV transitions (see Figs. 4-38 and 4-39) one can see the difference in the in coincidences with much better.

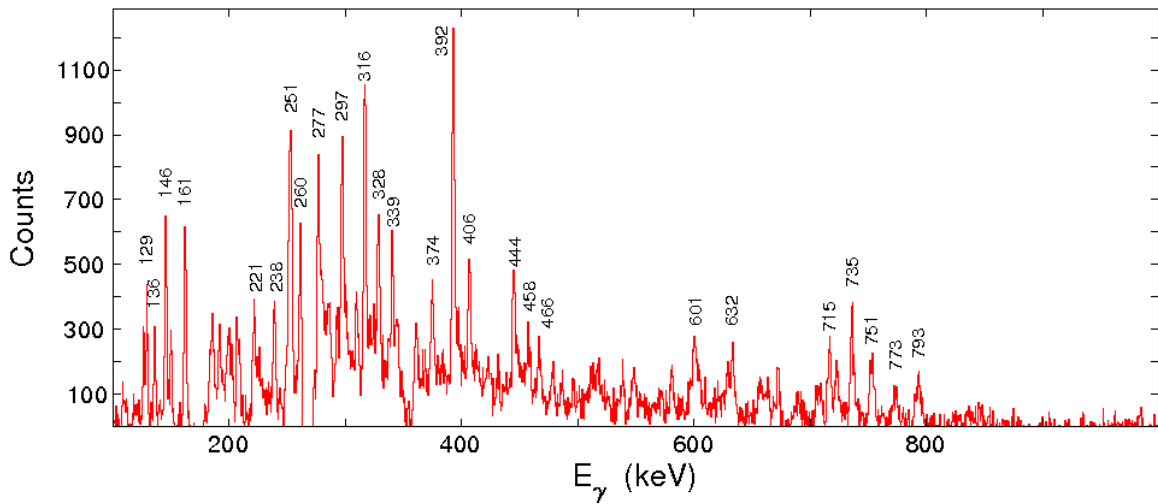


Fig 4-38 gate on 378 keV transition

When looking at Fig. 4-37 the peak 253 keV is very strong. In Fig. 4-38 this peak has a lower energy of  $\sim 252$  keV. This suggests that 377 keV transition is closer to 253 keV transition while 374 keV transition is closer to 252 keV gamma-ray. The spectrum gated on 378 keV transition brings some contaminating transitions from  $^{193}\text{Tl}$ , which need to be ignored. Another clear difference is shown in the intensities of the 349 keV and 793 keV peaks. They must be lying close to the 374 keV transition and much further away from the 377 keV transition.

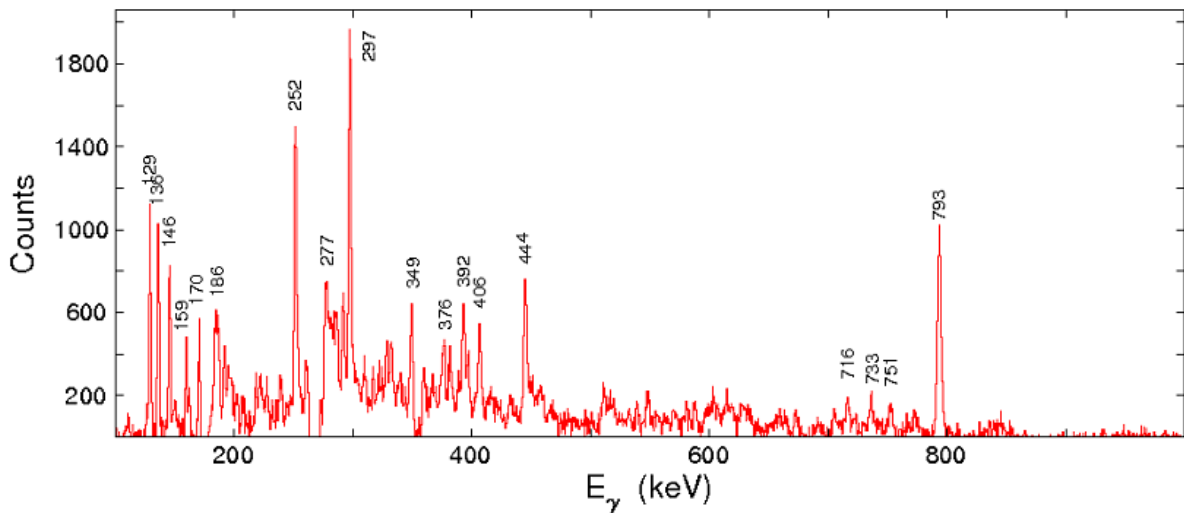


Fig 4-39 gate on 373 keV transition

#### 4.2.1.7 **The final level scheme**

The final level scheme is shown in Fig. 4-40. No spins or parities were measured in this work thus the assignments in brackets are inferred from comparing with the neighbouring nuclei. In some cases, in particular the levels below the 129 keV transition, the spin assignments given in brackets are very uncertain. In the next step of the data analysis angular distribution ratios and linear polarization anisotropies and also gamma ray intensities will be measured.

It should be noted that this gamma-coincidence analysis used the data collected within the two weekends of beam time, when the thin target was used. No chiral partner band to the yrast band was discovered so far in this data. However such search will be performed again when the additional thick targets data is added.



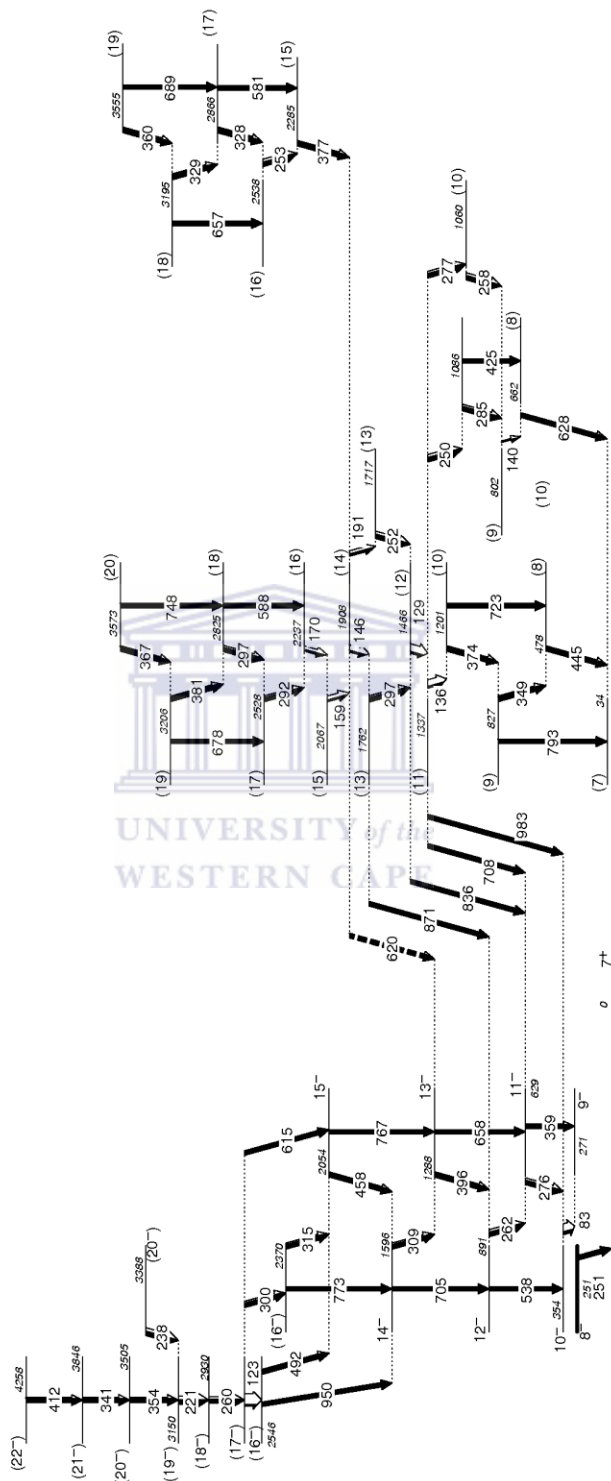


Fig 4-40 The final level scheme

### 4.3 Discussion and conclusion

To account for the observed structure in  $^{192}\text{Tl}$ , deformed shell model and the PRM (particle rotor model) framework will be used.

#### 4.3.1 Deformed Shell model

The deformed shell model is an extension of the shell model that accounts for nuclei that are not spherically symmetric.

The deformed shell model describes single particle orbits in a deformed nuclear potential. Unlike the shell model which assumes a spherically symmetric potential with no interaction between particles the deformed shell model considers deformed nuclear potential in which the particles orbit. Nucleons that are far from closed shells tend to induce deformed nuclear shapes. The nuclei may get into axially symmetric deformed shapes (prolate or oblate) or triaxial shapes.  $^{192}\text{Tl}$  has  $Z=81$  and  $N=111$  with one proton short to fill the 82 shell and 15 neutrons away from filling the 126 shell. With an excess of 15 neutron holes in between closed shells, the shape of this nucleus becomes moderately deformed.

To construct the deformed shell model Hamiltonian several terms are needed. These include the isotropic harmonic oscillator potential  $\hat{H}_0 = -\frac{\hbar^2}{2M}\nabla^2 + \frac{1}{2}M\omega_0^2 r^2$ , which describes the spherically symmetric nuclear potential well. In our case the orbiting nucleons move in a deformed potential. To account for this a term introducing quadrupole deformation is added. The shape of the potential is proportional to the quadrupole field and is given by

$$\hat{H}_d = -\delta M\omega_0 r^2 \frac{4}{3} \sqrt{\frac{\pi}{5}} Y_{20} = -M\omega_0 r^2 \beta Y_{20},$$

Where  $\beta$  is the deformation parameter,  $\delta$  is the shaping parameter and  $Y_{20}(\theta, \phi) = \frac{1}{4} \sqrt{\frac{15}{2\pi}} (3\cos^2\theta - 1)$ . The deformation parameter is related to the quadrupole moment  $Q_0$  and tells us whether the nucleus is prolate or oblate in shape. To a first approximation the quadrupole moment  $Q_0$  is given by

$$Q_0 \cong \frac{3}{\sqrt{5\pi}} R_{av}^2 Z\beta \quad (4.1).$$



When  $\beta < 0$  the nucleus is oblate and when  $\beta > 0$  it is prolate. A zero quadrupole moment occurs when the nucleus has spherical charge distribution. An important term in the interaction is the spin orbit coupling  $\hat{H}_{so} = C\vec{l} \cdot \vec{s}$  of the orbital angular momentum and the spin of the nucleon, where C is the strength of this coupling. This effect splits the subshell (except  $s_{1/2}$ ) into two, e.g.  $h_{9/2}$  and  $h_{11/2}$ . A shaping term is also needed to create an intermediate potential between the square well and the harmonic oscillator potentials, and this force is given by  $\hat{H}_s = D\vec{l}^2$ , where D is a parameter that simulates the deviation from a oscillator potential to a more realistic one. Therefore the single particle Hamiltonian of the deformed well is the sum of the following terms,

$$\hat{H} = \hat{H}_{sp} = \hat{H}_o + \hat{H}_d + \hat{H}_{so} + \hat{H}_s - \frac{\hbar^2}{2M}\nabla^2 + \frac{1}{2}M\omega_o^2r^2 - M\omega_o r^2 \beta Y_{20} + C\vec{l} \cdot \vec{s} + D\vec{l}^2.$$

To find the wave functions one writes

$$\hat{H}\varphi_{\Lambda\Omega} = \left( -\frac{\hbar^2}{2M}\nabla^2 + \frac{1}{2}M\omega_o^2r^2 - M\omega_o r^2 \beta Y_{20} + C\vec{l} \cdot \vec{s} + D\vec{l}^2 \right) \varphi_{\Lambda\Omega} = E_{\Lambda\Omega} \varphi_{\Lambda\Omega},$$

which has a solution  $\varphi_{\Lambda\Omega} = |N\Lambda\Omega\rangle = \sum_{Nlj} a_{Nlj} |Nlj\rangle$  in terms of the spherical bases states.

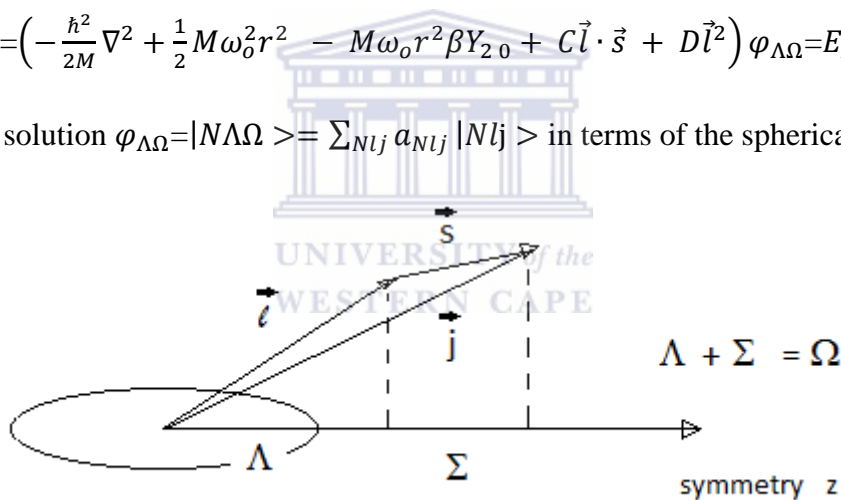


Fig 4-41 Nilsson quantum number  $\Omega$

Here  $\Lambda$  is the projection of  $\vec{l}$  along the symmetry (z)axis,  $\Sigma$  is the projection of  $\vec{s}$  along the z axis,  $\Omega$  is the projection of  $\vec{j}$  along the z axis, N is the principal number of the major shell and  $a_{Nlj}$  are the Clebsch-Gordon coefficients. New quantum numbers are needed, because of the mixing of shell model levels the old quantum numbers like  $l=3$  for the  $f_{7/2}$  state are not conserved. The  $f_{7/2}$  state has  $j=7/2$  at a spherical shape and splits into levels with projections  $|\Omega| = j, j - 1, \dots, 1/2$  when the shape becomes deformed, i.e. four levels since  $|\Omega| > 0$ , for

which  $j$  is not a good quantum number. Thus, one of the new good quantum numbers is the projection  $\Omega$ . The same goes for  $\Lambda = \Omega - \Sigma$ .

The single particle energy of a deformed state for axially symmetric shapes is given by

$$E_N = \left(n_z + \frac{1}{2}\right) \hbar\omega_z + \left(n_{x+y} + \frac{1}{2}\right) \hbar\omega_{x+y},$$

where  $N = n_{x+y} + n_z, n = 0, 1, 2, \dots$ ,

$$\omega_{x+y} = 2\omega_o \sqrt{\left(1 + \left(\frac{4}{5}\pi\right)^{1/2}\beta\right)} \text{ and } \omega_z = 2\omega_o \sqrt{\left(1 - 2\left(\frac{4}{5}\pi\right)^{1/2}\beta\right)}.$$

The single particle energy levels are conveniently plotted in the Nilsson diagrams as a function of  $\beta$  for protons and neutrons (as shown in Fig 4-42).

The Nilsson diagrams for protons and neutrons are different. This is because of the Coulomb repulsion the protons feel. The Coulomb force modifies the potential depth increasing the Fermi energy for protons. The Fermi energy level is the highest level which is filled with the available number of protons or neutrons, assuming that the nucleus has zero excitation energy.  $^{192}\text{Tl}$  is a deformed nucleus. Experimentally it is usually the spectroscopic quadrupole moment  $Q$  that is measured (this is the quadrupole moment when measured in the laboratory frame) while the intrinsic quadrupole moment  $Q_o$  reflects the nuclear quadrupole deformation. These two quadrupole moments are related by

$$Q = \frac{3K^2 - I(I+1)}{(I+1)(2I+3)} Q_o \quad (4.2),$$

where  $I$  is the nuclear spin and  $K$  is the projection of  $I$  on the symmetry axis.

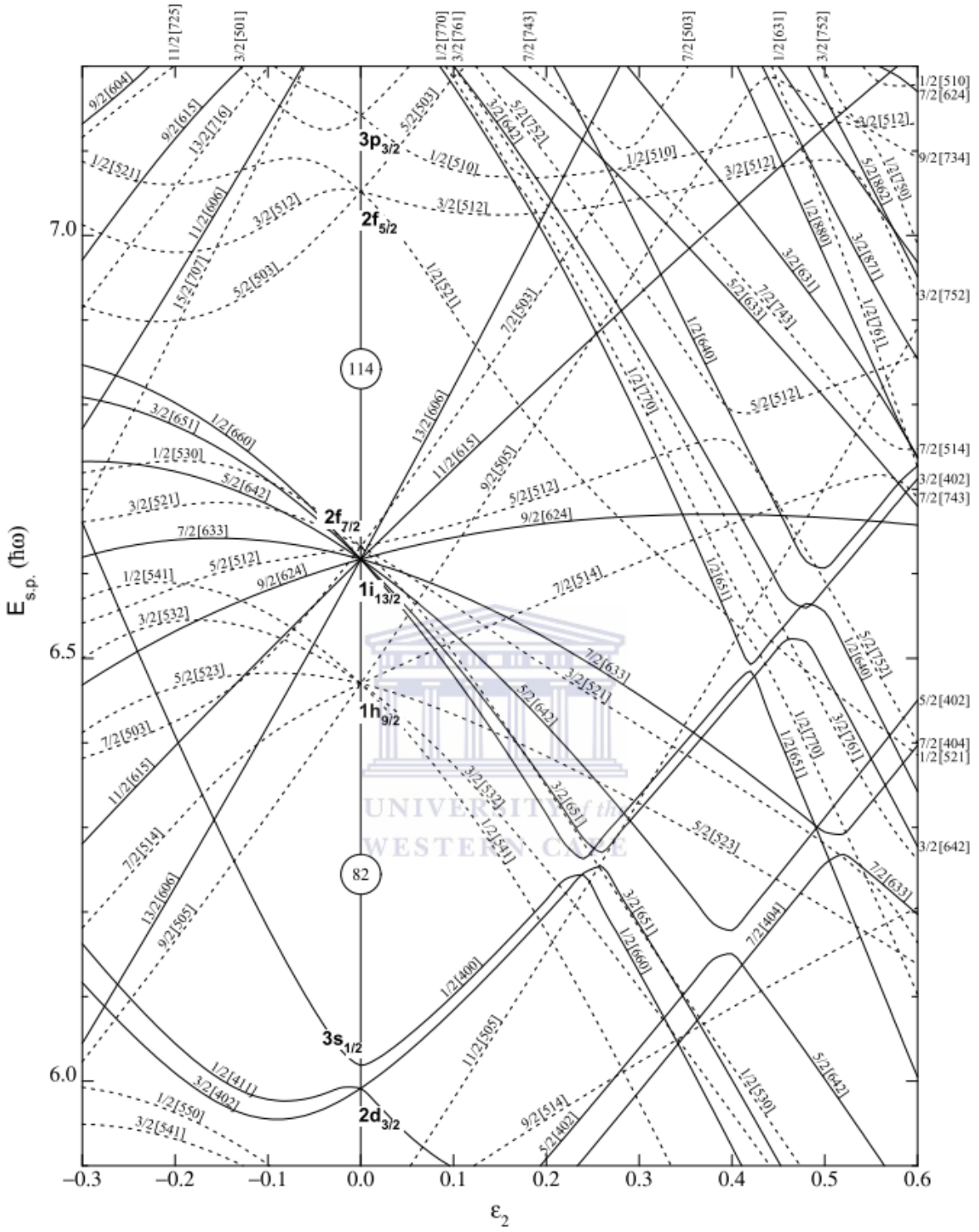


Fig. 4-42a Nilsson diagram for protons  $50 < Z \leq 82$  [Nil12]

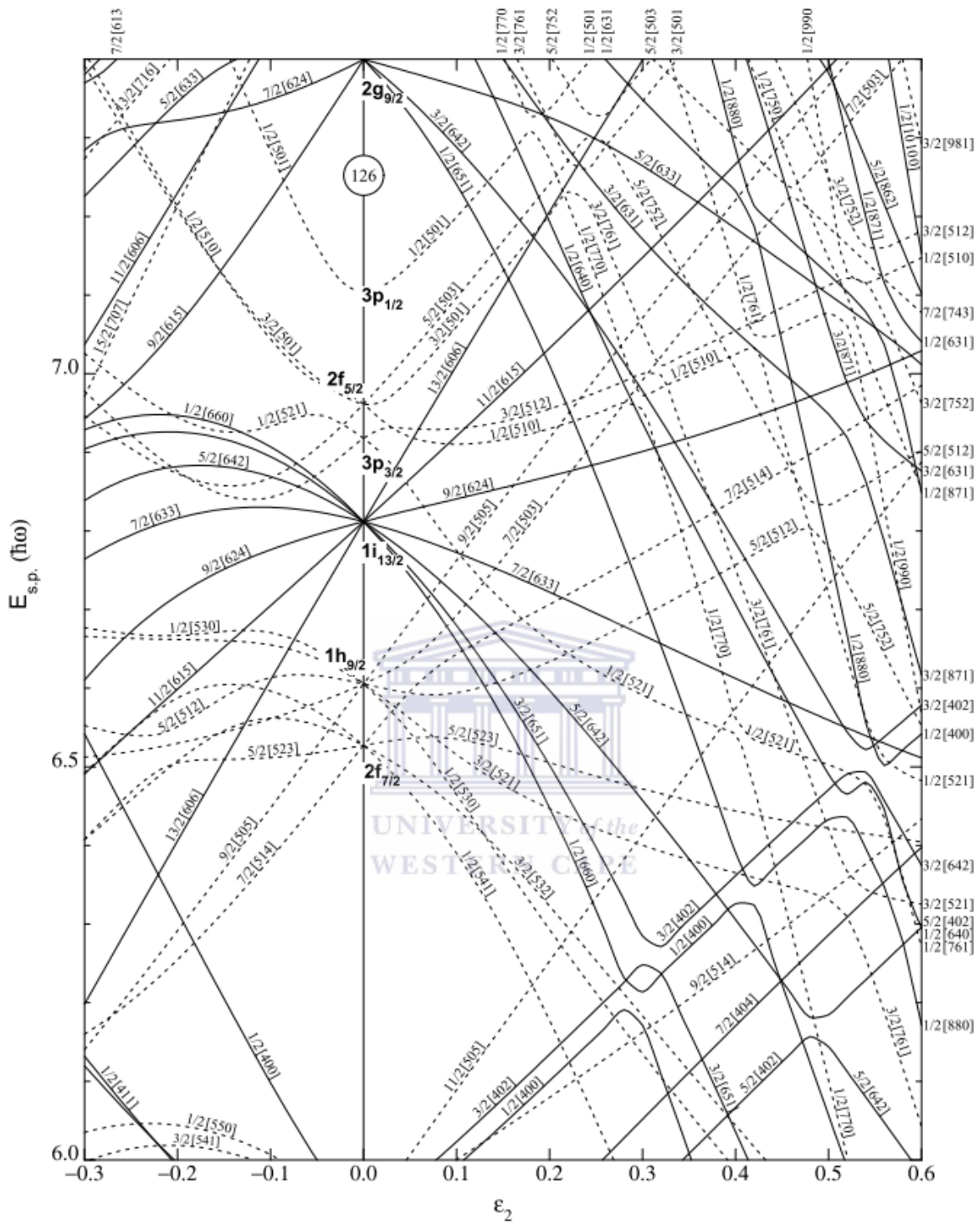
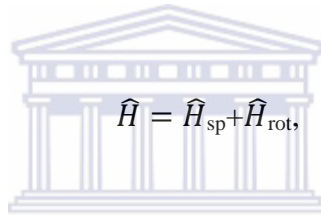


Fig 4-42b Nilsson plot for neutrons  $82 \leq N \leq 126$ [Nil12]

### 4.3.2 Band1

In  $^{192}\text{Tl}$  the rotational bands are based on the  $I^\pi = 8^-$  state, thus this state is of prime interest. The actual ground state in  $^{192}\text{Tl}$  is an isomer  $2^-$  (lifetime =9.6 min) that undergoes positive beta decay or electron capture to  $^{192}\text{Hg}$ .  $^{192}\text{Tl}$  has 81 protons and oblate deformed shape. Looking at the Nilsson diagram for protons, this makes the Fermi level for protons to lie at the bottom of the  $h_{9/2}$  shell, which means that the unpaired proton will occupy an orbital originating from the  $h_{9/2}$  shell. Similarly the Fermi level for neutrons lies at the top of the  $i_{13/2}$  shell, i.e. the unpaired neutron occupies an orbital originating from the  $i_{13/2}$  shell.

Since  $^{192}\text{Tl}$  is rotating (deformed nuclei can be observed to rotate while spherical nuclei cannot) the PRM (particle rotor model) can be used. The wave functions are then given by  $\Psi = \varphi_{\Lambda\Omega} \cdot \Phi_{rot}$ , where  $\varphi_{\Lambda\Omega}$  are the intrinsic deformed wave functions and  $\Phi_{rot}$  are the rotational wave functions of the nucleus in the laboratory frame. The new rotational Hamiltonian is



$$\hat{H} = \hat{H}_{sp} + \hat{H}_{rot},$$

where

$$\hat{H}_{rot} = \frac{\hbar^2}{2J} (I^2 + j^2 - 2\vec{I} \cdot \vec{j}).$$

The Coriolis term  $\vec{I} \cdot \vec{j}$ , when sufficiently strong, tends to align the angular momentum of the unpaired nucleons towards the rotational axis, which is perpendicular to the symmetry axis.

Looking at the neighbouring nuclei one can get a hint as to how the odd proton and neutron in  $^{192}\text{Tl}$  will behave. Looking at  $^{191}\text{Hg}$  (which has  $Z=80$  and  $N=111$ ) one can examine the coupling of the unpaired neutron as the nucleus is an isotone of  $^{192}\text{Tl}$  and has the same Fermi level as in  $^{192}\text{Tl}$ . One can note that similar quadrupole deformation is expected in both isotones. The ground state band in  $^{191}\text{Hg}$  is shown in Fig. 4-43 and one can see that this band is built of E2 transitions above a band head spin  $I^\pi = 13/2^+$  and therefore decoupled.

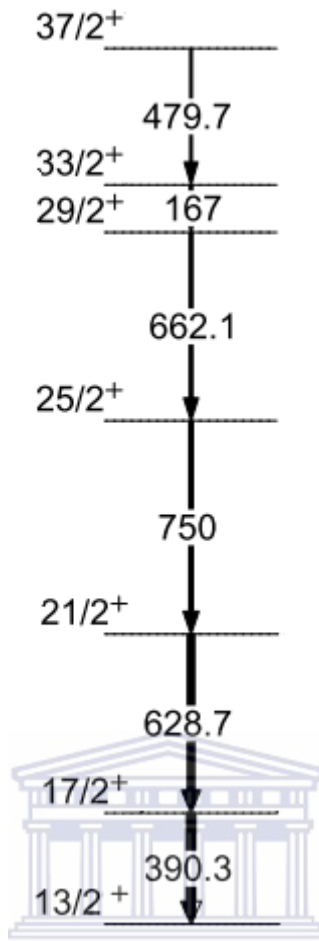


Fig 4-43 Yrast band in  $^{191}\text{Hg}$ , showing decoupled structure. The band is assigned to  $\nu 1i_{13/2}$  configuration.

Decoupled band occurs when the odd neutron moves independently from the rotating core. The energies of the levels in the band are given by as

$$E(I) = \frac{\hbar^2}{2J} [(I - j)(I - j + 1)] \quad (4.3),$$

where  $I$  is the spin of the state and  $j$  is the total angular momentum of the odd neutron. The band head has spin  $I=j$  and parity determined by the configuration of the odd neutron. Since the neutron occupies a level originating in the  $i_{13/2}$  shell, this decoupled band starts at  $I^\pi = 13/2^+$ .

On the other hand  $^{193}\text{Tl}$  has an odd proton and exhibits the rotational band shown in Fig. 4-44. This band is a strongly coupled band. Strongly coupled bands occur when the odd proton couples its motion to the rotation of the core. This happens when the angular momentum of

the odd nucleon has a large projection along the symmetry axis, and for low rotational frequencies where the Coriolis force is not very strong. The energy levels are given by

$$E(I) = \frac{\hbar^2}{2J} [(I(I+1) - K^2)] \quad (4.4),$$

where  $K$  is the projection of the total angular momentum along the symmetry axis.

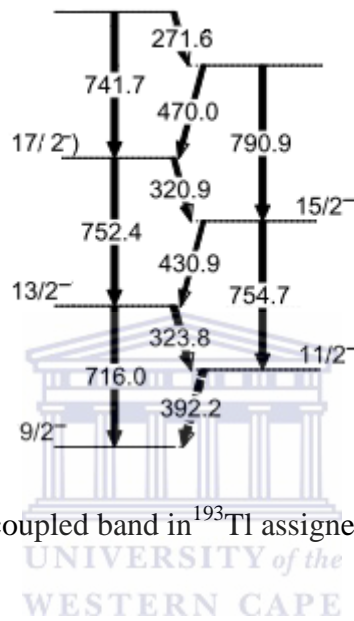


Fig 4-44 Yrast strongly coupled band in  $^{193}\text{Tl}$  assigned to  $\pi h_{9/2}$  configuration.

Since  $^{191}\text{Hg}$  is a neighbouring isotone and  $^{193}\text{Tl}$  is an isotope of  $^{192}\text{Tl}$  we expect that in  $^{192}\text{Tl}$  there will be a similar coupling of the two unpaired nucleon states, i.e.  $\pi 1h_{9/2} \otimes \nu 1i_{13/2}$ . The yrast rotational bands starts at the  $8^-$  level. This is exactly what one gets when considering the  $\pi 1h_{9/2} \otimes \nu 1i_{13/2}$  configuration. The angular momenta of the two nucleons are virtually perpendicular since  $\pi 1h_{9/2}$  has projection  $\Omega_p = 9/2$  along the symmetry axis and  $\nu 1i_{13/2}$  has projection  $\Omega_n = 1/2$ . Depending on the strength of the Coriolis force the neutron can be strongly coupled or decoupled. In this case, as confirmed by the properties of the band in  $^{191}\text{Hg}$  isotone the neutron angular momentum is decoupled. That means  $\Omega_n$  is not a good quantum number but the projection of the angular momentum along the rotational axis,  $i_n$  is. This coupling of the two angular momenta is illustrated in Fig. 4-45. Therefore the band head spin can be calculated as:

$$I_o \approx \sqrt{(\Omega_p)^2 + (i_n)^2} \quad (4.5)$$

$$\approx \sqrt{\left(\frac{9}{2}\right)^2 + \left(\frac{13}{2}\right)^2} \approx 8.$$

Configurations like the  $\pi 1h_{9/2} \otimes \nu 1i_{13/2}$  configuration in  $^{192}\text{Tl}$  are in principal suitable for forming a chiral system. The necessary requirement for a chiral system is to have three perpendicular angular momentum vectors. The proton and neutron in the  $\pi 1h_{9/2} \otimes \nu 1i_{13/2}$  configuration provide two orthogonal angular momenta. Thus the only remaining requirement is to have the rotational angular momentum pointing in the perpendicular direction to the proton and neutron angular momenta (see Fig. 4-46). This will occur if the nuclear shape is triaxial.

In principal the coupling of the two angular momenta with good projections along the symmetry axis of  $\Omega_p$  and  $\Omega_n$  results in a total K value,  $K_{tot} = \Omega_p \pm \Omega_n = 4$  or  $5$ .

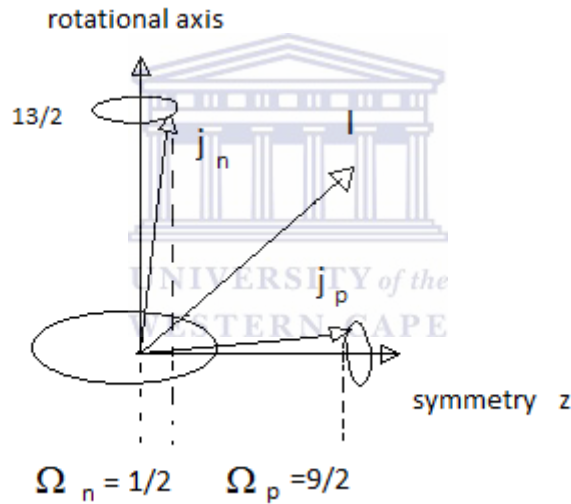


Fig 4-45 Perpendicular coupling of the proton and neutron angular momenta in  $^{192}\text{Tl}$

Inserting  $K_{tot} = 4$  and  $I = 8$  into (4.2) and using the measured quadrupole moment  $Q$  for the  $8^-$  level in  $^{192}\text{Tl}$  one can estimate the intrinsic quadrupole moment  $Q_o$ :

$$0.44\text{eb} = Q = \frac{3 \cdot 4^2 - 8(8+1)}{(8+1)(2 \cdot 8 + 3)} Q_o = -0.14 Q_o.$$

Therefore  $Q_o = -3.143$  eb. Now with the aid of equation (4.1)

$$-3.143 = \frac{3}{\sqrt{5\pi}} R_{av}^2 Z \beta.$$

Solving this for  $\beta$  gives



$$\beta = \frac{-3.143}{\frac{3}{\sqrt{5\pi}} \cdot 81 \cdot (1.2 \cdot 192^{1/3})^2} = -0.11,$$

which is the quadrupole deformation if the nuclear shape is axially symmetric. In the published literature quadrupole deformation of 0.13-0.17 was applied for the neighbouring thallium and mercury isotopes in the 190-194 mass range which was also used.

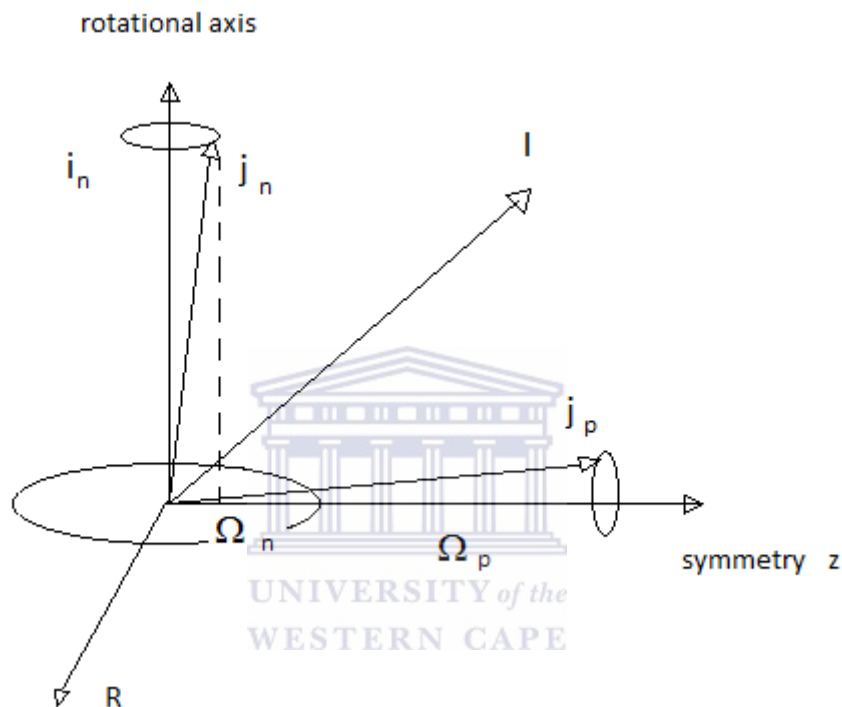


Fig 4-46 Chiral system formed by three orthogonal angular momenta

The level energy and spin in band1 increases due to the rotation of the nucleus. This band consists of the levels with  $I = 8, 9, 10, \dots$  up to  $16^-$  for  $^{192}\text{Tl}$ . At this point the band crossing occurs as is indicated by the decreasing energy of the 615 keV E2 transition.

#### 4.3.3 **Band4**

At increased rotational angular momentum and rotational energy the Coriolis force increases. The Coriolis force increases to a point at which a pair of neutrons is broken.

One can examine bands in neighbouring mercury and thallium isotopes in order to find out more about the pair breaking. First, one notices that in neighbouring nuclei it is a neutron pair

that breaks first. The two neutrons may both occupy  $i_{13/2}$  orbitals and then the band has the same parity as the yrast band.

For example in  $^{195}\text{Tl}$  a pair breaks and the two neutrons occupy  $i_{13/2}$  orbitals (see Fig. 4-48).

When a neutron pair is broken in the  $i_{13/2}$  shell, it is not possible that both neutrons to occupy the  $1/2^+$  [660] orbital since the Pauli principle forbids two fermions with the same quantum numbers. Thus the second neutron settles in the  $3/2^+$  [651] Nilsson orbital with projection  $K = 3/2$  along the symmetry axis (see Fig. 4-47). But the Coriolis force is strong and aligns the two neutrons along the rotational axis, giving a characteristic alignment of  $13/2 + 11/2 = 12$ , fig 4-47. Since in  $^{195}\text{Tl}$  the two neutrons are coupled with the odd proton  $\pi 1h_{9/2} \otimes \nu 1i_{13/2}$  the band head spin of these rotational bands will be

$I = \sqrt{(9/2)^2 + (12)^2} = 25/2$ , with parity of  $\pi_p \cdot \pi_n^2 = -1 \cdot (+1)^2 = -1$ . Indeed this is observed in  $^{195}\text{Tl}$  (see Fig. 4-48).

Consider another example in neighbouring  $^{191}\text{Hg}$  isotone a neutron pair breaks, with both  $i_{13/2}$  neutrons aligning along the rotational axis. This is indicated by the gain in the alignment at the band crossing (see Fig 4-41). This makes aligned three odd  $i_{13/2}$  neutrons. The third neutron cannot have the same projection as the other two and thus the third neutron settles in the positive parity  $7/2^+$  [633] orbital. Coriolis force aligns all three neutrons along the rotational axis with alignments of  $13/2$ ,  $11/2$ , and  $9/2$  (see Fig. 4-50). Therefore the band head spin of this decoupled band in  $^{191}\text{Hg}$  will be  $I = j = 13/2 + 11/2 + 9/2 = 33/2$  (see Fig. 4-43).

In  $^{195}\text{Tl}$  these three neutrons will be coupled with the odd proton  $\pi 1h_{9/2} \otimes \nu 1i_{13/2}$  (see Fig. 4-49). One would thus expect a rotational band built on a level with spin

$$I = \sqrt{\left(\frac{33}{2}\right)_n^2 + \left(\frac{9}{2}\right)_p^2} = 17$$

and with negative parity.

An interesting point to note is that band 4 seems to start at a slightly lower spin. In our case a more detailed experimental measurements need to be done on this band to confirm the actual spin.

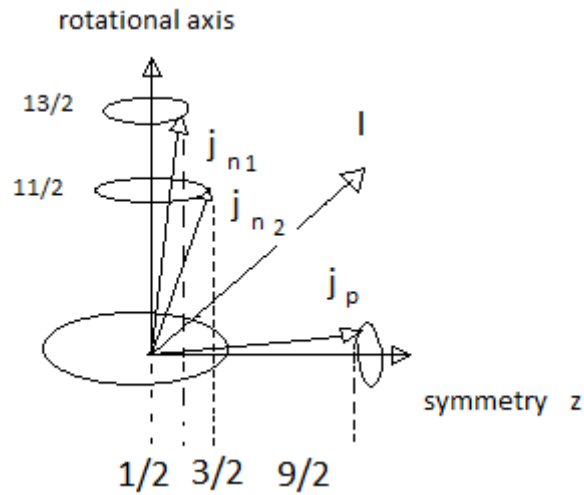


Fig 4-47 The alignment of two neutrons along the rotational axis

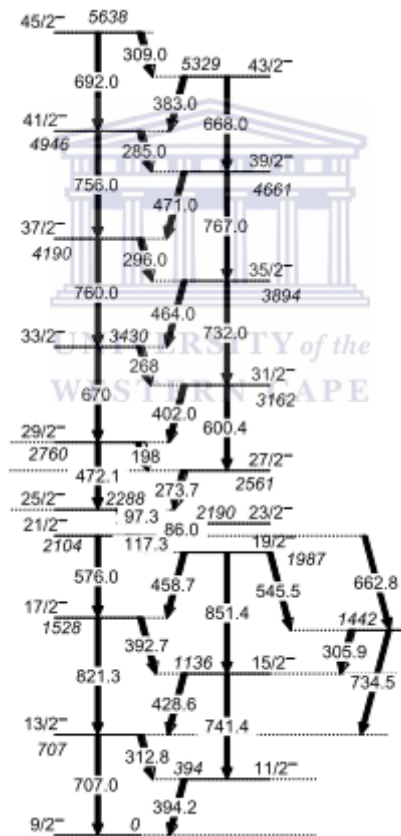


Fig 4-48 Showing the band due to the alignment of the two  $i_{13/2}$  neutrons in  $^{195}\text{Tl}$  (it has

$$I = \sqrt{(9/2)^2 + (12)^2} = 25/2)$$

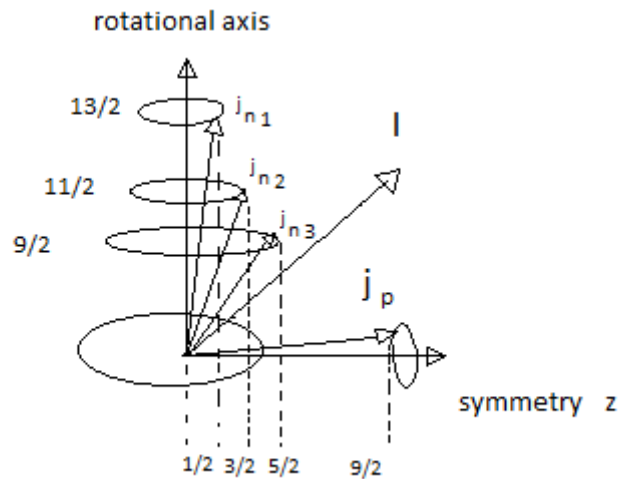


Fig 4-49 The alignment of three  $i_{13/2}$  neutrons along the rotational axis coupled to an odd proton  $h_{9/2}$

#### 4.3.4 **Band2 and band3**

Going back to  $^{195}\text{Tl}$  as a comparison, band 2 in Fig.4-40 looks similar to the positive parity band of  $^{195}\text{Tl}$  (see Fig. 4-50). The positive parity band comes when one of the unpaired neutrons occupies an  $i_{13/2}$  orbital while the second one settles in a negative parity orbital, i.e. the configuration is  $\pi 1h_{9/2} \otimes \nu 1i_{13/2} \nu j$  with  $j = (3p_{1/2}, 2f_{5/2})$ . Thus the positive parity of the band is caused by the involvement of the negative parity low j orbital.

In  $^{192}\text{Tl}$  such a band will involve three odd neutrons (two  $i_{13/2}$  neutrons and one low j negative parity neutron) coupled to the odd proton, with configuration  $\pi 1h_{9/2} \otimes \nu 1i_{13/2}^2 \nu j$ . In order to study further such an option one has to determine unambiguously the spins and parities of bands 2 and 3, which is being planned.

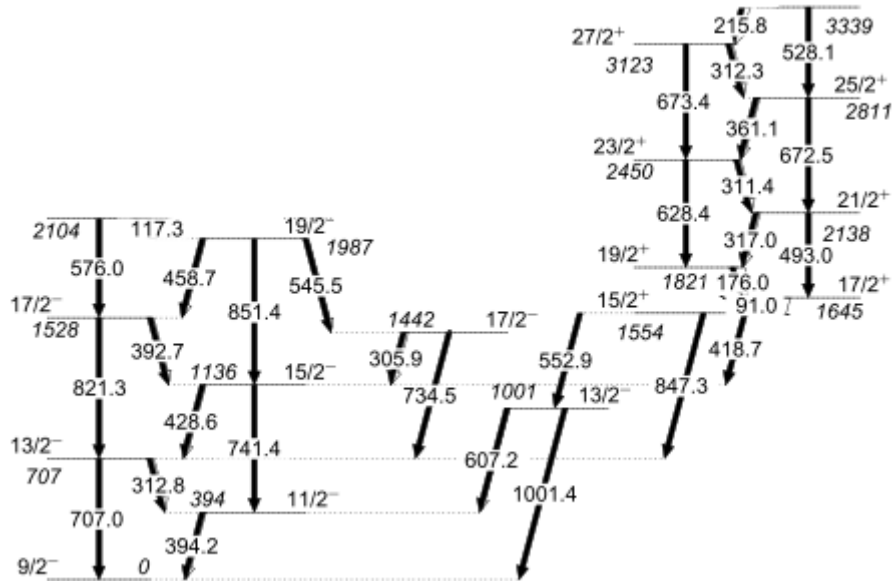


Fig 4-50  $^{195}\text{Tl}$  even parity band



## 5. Conclusion

This work had more than one objective.

One of the main objectives of this work was to learn and understand how to perform gamma spectroscopy research, starting from the beginning of an experiment until the final presentation of the data and interpretation of the results. This covered learning how to choose fusion evaporation reaction in order to produce the nucleus of interest  $^{192}\text{Tl}$ , and the role the beam energy plays. It included hands on experience with setting up the experiment, such as adjusting pole zero and CFD thresholds and also an understanding of the basics of the electronics needed to operate the AFRODITE array. Furthermore the principles of the detection of gamma rays, the basic characteristics of gamma ray detectors, their properties and operation were studied. The data would be impossible to analyse without the preliminary data manipulations, such as gain matching, energy calibrations, Doppler shift corrections, as well as the gain drifts corrections which proved to be a formidable task. Sorting the data and constructing  $E_{\gamma} - E_{\gamma}$  matrices completed this preliminary analysis.

Another objective was to extend the previously known level scheme. More than 50 new transitions were placed in the level scheme forming three new bands. Understanding how

rotational bands are formed (in the framework of the PRM) was the next step. A crucial role is often played by the Coriolis force which breaks pairs and aligns the odd neutrons along the rotational axis. Furthermore the method of comparing with the rotational bands in the neighbouring isotones and isotopes in order to explain the observations proved invaluable.

Another task that was set was to investigate the possibility of a chiral partner to the yrast band. But unfortunately such band was not found in our data. It is my opinion that a chiral band exists for  $^{192}\text{Tl}$  based on trends in the neighbouring nuclei. Further studies with increased statistics in  $^{192}\text{Tl}$  might reveal such bands. We can also have another look at our data after adding to it the data set collected with the thick target.

The study of the  $^{192}\text{Tl}$  thin target is in no way complete yet, since spin and parity measurements, etc. are not performed. A future study will focus on these and other quantities.



## 6 References

- [Bru11] Jorg Brucher Influence of P/Z setting on peak and lower spectrum cut off with MCA16, 18 December 2011, <[http://www.gbs-elektronik.de/fileadmin/download/manuals/mca\\_pole-zero-adjustment.pdf](http://www.gbs-elektronik.de/fileadmin/download/manuals/mca_pole-zero-adjustment.pdf)>
- [Cae11] CAEN digital pulse height analyser-a digital approach to radiation spectroscopy (2011), accessed 18 December 2011, <[http://www.caen.it/documents/News/32/AN2508\\_Digital\\_Pulse\\_Height\\_Analyser.pdf](http://www.caen.it/documents/News/32/AN2508_Digital_Pulse_Height_Analyser.pdf)>
- [Dra96], N. Drakos (1996), Studies of excited nuclear states by using the gamma-gamma coincidence technique, accessed, 18 December 2011, <<http://www.nuclear.kth.se/courses/lab/latex/gammagamma/gammagamma.html>>
- [Ele06] Electronics for physics experiments lecture notes, department of physics, university of the Western Cape
- [Exo11] EXOGAM detectors, accessed 18 December 2011, <<http://pro.ganil-spiral2.eu/laboratory/detectors/exogam/exogam-detectors>> stern Cape, 2006, page 30 and 40 fig 70
- [Fer06] K. Ferlic, The phenomenon of pair production (2006), accessed 18 December 2011, <[http://ryuc.info/creativityphysics/energy/pair\\_production.htm](http://ryuc.info/creativityphysics/energy/pair_production.htm)>
- [Fra97] S. Frauendorf, J. Meng, Nuclear Physics A 617 (1997) 131
- [Gam11] Gamma spectrum Generator, accessed 18 December 2011, <[http://www.nucleonica.net/wiki/index.php/Help:Gamma\\_Spectrum\\_Generator](http://www.nucleonica.net/wiki/index.php/Help:Gamma_Spectrum_Generator)>
- [Haw98] D. Hawcoft, Zakopane school of physics 1998, Search for hyperdeformation in Uranium isotopes <<http://ns.ph.liv.ac.uk/posters/dh/poster.html#introduction>>
- [Kra88] Kenneth S. Krane, Introductory nuclear physics, by John Wiley & Sons, Inc. Page 213-217, 198-204, 416-419.
- [Kol11] D. Kollar, Pulse processing and analyses, accessed 18 December 2011, <[http://www.dnp.fmph.uniba.sk/~kollar/je\\_w/el3.htm#6](http://www.dnp.fmph.uniba.sk/~kollar/je_w/el3.htm#6)> 213-217

- [Kre79] A. J. Kreiner, Physics Review C, 21, (1980), page 937, High-spin band structure on  $^{192}\text{Tl}$
- [Law11] Elena Lawrie, iThemba Labs, Nuclear structure lecture notes (2011), Page 8, 12, 19 and 51
- [Lab11] Attenuation of photons, national physics laboratory (2011), accessed 18 December 2011, <[http://www.kayelaby.npl.co.uk/atomic\\_and\\_nuclear\\_physics/4\\_2/4\\_2\\_2.html](http://www.kayelaby.npl.co.uk/atomic_and_nuclear_physics/4_2/4_2_2.html)>
- [Nil12] Nilsson diagram, accessed 5 January 2012  
<<http://www.wiley.com/legacy/products/subject/physics/toi/toi.pdf>>
- [Nuc12] Compton continuum, nucleonica.net, accessed 5 January 2012  
<[http://www.nucleonica.net/wiki/index.php?title=File%3ADetector\\_Response\\_Components\\_Spectrum.jpg](http://www.nucleonica.net/wiki/index.php?title=File%3ADetector_Response_Components_Spectrum.jpg)>
- [Mid11] MIDAS data acquisition system, accessed 5 January 2012,  
<<https://daq.tlabs.ac.za/>>
- [Obe11] Obed Shirinda and Elena Lawrie, iThemba Labs, Chiral symmetry in real nuclei (2011), lecture slides
- [Pra10] D.A.E Symp.on Nucl. Phys. 55 (2010), P.N. Prashanth, Clover detectors set-up for the study of beta decay spectroscopy,
- [Rad00] Online information on Radware (2000), accessed 18 December 2011  
<<http://radware.phy.ornl.gov/info.html>>
- [Ran06] Ranjan Bohwmik, Inter university accelerator centre, New Delhi, Experiments with large gamma detector arrays lecture slides 4 (2006)
- [Rud10] Rudolph Nchodu, Department of Physics, University of the Western Cape, 2010, lecture notes,
- [Sha10] John F. Sharpey –Schafer, Department of physics, university of the Western Cape lecture notes (2011) page 87
- [She98] Sara Shepherd Segmented germanium detectors (1998), accessed, 18 December 2011 <<http://ns.ph.liv.ac.uk/posters/sls/poster.html>>



<<http://radware.phy.ornl.gov/info.html>>

[Wan10]ShuangQuan B. Qi, S.Y. Wang, Zhang School of Physics, Peking University lecture slides (2010), Static chirality and chiral vibrations of atomic nuclei in particle rotor model,

